Stony Brook University

Searching for dark matter with the *Fermi*-LAT and through new experimental ideas

A Dissertation presented

by

Andrea Massari

to

The Graduate School

in Partial Fulfillment of the

Requirements

for the Degree of

Doctor of Philosophy

in

Physics

Stony Brook University

August 2016

Stony Brook University

The Graduate School

Andrea Massari

We, the dissertation committee for the above candidate for the

Doctor of Philosophy degree, hereby recommend

acceptance of this dissertation.

Rouven Essig - Dissertation Advisor
Assistant Professor - Physics & Astronomy

John Hobbs - Chairperson of Defense
Professor - Physics & Astronomy

Patrick Meade - Committee Member
Associate Professor - Physics & Astronomy

Amarjit Soni - Outside Committee Member
Senior Scientist, Department of Physics - Brookhaven National Laboratory

This dissertation is accepted by the Graduate School.

Nancy Goroff
Interim Dean of the Graduate School

Abstract of the Dissertation

Searching for dark matter with the *Fermi*-LAT and through new experimental ideas

by

Andrea Massari

Doctor of Philosophy

in

Physics

Stony Brook University

2016

The evidence for dark matter is overwhelming. We know where the dark matter is, how much there is, but we do not know what type of particle it consists of. Experimental efforts, as well as theoretical, have tried to shed light on its identity. On the experimental side, "indirect detection" aims to detect stable leptons, baryons, or photons resulting from the annihilation or decay of dark matter particles in outer space. On the other hand, "direct detection" experiments have the goal to reveal interactions of the dark matter particles with electrons or nuclei in a detector on Earth. To date, none of these endeavors has found convincing evidence for dark matter detection. In this dissertation I will describe two ideas to constrain and probe dark matter. One project focuses on indirect detection, where we used all-sky data from the *Fermi*-LAT gamma-ray space telescope. We developed a new method to optimize the choice of the data subsets used to derive constraints on theoretical models, with the aim

of making the bounds as strong, and yet conservative, as possible. The other project is on direct detection. Here we propose a new experimental concept to probe dark matter with masses as low as 1 MeV. The experiment is sensitive to possible interactions between dark matter particles and electrons within a scintillating target material under cryogenic conditions. Such interactions could eventually produce one or more photons. These photons could be revealed using state-of-the-art zero-dark-count single-photon detectors such as MKIDs or TES. The proposed experimental concept could open up vast new regions of the dark matter parameter space.

Dedication

This thesis is dedicated to the life forms who have loved me. Mostly mammals of the orders carnivora and primates. But also yeasts and bacteria of several genera, such as Saccharomyces, Acetobacter, Leuconostoc, and Lactobacillus.

Susy, who always ran away;
then, when I thought I'd caught her,
ran away for good.

Contents

List of Figures

List of Tables

Acknowledgements

Thank you Rouven for supporting, guiding, caring about, and bearing with me. Thank you Patrick, John, and Dr. Soni, for the time spent on reading my thesis, and all the advice and help.

Thanks to my collaborators: Tien-Tien, Andrea A., Elliott Bloom, Eder, Steve Derenzo, Adrian, who's my first friend. Thanks to those who make the PhD program possible (or at least probable): Sara, Nathan, Donald, Betty, Helen, Jac. Thanks to all the splendid scholars who have helped me along the way: Abhay, Tom Hemmick, Martin, Peter van Nieuwenhuizen, Concha, Robert Shrock, Stan Metchev, Sally Dawson, Sasha Abanov, King George Sterman...

Thank you, David Kahn, for your generosity, your support, your encouragement, your very honest advice, and all you've done for me. I'd be in a different place now, hadn't it been for you. Thank you Scott Sutherland, Tom Sexton, Lisa Berger, Edward Pascuzzi for the help, advice, and trust.

Thank you, MoMath people: Cindy, Paul, Alice, Nick, Sook, for your kindness, your believing in me, and accepting me to work with you.

Thank you, office mates at YITP, room 6114, for being the smartest, most fun, most evil, and hottest people to my knowing. Hari (who's like an annoying brother), Michael (the abusive Mathematica user), Tyler (the injured ranter), Colin (the awkward guy without flaws, hmmmm, still looking, though), Yiming (aka Wesley, the bad bad person), Yihong (eternal conjugal Skype call), Pin-Ju (the Dallas dodger), Jun (guilty of giving Yiming a car). Of all the ways to procrastinate, you've been the best. And I would know.

Thanks to my other dear buddies in physics: Ahsan, who's like a brother, Marco B., Veronica P., Paolo G., Pincella-San, Marcos, Ludwig, Morgan, Gustavo, Angelo, the former ram, Federica, Hye-Yun, Ju, Yiwen, Madalena, Ricardo, Sujan, Tin, Humed, Oumarou, Adam J., Marija, Constantinos, Arthur,

Aungshuman, Delton, Aleksas, Omer, Rahul, who's like a Canadian brother, Peter S., Missy, Francis, Ben, Albi, Chiara P., Valentina A., Sam R., Yongky.

Thanks gentle soccer and gentle reading people: Naveen, Abhi, Chandrika, Zeyu, Cam, Jimmy, Mu, Frederick, Yen. Thanks housemates: Andrey, Džejla, Mathew, Luca, Giulia. Thanks to my great landlord, Dan Hayes. Thanks queer folks: Alissa, Wei, Andrew, Jxhn, Janelle. Thanks SBU fencing club; you have kept me sane for a long while. Nick, Avery, Sly, Katherine, Alec, Braulio, Brianna, Kai, Jackson, Jay, Dave, Eleanor, Elias, Olivia, Randi, Tom, Esau, Kelley, Kerry, Michael, Sidney...

Thanks Stony Brook people I love: Fadi the piano, Sophie the violin, Natalie also violin, Maryam the hair, Dave Frank the Costco, Samira the everything, Terry-Ann the Mount Grey, Jocelyn the Ho, Adam Parr the philosophy, Helen J. the age appropriateness, Sheng the Chapin, Li Sha the Flushing, Matt Wroten the gathering, Alireza the flying carpet, Jon the talisman, Yury the... Yury, John S., Dan B., Alan & Ali the boardgames.

Thanks to my students: Brittney H., Liam, Karen, Tom, Lyndsey, Syed, Zainab, Katie N., and Kathy, who was the first. Thanks Brittany, you soft snake, Shu, Shuhao, Udele, Tae, Levi, Adrienne, Lilly, Rey, Charlton, Lijie, Kunal, Mark, Bonnie, Gia, Kevin for Brahms, Danny, Avery, who's awesome.

Thank you mom and dad for being always around but never in the way. I wish you thought of yourselves a tenth of what you're worth. Thanks grandma for still asking for a kiss from me, despite decades of denials. Thanks Elena for being my longest serving sister and somewhat tolerating me in my worst years. Thanks Laura for having come along and made life more fun. Thanks Nala for having been my feline daughter for a year, and for the polite love you've given me. Thanks Lola and Nerina, black creatures.

Thanks Angi and Silvana, for the restless support and generosity. Thanks Ale, Andreino, Giulia, Sabrina, for being silly cousins. Thanks Emilio, for the care you've taken of me. Thanks Amri.

Thanks to those who have died before I got here: Giuliano, Alberto, Giulio, Lina, Luna, Alf, Fonzie. And Susy, who disappeared. I'm sorry I couldn't share this with you all.

Thanks to my very best friends for ever: Za, who's my high-school buddy for some weird reason; Andy? Drew? Whatever he's called, for being a little brother, big and sweet, but mostly big; Lollo, for being a kind nice funny gigantic boy; Eleonora, for being the first person to tell me they loved me (as a friend); Giulia, for sharing this happy exile with me; Fly, whom I haven't met yet, but, if...; Ken, for being a corporate cutie pie, my role model, benefactor, and one of the nicest and most polished people I know; Le, whose butt I am very prone to hurting, but who has always come back to me nevertheless; Raquel, my daughter, for being an unamendable goofball and liking dates, avocados, and me; Nissim, for being an exhilarating source of counterexamples to ordinary human behaviors, and putting up with mine; Michael Richardson, for the paganism, the crystalline openness, the unhealthy amount of laughs we've given each other, and for eventually not marrying my ex; Celeste, the lone gold star, for being one of the truly nicest, most generous, and funniest people I know; Karen, who is blunt, lukewarm, has a million ethical rules I don't care for, plays boardgames almost as addictively as I do, and is generally wonderful; Alison, for being Alison, which in the dictionary reads: "assertive, direct, smart, gentle, empathetic, insightful, adventurous, candid, beautiful, funny".

Thanks Nina the teacher, Tanzeem the Tanu, Helena of Slytherin, Giamma the Carta, Klappa the nomad, Genna Mongolari, Gigia the fishermen's friend, Matte il Figher.

Thanks to those who have just essentially stopped talking to me for very diverse reasons: Christine, Marina, Chiara, Alessia, Dayoon, Valentina, Megan, Clara, Thao, Sarah, Pupy, Maureen, il Bella, Solomon, Elena. I miss some of you.

If I forgot someone, I might have done it on purpose, I guess? It doesn't matter. Love, and do what you will.

Chapter 1

Introduction

Particle Physics offers a highly predictive description of the Universe. This is encoded in the Standard Model of Particle Physics, complemented by massive neutrinos [1], and General Relativity, as a theory of gravitation [2]; within the frameworks of Quantum Mechanics and Statistical Physics.

General Relativity is a classical field theory of the metric tensor of a pseudo-Riemannian manifold. The metric completely determines the gravitational forces on an object and its trajectory. The Standard Model is a "quantum field theory of particles". This means that the degrees of freedom of the theory are complex-valued fields defined on the flat Minkowski space-time and they represent particles with some probability of interacting at a certain point of the space-time. In particular, spin-1 bosonic fields represent the interaction carriers. They are divided into three sets: the eight massless carriers of the strong interaction (QCD), the three massive carriers of the weak interaction, and the photon, the massless carrier of electromagnetism. The weak and electromagnetic interactions are further unified into the *electro-weak theory*. Fermionic spin-1/2 fields represent the matter in the Universe. They are divided into leptons and quarks. The leptons are typically lighter, have integer electric charge $(0, \pm 1)$ and are subject to the electro-weak force only. The quarks are typically heavier, have fractional electric charges $(\pm 1/2, \pm 2/3)$ and also interact via the strong force. There is also a field, the *Higgs field*, which couples to all massive particles. As this field acquires a non-zero vacuum ex-

pectation value, some of its interaction terms provide these particle with their masses. This is known as the Higgs electro-weak symmetry-breaking mechanism. Of the initial Higgs field, a massive bosonic spin-0 electrically neutral one is left behind, which is called the *Higgs boson*.

As empirically successful as this formulation may be, boasting the recent triumphs of the discovery of the Higgs particle [3] and the first direct detection of gravitational waves [4], open problems have existed for decades, which call for a supplementation of the current theories. I will list here some of these problems, and sources to learn more about them.

- Strong CP problem. Why does the strong interaction conserve the combination of Charge conjugation (C) and Parity transformation (P), although the symmetries of the theory allow for CP-violating terms? [5]

- Neutrino masses. What are the individual masses of the neutrino mass eigenstates? What is the mass term for the neutrinos? Are neutrinos Majorana or Dirac particles? [6]

- Flavor problem. Why are flavor-changing neutral currents not observed around the weak scale, when they are expected in most non-fine tuned theories that explain electro-weak symmetry breaking? Why are there three generations of fermions? How are their masses related? [7, 8]

- Unification of interactions. Why do the couplings of the three Standard Model interactions seem to converge to the same value when calculated at very high energies ($\sim 10^{16}\,\mathrm{GeV}$)? [9]

- Higgs hierarchy problem. Why is the mass of the Higgs so small compared to the natural value that it might have, given the quadratic dependence on the cut-off energy (*i.e.* Planck mass)? [10]

- Quantum formulation of gravity. Can we write a theory of gravity that is compatible with quantum mechanics and has practical predictive power? [11]

- Baryogenesis & Leptogenesis. How come there are almost only baryons (leptons) and very few anti-baryons (anti-leptons) in the visible Universe? [12, 13]

- Cosmological constant problem (cosmological hierarchy problem). Why is the energy density of the Universe (dominated by the Dark Energy) so low compared to the expected value? [14]

- Particle nature of the dark matter. What types of particle constitute the dark matter? What forces are they subject to? [15]

- Field-theoretical nature of Dark Energy. What is the equation of state of the Dark Energy? What quantum theory originates it? [16]

As we see, a good number of problems concerns our understanding of the evolution and make-up of the Universe at large scales. In this thesis I will be focusing on the problem of identifying the particle nature of dark matter.

The problem is of particular significance, as current estimates have the dark matter constituting $\sim 85\%$ of the visible Universe's matter. This vast amount of matter could have the most disparate properties and range from a very simple elementary-particle constituent interacting only with gravity to a very complex mix of bound states interacting with the Standard Model particles and new unknown forces. Given the amount of uncertainty, we are bound to be met with astonishing surprises.

I will start by explaining the dark matter hypothesis, why we are confident in it, and what we know about it. Then I will present some particle candidates to the role of dark matter, and talk about what the experimental and theoretical attempts have been at shedding light on this conundrum. After that I will go on to present my contributions to the field. One is a project on optimization of model constraint derivation from indirect detection data; the other is a novel proposal for an experimental technique of direct detection using scintillation.

1.1 The evidence for Dark Matter

Dark matter is a postulated substance subject to gravity but possibly not to the other known interactions (unless to a very little extent), which is thought to constitute the majority of the matter in our Universe [17].

The dark matter hypothesis was first put forth by astronomer Fritz Zwicky in the 1930s in order to explain the typical velocities of galaxies within clusters [18]. Evidence for the existence of (non baryonic) dark matter is extremely convincing, albeit to date exclusively due to astronomical observations of its gravitational effects (and although alternative hypotheses still exist [19]). Let us review the main arguments supporting the dark matter hypothesis.

Historically, the first evidence for dark matter came from dynamical considerations about spiral galaxies and galaxy clusters. In the case of a spiral galaxy, with its approximate cylindrical symmetry, it is possible to consider the circular speed of objects orbiting around it as a function of their distance from the galaxy's center. As illustrated in Fig. 1.1, the approximate expected behavior of such a function should be a power-law decline, once the distance from the center is large enough to enclose most of the visible matter in the galaxy (disk contribution). However, the data shows that the rotational speed reaches a maximum and then plateaus well outside the visible galactic outskirts. Postulating the existence of additional matter inside and around the galaxy (the "dark matter Halo") is an attractive solution to this conundrum [20].

A similar problem occurs when considering the velocities of the member galaxies within a galaxy cluster. The virial theorem, applied to Newtonian gravity, states that the average kinetic and potential energies satisfy:

$$2\langle T\rangle = -\langle V\rangle, \tag{1.1.1}$$

and therefore, with enough measurements of the individual velocities of the member galaxies, it is possible to deduce what the average gravitational potential of the cluster is, and with that obtain an estimate of the total mass in the system. Zwicky first used this method and realized that a gross mismatch

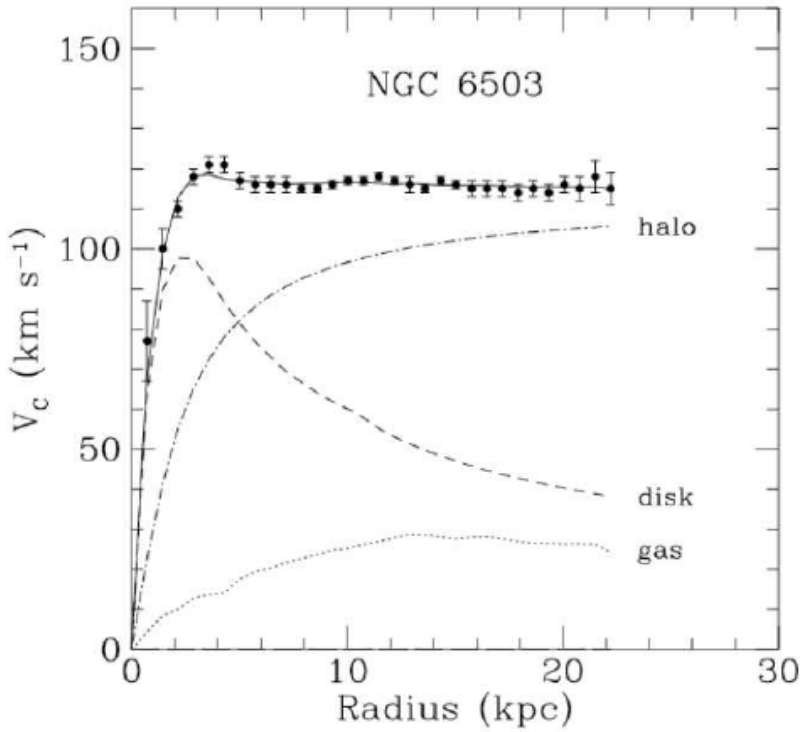

Figure 1.1: Rotation curve for the galaxy NGC6503 from [21].

existed between this estimate and the one obtained from spectroscopic analysis of the visible matter in the cluster [18].

Another important case, where the presence of dark matter is suggested, is the explanation of the *Cosmic Microwave Background* (CMB) "Power Spectrum". The CMB is constituted by those photons that were in equilibrium with baryonic matter at an epoch when the temperature of the Universe was enough to keep electrons and protons from forming bound atoms. These photons were kept in equilibrium by frequent scattering off the matter, but when the temperature decreased below a certain critical value, electrons and protons bound together and the photons stopped scattering off the now neutral matter. This event is known as *recombination* and/or *last scattering*. The CMB photons come from such long distances that they are enormously redshifted and are detected as a black body of microwaves with an average temperature of $\sim 2.726\,\mathrm{K}$. However, very small temperature differences (temperature

anisotropies) exist between different locations in the sky, and the pattern of these has extremely important implications for the evolution and causal structure of the Universe. For a complete introduction see [22]. The power spectrum of these oscillations is derived from their spherical harmonic expansion:

$$\frac{\delta T}{T}(\theta,\phi) = \sum_{\ell=2}^{\infty}\sum_{m=-\ell}^{\ell} a_{\ell m} Y_{\ell m}.(\theta,\phi) \tag{1.1.2}$$

Squaring this, taking a spatial average, and summing over the azimuthal variable m (which improves the statistic), yields

$$C_\ell \equiv \frac{1}{2\ell+1}\sum_{m=-\ell}^{\ell} |a_{\ell m}|^2. \tag{1.1.3}$$

Now that we have the definition of the power spectrum, how does physics inform us about it? Heuristically, what these coefficients mean is how big, on average, the temperature oscillations are, seen at a certain angular scale (defined by ℓ). Several experiments have provided us with an accurate look at the CMB power spectrum, the latest of which being the Planck satellite [23]. In Fig. 1.2 we can see the experimental results. While the first peak is related to the recombination event, the peaks at higher ℓ are an imprint of the acoustic oscillations in the expanding pre-recombination photon-baryon plasma. As one can see in Fig. 1.3, different values of the abundance of total (non relativistic) matter and baryonic matter (Ω_m and Ω_b) would significantly deform the shape of the CMB power spectrum, especially in the relative height of the second and third peak.

The data is fitted by a model that includes $\Omega_m h^2 \sim 0.31$ and $\Omega_b h^2 \sim 0.022$ [24]. Since $\Omega_{DM} = \Omega_m - \Omega_b > 0$, this is very strong evidence for dark matter.

We should also add that an independent confirmation of the size of the abundance of the baryonic matter Ω_b is provided by the theory of *Big Bang Nucleosynthesis* (BBN) [25]. This is a theoretical model based on standard cosmology and nuclear physics which predicts, without introducing any free

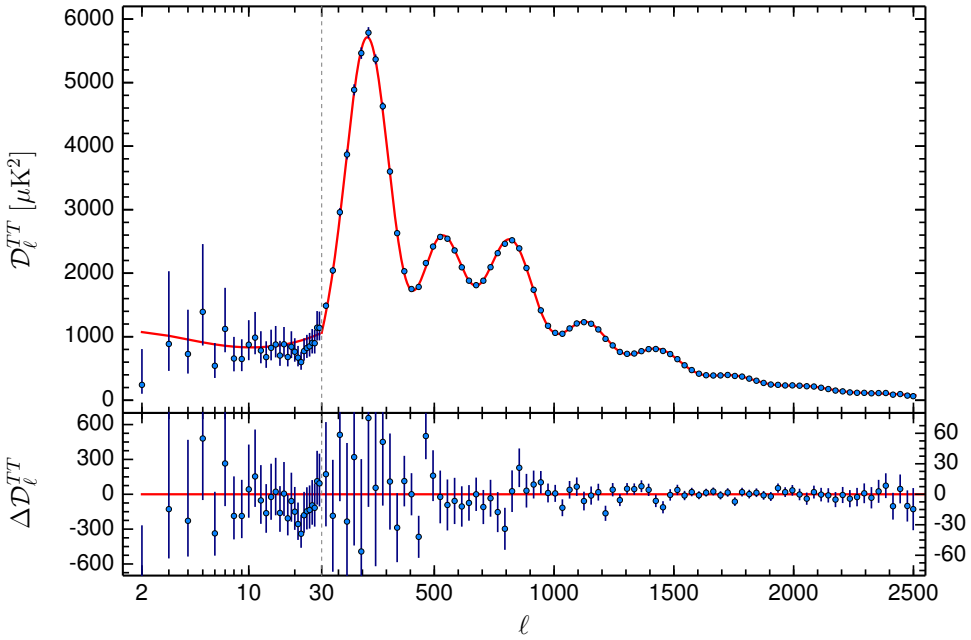

Figure 1.2: Power spectrum and best fit to the ΛCDM model from [24].

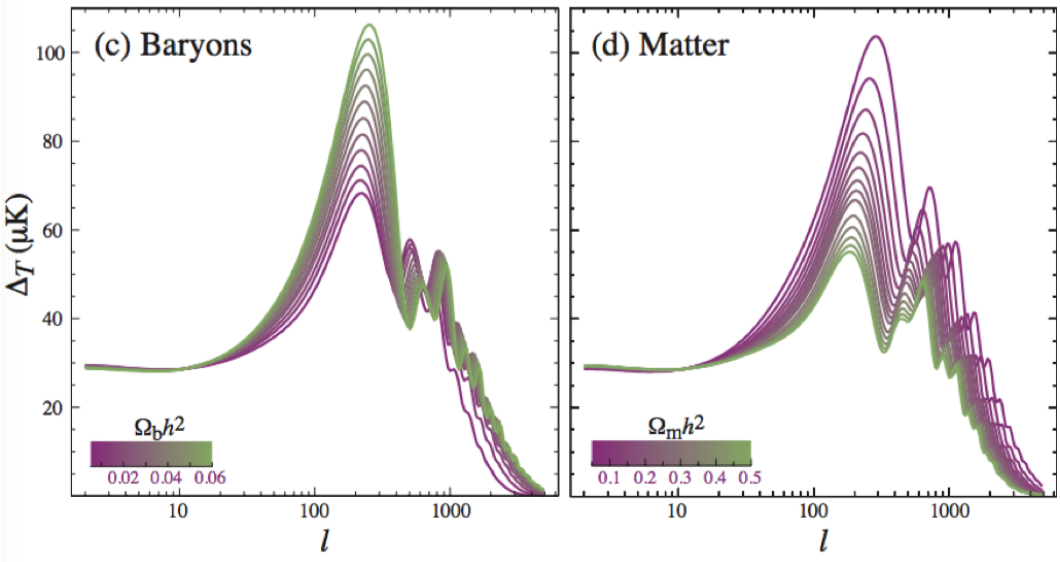

Figure 1.3: Effect of varying total matter and baryonic matter abundances on the CMB power-spectrum shape. From [22].

parameter, the abundances of the lightest stable nuclei in the Universe (^{1}H,^{2}D, ^{3}He,^{4}He,^{6}Li,^{7}Li,^{7}Be). Using the value of $\Omega_b h^2$ quoted above, the model predicts abundances that match with the observations within the uncertainty (except for ^{7}Li), corroborating the results of CMB analysis, and therefore serving as further evidence for dark matter.

Another piece of evidence for DM comes from the shape and make-up of large-scale structures. The visible matter in the Universe is organized in structures hierarchically nested in one another. Super galaxy clusters contain Galaxy Clusters, which contain Galaxies which in turn contain dwarf Galaxies; all of these objects having characteristic size scales.

This particular pattern can be a powerful tool to infer the properties of the matter in the Universe thanks to tools capable of numerically simulating the evolution of matter density throughout the Universe starting from its early times just after inflation and then focusing on smaller regions to follow the formation of a specific structure (see *e.g.* [26]). The results of such simulations yield structures similar to the ones we observe only when non collisional and non relativistic matter ("cold dark matter" or "warm dark matter") is used (*e.g.* [27]), thus suggesting that most of the matter in the universe is dark.

Another important and unexpected confirmation of the dark matter hypothesis comes from the observation of galaxy cluster collisions, the first and most famous discovered being that of the "Bullet Cluster" [28]. The observation shows two distinct clusters of galaxies whose configuration suggests that they collided with each other around 3.7 billion years ago. From X-ray spectroscopy it was observed that the hot intergalactic gas constituting most of the visible matter in the clusters was heavily affected by the collision, somewhat dragging behind the stars (which instead proceeded undisturbed, as expected), and acquiring the typical shape of a shock-wave (which earned the smaller cluster its name). Scientists then applied the technique of *weak gravitational lensing* [29] to try and map out the mass distribution of the cluster system [30] . As seen in Fig.1.4, most of the mass of each cluster is distributed in a rather spherical manner and centered around points that are quite far beyond the centers of the gas distribution. This fact is well explained by as-

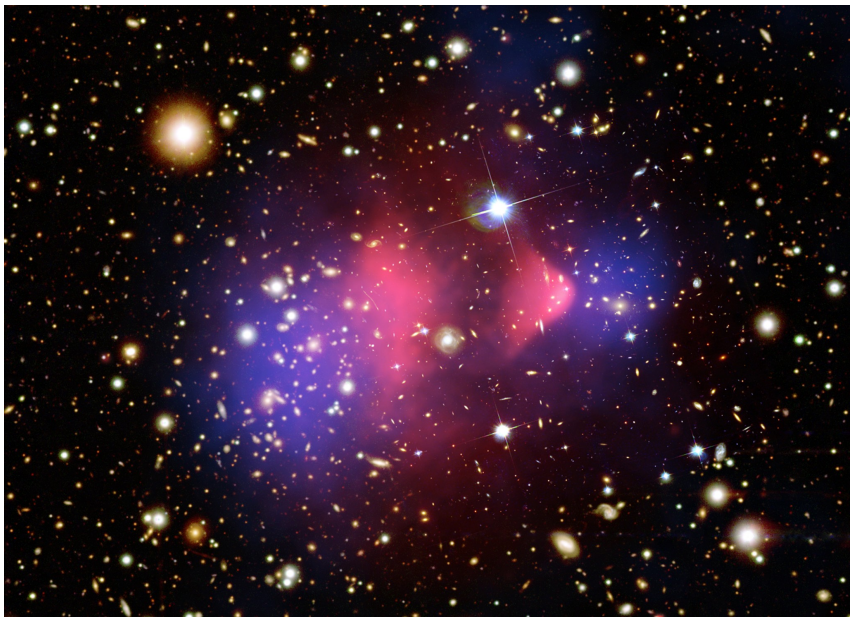

Figure 1.4: The Bullet Cluster. Red: baryonic gas density (from spectroscopy). Blue: total mass density (from weak gravitational lensing). Data from [32] and [30], reformatted by NASA at http://www.nasa.gov/vision/universe/starsgalaxies/dark_matter_proven.html.

suming that most of the mater in a galaxy cluster is made of non-baryonic dark matter. Moreover, this dark matter must be non collisional to a sufficient extent (for bounds on the self-interaction cross section see *e.g.* [31]), in order to be compatible with the observation that it maintained its shape and motion throughout the collision as opposed to the baryonic gas, which was left behind.

1.2 Dark Matter Candidates

Over the last few decades countless models for the dark matter particle(s) have been proposed. (See [33] for a review.) The most appealing are generally motivated within other areas of particle physics and must evade all the experimental constraints. They can be fit into different classes. In this section we briefly review a few of them.

name	baryonic?	Fermion/Boson	mass (eV/c^2)	hot/cold
MACHO	yes	F	$10^{58} - 10^{68}$	cold
axion	no	B	$10^{-6} - 10^{0}$	cold
active neutrino	no	F	$0 - 10^{-1}$	hot
WIMP	no	F	$10^{3} - 10^{12}$	cold

Table 1.1: Dark Matter Particle candidates and properties

Massive Astrophysical Compact Halo Objects (*MACHOs*) are aggregations of ordinary matter that are too compact and too small to emit any light. These include black hole remnants, jupiter-like planets, and brown dwarfs. This hypothesis has been long known to be subject to testing through *gravitational microlensing* [34], the phenomenon by which a compact mass transiting in front of a distant light source will cause a distortion of the source's appearance and a momentary brightening, which is detectable. Such an astronomical search has indeed been performed in the last decade of the 20th century and the results, though extremely rich for the astrophysics of these objects, have definitely proved that they do not make up any significant amount of the dark matter in our Universe [35].

Axions are light spin-0 elementary particles postulated within the theoretical framework introduced by Peccei and Quinn [36] in order to solve the *strong CP problem*. The latter is an open problem within the strong sector of the Standard Model (see [5] for a review) about the experimental absence from the QCD Lagrangian of the CP-violating term

$$\propto \theta \epsilon^{\mu\nu\rho\sigma} G^a_{\mu\nu} G^a_{\rho\sigma}. \tag{1.2.4}$$

The strongest upper constraint on θ comes from the measurement of the neutron's electric dipole (such as [37]). Peccei-Quinn theory [36] justifies the small size of this term by promoting θ to a spin-0 parity-odd particle, the axion, which would be the Nambu-Goldstone boson of a new $U(1)$ symmetry (Peccei-Quinn symmetry). The symmetry would guarantee the vanishing of terms like 1.2.4. At the same time, instantonic effects in the QCD vacuum

would give the axion a mass. This fact, coupled with cosmological evolution considerations, would enable the axion to make up all of the dark matter in the Universe. There are several models of axions and axion-like particles (the latter being unrelated to QCD and the strong CP problem but sharing some fundamental similarities with the QCD axions). Their detection is typically based on the fact that these particles are predicted to couple to the electromagnetic field and therefore conversion is possible between photons and axions [38]. One such experiment is the *Axion Dark Matter Experiment* (*ADMX*) [39].

Active neutrinos could also make up the dark matter. However, given their very small mass, they would have been relativistic when they decoupled from the baryonic matter (see below for a more detailed discussion of decoupling in the case of WIMPs). This is because the expansion rate of the Universe and their interaction cross section with baryonic matter are such that they stop converting into ordinary matter before they cool down enough to become non relativistic. This scenario is what goes under the name of *hot dark matter*, and it presents virtually unsurmountable challenges for structure-formation predictions (see Sec. 1.1) to match with observations, as the amount of coalescence is insufficient [40].

1.2.1 The WIMP miracle

A popular approach, first proposed in the 1970s [41], goes under the name of *WIMPs*. We will go through some steps of the derivation of the so-called *WIMP Miracle*, see *e.g.* [42]. The model makes the assumption that the dark matter (χ) used to be in equilibrium with the Standard Model particles (X) in the early Universe. This equilibrium is regulated by the Boltzmann equation:

$$\frac{1}{V}\frac{\mathrm{d}N_\chi}{\mathrm{d}t} = \langle\sigma_{X\bar{X}\to\chi\bar{\chi}}v\rangle n_X^2 - \langle\sigma_{\chi\bar{\chi}\to X\bar{X}}v\rangle n_\chi^2, \tag{1.2.5}$$

where $V = a^3$ is a co-moving volume and a the scale factor of the Universe, N_χ is the number of χ-particles in the volume V, $n_{\chi/X}$ is the particle number density, v is a relativistically invariant relative velocity between two particles

(or, better, the Møller velocity [43]), $\sigma_{XX\to\chi\chi}$ the annihilation cross section of Standard Model particles into dark matter ones, and $\langle\ \rangle$ denotes a statistical Boltzmann average over v. The equation becomes, on the left-hand side,

$$\frac{1}{V}\frac{\mathrm{d}(n_\chi V)}{\mathrm{d}t} = \frac{1}{V}\frac{\mathrm{d}(n_\chi a^3)}{\mathrm{d}t} = \frac{1}{V}\left(V\frac{\mathrm{d}n_\chi}{\mathrm{d}t} + 3a^2\dot{a}n_\chi\right) = \frac{\mathrm{d}n_\chi}{\mathrm{d}t} + 3Hn_\chi \quad (1.2.6)$$

where H is the Hubble parameter. Assuming that the SM particles are at equilibrium for all times with the photon bath of temperature T, and that, before the decoupling, DM was also in equilibrium with them, implies

$$\langle\sigma_{X\bar{X}\to\chi\bar{\chi}}v\rangle = \langle\sigma_{\chi\bar{\chi}\to X\bar{X}}v\rangle, \quad (1.2.7)$$

$$n_X = n_\chi^{\mathrm{EQ}}, \quad (1.2.8)$$

where n_χ^{EQ} solves the Boltzmann equation at equilibrium. Thus the Boltzmann equation for χ becomes

$$\frac{\mathrm{d}n_\chi}{\mathrm{d}t} = -3Hn_\chi - \langle\sigma_{\chi\bar{\chi}\to X\bar{X}}v\rangle\left(n_\chi^2 - \left(n_\chi^{\mathrm{EQ}}\right)^2\right). \quad (1.2.9)$$

If for convenience we define,

$$Y \equiv \frac{n_\chi}{s}, \quad (1.2.10)$$

$$x \equiv \frac{m}{T}, \quad (1.2.11)$$

where s is the entropy density of the Universe, and m is the mass of χ, we obtain

$$\frac{\mathrm{d}Y}{\mathrm{d}x} = -\frac{sx\langle\sigma v\rangle}{H}\left(Y^2 - Y_{\mathrm{EQ}}^2\right). \quad (1.2.12)$$

After the Universe cooled down to temperatures comparable with the DM particle mass ($x \sim 3$), the process of annihilation of SM particles into DM particles was exponentially suppressed and the DM was doomed to deplete into ordinary matter. However, the Universe is also expanding and therefore

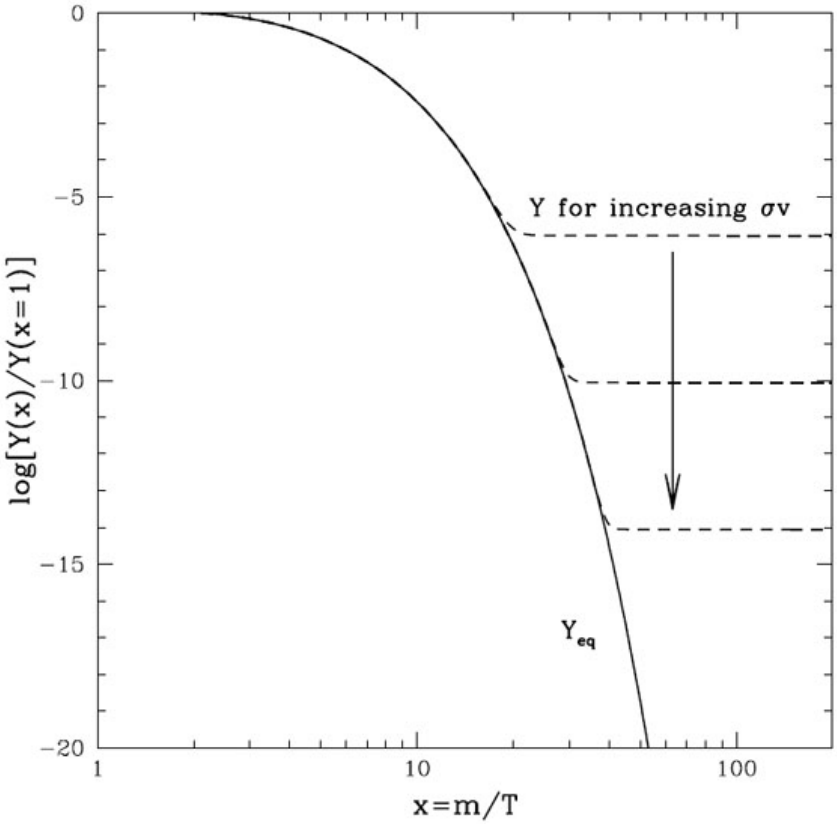

Figure 1.5: Numerical solutions of Eq. 1.2.12 for different values of $\langle \sigma v \rangle$. From [42].

some point comes when the average relative expansion rate between two DM particles is so high that their annihilation rate into SM particles goes to zero. The DM particle number becomes therefore asymptotically constant. This mechanism is called *thermal freeze-out*.

In Fig. 1.5 we see how the average cross section is key to determining the final asymptotical abundance of the dark matter. Therefore, since we know the expansion rate and what the DM energy density is at our epoch, we can work out what the annihilation cross section and mass for these hypothetical particles should be, and we find surprisingly that

$$\langle \sigma v \rangle \sim 10^{-26}\,\mathrm{cm}^3\mathrm{sec}^{-1} \tag{1.2.13}$$

$$m_\chi \sim 100\,\mathrm{GeV} \tag{1.2.14}$$

which is around the energy scale of electro-weak dynamics. This lends this and similar models the name of *Weakly Interacting Massive Particles* (*WIMPs*). This fact is sometimes referred to as the *WIMP miracle*. The miracle here is that an unknown particle interacting via the weak force would naturally have the correct relic abundance to make up the dark matter. Moreover, given its typical mass, this particle would decouple from the baryonic matter before the epoch of BBN (see Sec. 1.1), therefore preserving the successful predictions of cosmic nuclear abundances. This scenario was particularly appealing when several supersymmetric models (invoked to solve the Higgs hierarchy problem, see Sec. 1 above) required the existence of undiscovered stable fermionic partners to the weak force carriers [44]. The enthusiasm around this coincidence has somewhat faded over the last decade, especially as LHC established new and much higher lower limits for the masses of the still undiscovered supersymmetric particles [45]. Also, direct detection experiments (see below) have begun to probe deeply into the parameter space of dark matter particles interacting through the weak force carriers or the Higgs, yet without positive detection results. However, the general WIMP paradigm remains a standard framework for dark matter models and searches, as we will see in the following.

1.3 WIMP-like particle detection strategies

Since, as of yet, the only empirical evidence for dark matter is through the gravitational interaction, it is very important to investigate what its particle identity and behavior are.

Assuming that dark matter is a particle with properties similar to those of a WIMP (whence the term "Wimp-like"), the interaction that must exist between DM and ordinary matter for the "miracle" to happen suggests three possible avenues to its detection, as seen in Fig. 1.6.

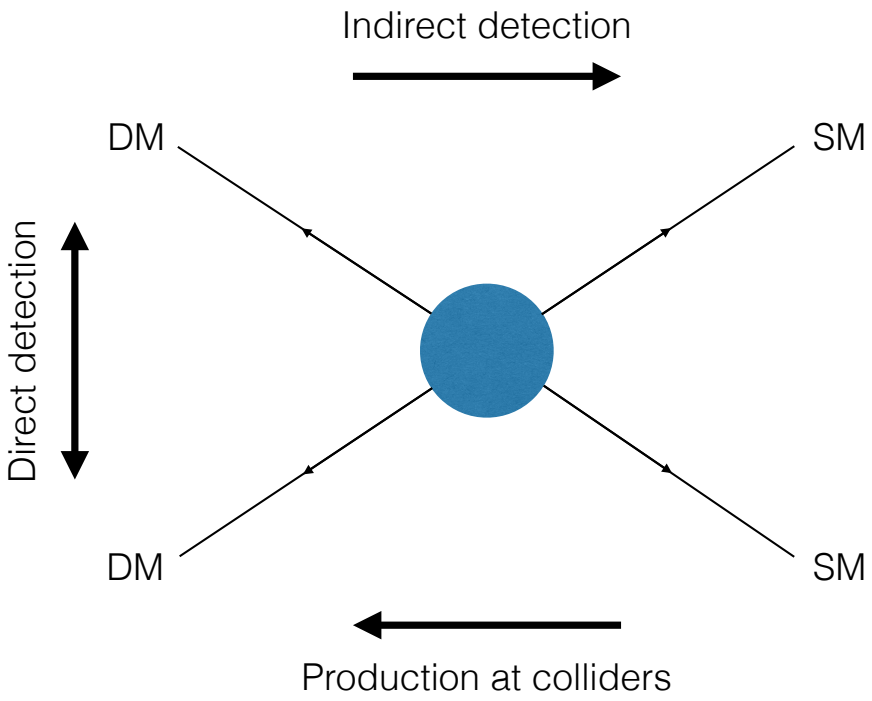

Figure 1.6: Different approaches for WIMP-like dark matter particle detection.

1.3.1 Dark Matter Indirect Detection

According to the WIMP paradigm, WIMPs must interact with Standard Model particles. This would mean that even today the dark matter particles are annihilating or decaying (we have not discussed decaying dark matter models here, we defer this to Sec. 2.4.2) into ordinary particles, though at very small rates. These SM particles could eventually reach observers on our planet Earth in a sizable amount for their detection. This is what we call *indirect detection* [46].

In general, the set-up of an indirect detection experiment is constituted by a detector in space or on Earth, capable of detecting stable particles: photons, charged leptons, neutrinos, stable baryons, which might be the ultimate result of the annihilation (or decay) of dark matter particles in some large region far

away in space.

Naturally, the challenge with this type of experiment is in the modeling of an unavoidable background due to astrophysical processes. This encourages experimenters to look for particularly unmistakable signals, such as "monochromatic lines" (*i.e.* signals made of particles with the same energy, [47]), or signals which are concentrated around areas where the expected dark matter density is particularly high (such as *dwarf galaxies* [48]). We will now briefly review a few recent important experiments in indirect detection.

The Fermi-LAT [49] is a γ-ray space telescope. We will describe its functioning in some detail in the next chapter, which concerns optimization of data analysis from this telescope.

The *Alpha Magnetic Spectrometer* (*AMS*) [50] is a module mounted on the International Space Station. It features a strong magnetic field able to deflect charged cosmic rays in order to identify them. Over the years it has produced important results especially with regard to the cosmic-ray positron-fraction measurement, which exhibits an unexpected rise at high energies [51].

The *IceCube Neutrino Observatory* [52] is an Earth-bound experiment located at the South Pole. Its target is a large block of natural ice deep underground and it is sensitive to very high-energy neutrinos interactions creating inside the ice charged leptons, which in turn are detected through Cherenkov radiation. The collaboration has already produced very significant observations [53] and has been able to put constraints on DM annihilation and decay models [54].

1.3.2 Dark Matter Direct Detection

If dark matter is made of WIMP-like particles, it will be able to scatter off ordinary matter with a certain cross section at a given momentum transfer. Since the Sun is orbiting about the Galactic center, and the Galaxy is thought to possess an overall static dark matter halo, our planet would be sweeping across it and receiving an effective "dark matter wind". Incidentally, due to the relative motion of the Earth around the Sun, this wind will be strongest

in the late Spring and weakest in the late Autumn.

The class of experimental techniques focusing on this scenario goes by the name of *direct detection* [55]. This typically consists of devising a target material in a condition of very low and/or known background and waiting for DM particle to scatter off the material's constituents, depositing a noticeable amount of energy, and thereby creating a visible signal exceeding the background.

Within this family we can further distinguish experiments by the target used (*e.g.*, various non conducting crystals, noble liquids), the parameters probed (*e.g.*, spin-independent or -dependent cross section with nucleons, quarks or electrons), and the type of signal sought (*e.g.*, scintillation, ionization, thermal energy deposition). In addition to this, some experiments focus on recognizing an *annual modulation* pattern in their data spanning several years, which is expected to exist due to the different intensities of the dark matter wind at different times of the year, as explained above.

From the very first conceiving of an experiment by Goodman and Witten [56], impressive progress has been done. In particular, modern experiments are able to perform an active event-by-event signal vs. background discrimination, and have reached considerable sizes, which has led to an exponential improvement of their sensitivities. And alas, no convincing signal has so far been observed in any investigation. Let us review a few current important experiments.

The CDMS collaboration [57] currently works with 600 g Germanium crystal at 10 mK. It is capable of detecting phonon signal (heat) from DM interaction as well as ionization with the purpose of background rejection.

CoGeNT [58] is a liquid-nitrogen cooled 440 g highly pure Ge crystal, detecting ionization.

CreSST [59] uses a 10 Kg $CaWO_4$ crystal, operated at 10mK, and measures both signals from scintillation and heating for event discrimination.

The DAMA collaboration [60] has been using for several years a total 250 Kg in NaI(Tl) scintillators and has focused on detecting an annual modulation signal, which it claims has been found with very high significance [61].

However, this signal seems to be at odds with null results from several other experiments and is not yet accepted by the community as coming from dark matter.

Edelweiss III [62] is a recent experimental effort availing itself of 40 800 g Ge detectors kept at 20mK and is sensitive to ionization and heat deposition signature.

LUX [63] employs 370 Kg liquid Xenon, which scintillates when an excited dimer, a molecule formed by one neutral and one ionized Xe atoms, decays to its ground state.

SIMPLE [64] is rather unique in this list in that it uses a suspension of superheated droplets of C_2ClF_5, which act as bubble chambers for incoming dark matter particles.

XENON100 [65] is also a liquid Xenon detector, very similar to LUX, with a current mass of 100 Kg.

Different theoretical assumptions will assign a different meaning to the (null) results from these experiments. In particular, it is customary to present limits for an interaction made of an effective spin-independent contact operator parametrized by a DM-nucleon cross section $\sigma_{\chi N}$. However, if we assume this term to vanish, we would, at first order, model the interaction with a spin-dependent cross section, which, in particular, will make some nuclei more or less reactive, depending on their spin.

As is seen in Fig. 1.7, current and future experiments are able to probe deeply into the DM parameter space for WIMP masses roughly above a few GeV. For lower values, however, the experimental sensitivity is severely impaired by the requirement that the dark matter scatter off much heavier nucleons, thus transferring much less energy, and therefore failing to trigger a count in the detector. This means that, in order to explore those models predicting a Light Dark Matter (LDM) particle [67], novel approaches are needed.

The second part of this thesis consists of a proposal for a new technique to detect light dark matter using electrons as targets, as first suggested in [68], and low-photon-number scintillation as signal.

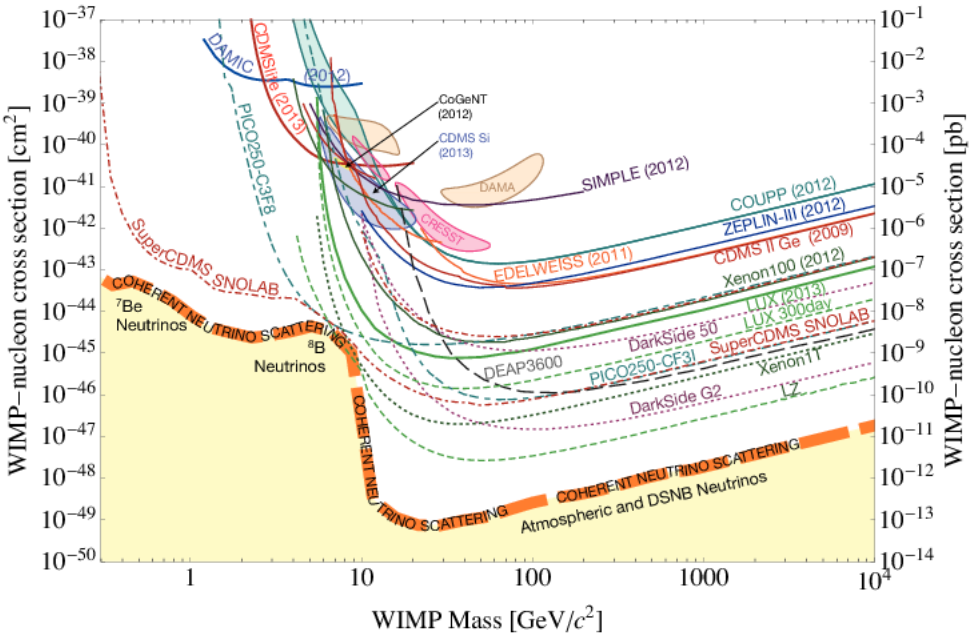

Figure 1.7: Recent dark matter direct detection limits from [66].

1.3.3 Dark Matter production at colliders

SM particles can annihilate together and convert their energy-momentum into the creation of dark matter particles, which could be noticed at colliders typically as missing energy not accounted for by neutrinos and other SM sources. In this thesis we will not focus on this mechanism and refer the reader to [69] for a review.

1.4 The scope of this thesis

Within the experimental efforts described above, my contribution consisted of two projects, whose presentation will take up the following two chapters of this thesis.

1.4.1 Strong conservative limits on dark matter indirect detection from the Fermi γ-ray telescope

The first project is on indirect detection. It uses γ-ray data from the *Fermi*-LAT space telescope. The telescope gathers data from every direction in the sky and records several features about each γ-ray event, such as the direction of the photon in the sky, its energy, the incident angle, the angle the spacecraft makes with respect to the Earth's zenith, and more. We particularly focus on the two angular coordinates determining the spatial origin of the photon, as well as the energy.

Several investigations are possible, that focus on specific regions of the energy spectrum of the sky. One standard analysis derives constraints on DM annihilating (or decaying) into different SM final states. The first step is to compute the expected number of observed photons in a certain energy range and from a certain region in the sky. This number depends, among other things, on the dark matter distribution, the dark matter particle mass, the photon spectrum of the SM final state the model features, and, proportionally, on the annihilation cross section (σ_A) for the primary DM-DM annihilation. This last parameter is normally the free model parameter for which constraints are derived.

Specifically, one would tune σ_A such that the expected number of photons does not exceed the observed one (at a certain confidence level). If one knew that a fraction of the observed photons is certainly not due to dark matter, they could subtract this fraction from the total in order to make the constraint stronger. However, this comes at the price of the results losing reliability, because the modeling of astrophysical foregrounds is generally complex and subject to much uncertainty.

In our case, we chose to be very conservative and did not subtract any foreground. Moreover, there exist several expected DM signal sources at a Galactic and extra-Galactic scale and each one has its own modeling challenges and offers a somewhat unique approach to probing the DM parameter space. For our project we focused on the Galactic halo introduced above. This is an ex-

tended source and is expected to produce photons in sizeable amounts from the entire sky, though being brighter at the Galactic Center (GC). However, the GC also has a large number of photons that are coming from astrophysical processes and therefore the strength of the constraint might suffer. This led us to try and introduce algorithms able to select an optimal region of the sky ("Region Of Interest", ROI) and energy range, to obtain the strongest possible limits. This presents a challenge in the fact that the algorithm might pick a data subset that simply happened to have a statistical down-oscillation in the observed photons, which would make the method statistically flawed. In view of this, we opted to use 10 Monte Carlo simulations[1] and created algorithms with a figure of merit that took all the simulations into account at the same time. One approach was to pixellate the sky in various manners and let the algorithm pick the best pixels (the ones yielding the best limits, taken individually) from each simulation and then intersect them. This however failed often to give satisfying results for low-statistic regions. Several methods were tried until we settled on one which constructs the ROIs as simple geometrical shapes parametrized by 3 variables for annihilation and 1 for decays. Then the variables are chosen such that the average constraint over the 10 MCs is the strongest. At this point we were ready to derive the final constraint using the MC-selected ROI on the real data.

This allowed us to improve by about one order of magnitude over similar analyses that used comparable data and methodologies. Also, note that our analysis employs and derives limits for a very broad range of dark matter models, allowing for different halo distributions (DM profiles), final states, Galactic-magnetic-field values, annihilation or decay pathways. A great deal of checks and investigations were performed in order to ensure the reliability of our results. These are mostly contained in the appendices to the chapter, which also feature a discussion of how our results compare with recent similar works or claimed signals.

[1] All the simulations are based on the same physical model and differ only by the randomly generated counts map they produce. See Sec. 2.E.

1.4.2 Light Dark Matter Direct Detection with Scintillating Targets

The second project has been a new proposal to directly detect light dark matter (LDM) particles through low-photon-number scintillation from DM-electron scattering.

The idea was spurred by work done in the past few years (*e.g.* [70]) on searching for LDM using electrons in materials as targets. Traditionally, direct detection experiments have focused on the signal that might come from the dark matter particles scattering off nuclei and making them recoil with enough momentum transfer to trigger a count in the detector (in form of heat, scintillation, ionization, or phase transitions). However, since we expect the dark matter particles in our Galaxy to be non relativistic, when they have a mass significantly smaller than the nuclei, the amount of recoil momentum imparted will be too small to trigger the detector, leaving the sub-GeV end of the dark matter mass parameter space relatively unexplored.

In order to probe those regions (which are theoretically well motivated), one idea was to use electrons as targets, in virtue of their much smaller mass than the nuclei. It has already been shown how constraints for DM-electron scattering cross section ($\sigma_{\chi e}$) could be derived from existing experiments such as XENON10, but to gain sensitivity dedicated experiments are in order. The work cited before suggested using semiconductors as target materials and, as signal, the electrons ionized by the interaction with the dark matter, and captured by an electric field. Since solids have a very high target density they are a favorite class of targets for direct detection experiments and we mostly focused on these, as well.

One of the main challenges for such a project relies in the computation of the expected signal, because the electronic states within a crystal are very large in number and very complex to calculate. Nevertheless, much of this work had been done for the above mentioned article. Our work aimed to propose a similar but orthogonal pathway, where the signal is now constituted by scintillation photons in a semiconductor or insulator.

Scintillation (or luminescence) is a phenomenon that occurs in several different materials (liquids, organic molecules, solids) by which electrons are excited to higher energy states and eventually decay back to the ground state by emitting a photon. The physical processes that intervene between the initial excitation and the final emergence of a photon from the material can be extremely complex and will be described in Sec. 3.2.1. We spent much time considering how to model these and how they would influence our results. In particular we investigated the importance of the role of "excitons". These are spatially correlated electron-hole pairs that are very often involved in the scintillation mechanism. We considered the prospect that these excitons might be an important final state for the initial scattering process and we developed a theory to calculate that. However, we noticed that the amount of phase space that these states take up is very small and therefore can be safely neglected (but see the appendices for a discussion).

The other major ingredient to make our project feasible was to find appropriate devices to detect a signal often constituted by a single photon. This requires a detector with exactly zero dark counts. Fortunately, such detectors are being developed in the present time (*e.g.* MKIDs, TES), though costly and typically requiring cryogenic conditions to operate. Finally, we were able to derive sensitivity limits for our chosen materials and the results are competitive with similar approaches using ionization signal.

Chapter 2

Strong Conservative Limits on Dark Matter indirect detection from the Fermi γ-ray telescope

2.1 Introduction

The *Fermi Gamma-ray Space Telescope* (*Fermi*), through its main instrument, the Large Area Telescope (LAT) [49], has been surveying the γ-ray sky since August 2008 in the energy range from 20 MeV to above 300 GeV (with detected events up to ~ 1 TeV). In addition to γ rays produced by known astrophysical sources, the *Fermi*-LAT can detect photons from postulated decay or annihilation of dark matter (DM) to Standard Model (SM) particles. The possibility that DM can annihilate is particularly motivated by the "WIMP miracle" [15]. Here one hypothesizes the existence of weakly interacting massive particles (WIMPs) with few-GeV to few-TeV masses and weak-scale annihilation cross sections. These WIMPs would have been in thermal equilibrium with the SM sector in the early Universe and they generally produce the observed relic abundance of DM from thermal freeze-out. This suggests that WIMPs could still be annihilating today to SM particles. The annihilation could produce various SM particles, which can either radiate photons, further

decay to other SM particles including photons, or inverse Compton scatter (ICS) off background light, producing high-energy γ rays. Those photons that arrive at the *Fermi*-LAT could then be used to infer properties of the DM particles and their distribution around us.

Many WIMP searches have been performed using *Fermi*-LAT data. Analyses by the *Fermi*-LAT Collaboration and outside groups have searched for monochromatic γ-ray lines [47, 71–76] and continuum γ-ray excesses in the diffuse spectrum from different target regions *e.g.*, dwarf spheroidal galaxies [77–83], clusters of galaxies [84–86], the Galactic halo [80, 87–89], the Inner Galaxy [90–103], the Smith cloud [104, 105], and the extragalactic γ-ray background [106–109]. No undisputed signal of DM has been detected thus far, and the cross-section upper limits from these analyses for DM masses $m_{\rm DM} \lesssim 10$ GeV are approaching the typical cross section required during freeze-out for a WIMP to obtain the observed relic abundance, namely $\langle \sigma v \rangle_{\rm relic} \sim 3 \times 10^{-26}$ cm^3 s^{-1}.

While DM is often thought of as being a stable particle, viable DM candidates only need to be stable on *cosmological* time-scales. In particular, DM lifetimes of the order of the age of the Universe or longer ($\tau_{\rm DM} > 10^{17}$ s) can typically evade cosmological and astrophysical bounds more easily than annihilating DM, such as constraints from Big Bang Nucleosynthesis [110], the extragalactic γ-ray background [111], and re-ionization and the Cosmic-Microwave-Background [112–117]. The more relaxed constraints on decaying DM are a result of the DM decay rate being linear with $\rho_{\rm DM}$, as opposed to quadratic with $\rho_{\rm DM}$ in the case of annihilation.

In this chapter, we will provide conservative DM cross-section upper limits and decay-lifetime lower limits from the *Fermi*-LAT inclusive photon spectrum. The inclusive spectrum is presumably dominated by astrophysical foregrounds in the Milky Way, though DM could contribute to it. We make no attempt at subtracting foregrounds and simply require that any putative DM signal contribute less than the observed flux. A similar idea has been used in other works to derive conservative constraints [87, 89, 90], where the DM signal is maximized until saturating the observed flux. The approach in this chapter

differs from such previous analyses in several ways, resulting in stronger constraints on DM. Firstly, we restrict our regions of interest (ROIs) to have a particular symmetric shape determined by only a few free parameters, and we optimize over these parameters. Secondly, we also optimize the energy range that we use for deriving the constraint. Thirdly, we optimize with respect to the constraint itself and not, for example, the signal-to-noise ratio, and last, we optimize our constraints on 10 simulated data sets, not on the measured data. After finding the optimal ROI on simulated data, we use the real data from that same ROI to find the constraint. We derive constraints in this fashion for various DM-halo shapes and for various annihilation and decay final states. The resulting constraints, while being robust and conservative as no foregrounds have been subtracted, are competitive with other existing constraints and stronger than other conservative bounds obtained by [87, 89, 90].

The chapter is organized as follows. In §2.2 we discuss the calculation of the expected γ-ray flux from DM annihilation and decay. In §2.3 we discuss the event selection, method, simulated data sets, and ROI selection. §2.4 discusses the resulting constraints, while our conclusions are in §2.5. In Appendix 2.A we use our method to calculate the limits on DM-annihilation models that have been invoked to explain an excess of γ rays from the Galactic Center (GC) and Inner Galaxy region. Appendix 2.B presents the optimal ROIs together with the corresponding count spectra for several DM channels. Appendix 2.C discusses the effect on our results of source masking and choosing front-/back-converting events. Appendix 2.D describes the astrophysical assumptions affecting the results that include contributions from ICS. Finally, Appendix 2.E provides more details on the simulated data sets that we use, and Appendix 2.F compares the limits obtained from our simulated data sets with those derived from real data.

2.2 Expected Dark Matter signal

Gamma rays from DM annihilation or decay to SM final states can be produced in two dominant ways. The first possibility, which we refer to as *prompt*,

is from either final-state radiation (FSR) produced by Bremsstrahlung by SM particles or from the decay of hadrons that arise in hadronic final states. The second possibility is from electrons and positrons (produced either directly or at the end of a cascade decay chain) that inverse Compton scatter off background ambient light, which primarily consists of starlight, the infrared background light, and the Cosmic Microwave Background (CMB). This ICS process boosts the energy of the background light to produce γ rays. Unlike prompt radiation, ICS depends on various unknown astrophysical parameters discussed below. Although a sizable contribution to the energy lost by the electrons propagating through the Galaxy consists of synchrotron radiation due to acceleration by the Galactic magnetic field, we note that the synchrotron radiation does not make up a noticeable fraction of the γ rays in the energy range under study, as we only consider DM particles with mass below 10 TeV [118, 119]. We thus do not include it in this study. Moreover, the DM signal can receive additional sizeable contributions due to Galactic substructure, particularly for annihilations [120], but we do not include this effect in our study. This makes our analysis more conservative and model independent in this regard. We now outline the calculation of the DM-initiated γ-ray flux.

2.2.1 Prompt radiation

The differential flux, $\mathrm{d}\Phi_\gamma/\mathrm{d}E_\gamma$, of *prompt* photons coming from DM annihilation within the Milky Way halo is given by

$$\frac{\mathrm{d}\Phi_\gamma}{\mathrm{d}E_\gamma} = \frac{1}{8\pi}\,\frac{\langle\sigma v\rangle}{m_{\mathrm{DM}}^2}\,\frac{\mathrm{d}N_\gamma}{\mathrm{d}E_\gamma}\,r_\odot\,\rho_\odot^2\,J_{\mathrm{ann}}\,, \tag{2.2.1}$$

where $\langle\sigma v\rangle$ is the thermally averaged DM annihilation cross section, m_{DM} is the DM mass, and $\mathrm{d}N_\gamma/\mathrm{d}E_\gamma$ is the photon spectrum per annihilation. We assume $\rho_\odot = 0.4$ GeV/cm^3 is the DM density at the Sun's location in the Galaxy [121, 122] [1], and $r_\odot = 8.5$ kpc is the distance between the Sun and the

[1] A range of values between 0.2 and 0.85 GeV/cm^3 are possible at present though [121–125]. Note that a different value for the local DM density would shift up or down our predictions for DM annihilation and decay by a factor proportional to ρ_0^2 and ρ_0, respectively

GC [126]. The "J-factor" is given by

$$J_{\rm ann} \equiv \int_{\rm ROI} {\rm d}b\, {\rm d}\ell\, {\rm d}s\, \frac{\cos b}{r_\odot} \left[\frac{\rho\left(r(s,b,\ell)\right)}{\rho_\odot}\right]^2 , \tag{2.2.2}$$

which depends on the distribution of DM in the Milky Way halo, $\rho(r)$, where $r \equiv r(s,b,\ell)$ is the Galactocentric distance, given by $r = \sqrt{s^2 + r_\odot^2 - 2sr_\odot \cos\ell \cos b}$, where ℓ and b are the Galactic longitude and latitude, respectively, and s is the line-of-sight distance. The integral is over a particular ROI. For decays we can replace $\langle\sigma v\rangle\rho_\odot^2/2m_{\rm DM}^2$ with $\rho_\odot/\tau m_{\rm DM}$ in Eq. (2.2.1), where τ is the DM decay lifetime, with the J-factor

$$J_{\rm dec} \equiv \int_{\rm ROI} {\rm d}b\, {\rm d}\ell\, {\rm d}s\, \frac{\cos b}{r_\odot} \frac{\rho\left(r(s,b,\ell)\right)}{\rho_\odot} . \tag{2.2.3}$$

Moreover, for decays the ${\rm d}N_\gamma/dE_\gamma$ should be interpreted as the photon spectrum for individual DM particle decays.

We consider four popular DM density profiles: the Navarro-Frenk-White (NFW) [127,128], Einasto [129,130], Isothermal [131], and "contracted" NFW (NFW$_c$) [123,132] with slope values taken from [73].

$$\rho_{\rm Isothermal}(r) = \frac{\rho_0^{\rm Iso}}{1 + (r/r_{s,iso})^2} \tag{2.2.4}$$

$$\rho_{\rm NFW}(r) = \frac{\rho_0^{\rm NFW}}{r/r_s\,(1 + r/r_s)^2} \tag{2.2.5}$$

$$\rho_{\rm Einasto}(r) = \rho_0^{\rm Ein} \exp\left\{-(2/\alpha)\left[(r/r_s)^\alpha - 1\right]\right\} \tag{2.2.6}$$

$$\rho_{{\rm NFW}_c}(r) = \frac{\rho_0^{{\rm NFW}_c}}{(r/r_s)^{1.3}\,(1 + r/r_s)^{1.7}} . \tag{2.2.7}$$

We set $\alpha = 0.17$, $r_s = 20\,{\rm kpc}$ [130,132], and $r_{s,iso} = 5\,{\rm kpc}$ [131]. The normalization $\rho(r_\odot) = \rho_\odot$ fixes $\rho_0^{\rm Iso} \simeq 1.56$, $\rho_0^{\rm NFW} \simeq 0.35$, $\rho_0^{\rm Ein} \simeq 0.08$, and $\rho_0^{{\rm NFW}_c} \simeq 0.24$ in units of GeV/cm^3. Our choice of the functional form and parameters in Eq. (2.2.7) is a representative example of the possibility that, due to adiabatic contraction from the inclusion of baryonic matter, the DM profile might have

for annihilations and decays.

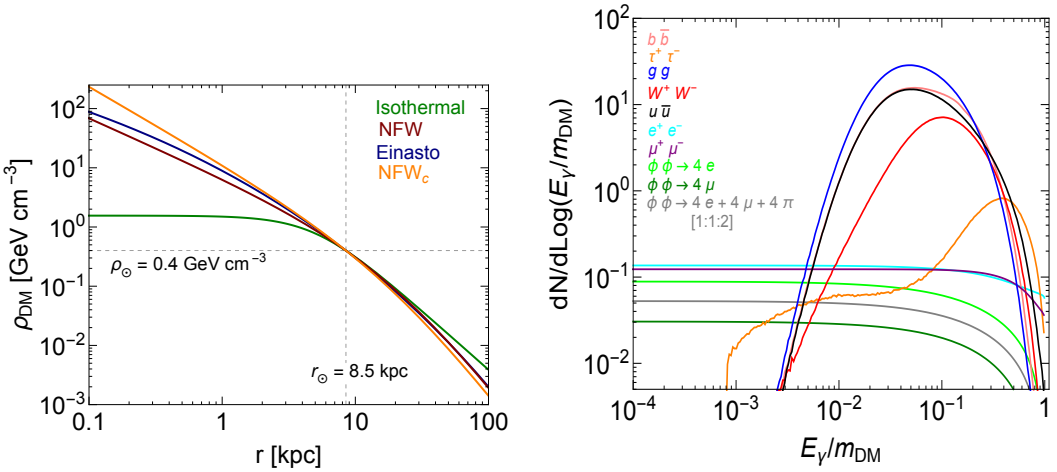

Figure 2.1: **Left:** Dark-matter density profiles versus distance from the Galactic Center (GC). We use the Isothermal (green), NFW (red), Einasto (blue), and a "contracted" NFW (NFW$_c$, orange, with $\rho \propto 1/r^{1.3}$ for $r \to 0$) profile. **Right:** Prompt γ-ray spectra produced in the annihilation of 1 TeV dark matter to e^+e^-, $\mu^+\mu^-$, $\tau^+\tau^-$, $b\bar{b}$, W^+W^-, $u\bar{u}$, gg (g = a gluon), and $\phi\phi$, where ϕ decays either only to e^+e^- (with $m_\phi = 0.1$ GeV), or only to $\mu^+\mu^-$ (with $m_\phi = 0.9$ GeV), or to e^+e^-, $\mu^+\mu^-$, and $\pi^+\pi^-$ in the ratio 1 : 1 : 2 (with $m_\phi = 0.9$ GeV).

a central slope steeper even than that of the NFW or Einasto profiles. The four profiles are shown in Fig. 2.1 (**left**).

The (prompt) photon spectra, $\mathrm{d}N_\gamma/\mathrm{d}E_\gamma$ have been generated with `Pythia 8.165` [133] or are based on formulas in [134–137]. They are the same as in `DMFIT` [138] after the latest update described in [79]. We will consider the ten different final states e^+e^-, $\mu^+\mu^-$, $\tau^+\tau^-$, $b\bar{b}$, W^+W^-, $u\bar{u}$, gg (g = a gluon), and $\phi\phi$, where ϕ decays either only to e^+e^- (with $m_\phi = 0.1$ GeV), or only to $\mu^+\mu^-$ (with $m_\phi = 0.9$ GeV), or to e^+e^-, $\mu^+\mu^-$, and $\pi^+\pi^-$ in the ratio 1 : 1 : 2 (with $m_\phi = 0.9$ GeV) (the latter ratio is motivated if ϕ is a dark photon that kinetically mixes with the SM hypercharge gauge boson). The annihilation channels to $\phi\phi$ are motivated by DM models [139, 140] that attempt to explain the rising positron fraction measured by PAMELA [141], *Fermi* [142], and AMS-02 [51, 143]; the ϕ can also facilitate an inelastic transition between the DM ground state and an excited state [139, 144] to explain e.g., the 511

keV line anomaly [145]. For DM decays, the ϕ channels can be viewed as "simplified models" that can capture how the constraints change when there is a cascade, e.g., [119]. We will sometimes refer to these scalar-mediated processes as "eXciting Dark Matter" (XDM). These spectra are shown in Fig. 2.1 (**right**) in the case of annihilating DM and $m_{\rm DM} = 1$ TeV. We do not consider other popular DM candidates like axions and gravitinos.

We note that the observed differential photon flux can also be written as

$$\frac{\mathrm{d}\Phi_\gamma}{\mathrm{d}E_\gamma} \equiv \frac{\mathrm{d}N_\gamma}{t_{\rm tot}\, A_{\rm eff}\, \mathrm{d}E_\gamma} \equiv \frac{1}{\mathcal{E}} \frac{\mathrm{d}N_\gamma}{\mathrm{d}E_\gamma}\,, \tag{2.2.8}$$

where we have now explicitly included $A_{\rm eff}$, the effective area (which is a function of energy), $t_{\rm tot}$, the LAT's total live time, and $\mathcal{E}$, the LAT's exposure. Given the photon spectra, the number of photons from a DM annihilation signal in a spatial region Ω^i, with J-factor $J^i_{\rm ann}$, and energy range $[E_k, E_{k+1}]$ is given by

$$N^{i,k}_\gamma = \frac{1}{8\pi} \frac{r_\odot \rho^2_\odot}{m^2_{\rm DM}} \langle \sigma v \rangle\, J^i_{\rm ann}\, \mathcal{E}^{i,k} \int_{E_k}^{E_{k+1}} \mathrm{d}E_\gamma \frac{\mathrm{d}N_\gamma}{\mathrm{d}E_\gamma}\,, \tag{2.2.9}$$

where $\mathcal{E}^{i,k}$ is the exposure averaged over Ω^i and calculated at the midpoint of $[E_k, E_{k+1}]$ (since the variation of the exposure over a single energy bin is very small). For decays the predicted counts are

$$N^{i,k}_\gamma = \frac{1}{4\pi} \frac{r_\odot \rho_\odot}{m_{\rm DM}} \frac{1}{\tau}\, J^i_{\rm dec}\, \mathcal{E}^{i,k} \int_{E_k}^{E_{k+1}} \mathrm{d}E_\gamma \frac{\mathrm{d}N_\gamma}{\mathrm{d}E_\gamma}\,. \tag{2.2.10}$$

The approximately homogeneously distributed DM in the Universe could provide an extragalactic contribution to the observed photon flux. However, the observed γ-ray spectrum will be different than that expected from Galactic DM interactions since the photons redshift as they propagate to us and there is a finite optical depth — the result of interactions of the γ rays with low-energy photons that compose the extragalactic background light (EBL). This yields the following expected extragalactic photon intensity for decaying

DM [146, 147]

$$\frac{\mathrm{d}^2\Phi_\gamma}{\mathrm{d}E_\gamma \mathrm{d}\Omega} = \frac{1}{4\pi}\frac{\Omega_{\rm DM}\,\rho_{c,0}}{\tau m_{\rm DM}}\int_0^\infty \mathrm{d}z\,\frac{e^{-\tau(E_\gamma(z),z)}}{H(z)}\frac{\mathrm{d}N_\gamma}{\mathrm{d}E_\gamma}(E_\gamma(z),z)\,. \tag{2.2.11}$$

Here, $\Omega_{\rm DM} \simeq 0.267$ is the present DM energy density, $\rho_{c,0} \simeq 4.7{\times}10^{-6}$ GeV/cm^3 is the critical density today, $E_\gamma(z) = E_\gamma(z+1)$ is the energy of the emitted photon, $H(z) = H_0\sqrt{\Omega_m(1+z)^3+\Omega_\Lambda}$, where $\Omega_m \simeq 0.317$ and $\Omega_\Lambda \simeq 0.683$ are the total matter and cosmological-constant energy densities [148], respectively, and we assume a flat Universe with $\Omega_m + \Omega_\Lambda = 1$. The optical depth is given by $\tau\,(E_\gamma, z)$, and we use the parameterizations found in [146]. We note that, for annihilating DM, the smooth extragalactic contribution is subleading compared to the Galactic one and we ignore it, whereas for decays it is a factor of order $\lesssim 1$ as large as its Galactic counterpart and we include it in our analysis.

2.2.2 Inverse Compton Scattering

We include the flux generated by ICS for the cases where DM annihilates/decays to e^+e^-, $\mu^+\mu^-$, $\tau^+\tau^-$, as well as $\phi\phi$ channels. In all cases we end up with high-energy electrons and positrons. These propagate within the Galaxy and can lose energy through ICS off starlight, infrared background light, or CMB photons, or via synchrotron radiation in the Galactic magnetic field. The ICS process ($e^{\pm\prime}\gamma' \to e^\pm\gamma$) can produce high-energy γ rays that are observed by the LAT. The synchrotron-radiation contribution in the *Fermi*-LAT energy range is subdominant for the DM masses and models that we consider [119] and thus we neglect it when we derive our limits. However, it must be included when calculating the ICS γ-ray signal, since it determines how fast the electrons and positrons cool. In fact, the cooling time is strongly dependent on the Galactic magnetic field, whose values at different locations in our Galaxy are not known very accurately. This leads to large uncertainties in the ICS signal. Moreover, the calculation of the ICS signal requires additional assumptions; for example, we assume, as generally done, that the density of electrons and positrons after propagation follows a steady-state so-

lution. However, phenomena such as the *Fermi* bubbles [149], pointing to a dynamical event in the Milky Way's recent history, might make this assumption not fully justified. We also assume that the steady-state propagation of the electrons/positrons only occurs inside a cylindrical region of the Galaxy that has a maximum radius R_h and half-height z_h. The steady-state diffusion equation is given by (e.g., [150])

$$-D_{xx}\left(E_e'\right)\nabla^2\frac{\mathrm{d}n_e}{\mathrm{d}E_e'}-\frac{\partial}{\partial E_e'}\left[b\left(r,z,E_e'\right)\,\frac{\mathrm{d}n_e}{\mathrm{d}E_e'}\right]=\begin{cases}\frac{1}{2}\left(\frac{\rho(r,z)}{m_{\rm DM}}\right)^2\langle\sigma v\rangle\,\frac{\mathrm{d}N_e}{\mathrm{d}E_e'}, & \text{annihil.}\\ \frac{1}{2}\,\frac{2\rho(r,z)}{m_{\rm DM}}\,\frac{1}{\tau}\,\frac{\mathrm{d}N_e}{\mathrm{d}E_e'}, & \text{decays}\end{cases} \tag{2.2.12}$$

Here $\mathrm{d}n_e/\mathrm{d}E_e' \equiv \mathrm{d}n_e(r,z,E_e')/\mathrm{d}E_e'$ is the energy-dependent differential electron+positron density at a given point in the Galaxy, (r,z), where r and z are the cylindrical coordinates of the electron/positron in the Galaxy. The right-hand side of Eq. (2.2.12) is the source term and contains the DM density profile, $\rho(r,z)$ (a function of cylindrical coordinates) and the electron+positron energy spectrum, $\mathrm{d}N_e/\mathrm{d}E_e'$; also, there is a factor 1/2 for Majorana fermions, otherwise 1 for Dirac fermions. The first term on the left-hand side accounts for the spatial diffusion and is characterized by an energy-dependent coefficient,

$$D_{xx}\left(E_e'\right)=D_0\left(\frac{E_e'}{E_0}\right)^{\delta}. \tag{2.2.13}$$

The second term is the energy-dependent loss and is given by

$$b\left(r,z,E_e'\right)\equiv-\frac{\mathrm{d}E_e'}{\mathrm{d}t}=\frac{4\sigma_T}{3m_e^2}E_e'^2\left[u_B(r,z)+\sum_{i=1}^{3}u_{\gamma i}(r,z)\,R_i(E_e')\right], \tag{2.2.14}$$

where $\sigma_T = 8\pi r_e^2/3$, with $r_e = \alpha_{\rm em}/m_e$, is the Thomson cross section, and $u_B\left(r,z\right) = B^2/2$ is the energy density of the Galactic magnetic field B, chosen to have the form [151]

$$B\equiv B(r,z)=B_0\,e^{-[(r-R_\odot)/R_b+z/z_b]}, \tag{2.2.15}$$

where $R_b = 10$ kpc and $z_b = 2$ kpc. The $u_{\gamma i}(r, z)$ are the energy densities of the three relevant light components in the Galaxy, i.e.: CMB, infrared light, and starlight. The factors $R_i(E'_e)$ take into account relativistic corrections. The γ-ray differential flux at energy E_γ, resulting from ICS off an electron is

$$\frac{\mathrm{d}^2\Phi_\gamma}{\mathrm{d}E_\gamma \mathrm{d}\Omega} = \frac{\alpha_{\rm em}^2}{2} \int \mathrm{d}s \iint \mathrm{d}E'_\gamma \, \mathrm{d}E'_e \, \frac{f_{\rm IC}\,(q,\epsilon)}{{E'_\gamma}^2 E'^2_e} \, \frac{\mathrm{d}n_e}{\mathrm{d}E'_e}\,(r, z, E'_e) \, \frac{\mathrm{d}u_\gamma}{\mathrm{d}E'_\gamma}\,(r, z, E'_\gamma) \quad (2.2.16)$$

where s is the line-of-sight distance, and

$$f_{\rm IC}(q,\epsilon) \equiv 2q\log q + (1+2q)(1-q) + \frac{1}{2}\frac{(\epsilon q)^2}{1+\epsilon q}(1-q)\,, \quad (2.2.17)$$

$$q \equiv \frac{\epsilon}{\Gamma(1-\epsilon)}, \qquad \epsilon \equiv \frac{E_\gamma}{E'_e}, \qquad \Gamma \equiv \frac{4E'_\gamma E'_e}{m_e^2}\,. \quad (2.2.18)$$

We calculate the ICS contribution with `GALPROP V50` [152]. We use a version of `GALPROP V50` that was modified by the authors of [153] to include various DM annihilation and decay final states. We fix $\delta = 0.33$, $E_0 = 4$ GeV, and take the cylindrical geometry to have a maximum radius $R_h = 20$ kpc and a maximum half-height $z_h = 4$ kpc. As mentioned above, the greatest source of uncertainty is due to the Galactic magnetic field, B. To capture some of this uncertainty, we vary B_0 between $1 - 10$ μG, when showing our results in §2.4. We fix the spatial diffusion coefficient parameter to be $D_0 = 4.797 \times 10^{28}$ cm^2/s (6.311×10^{28} cm^2/s) for $B_0 = 1$ μG (10 μG). (See Appendix 2.D for sources for these values.) In Appendix 2.D we show how our results are affected when varying z_h and R_h, in addition to D_0 and B_0; we find that the largest effect on the results comes from the variation of B_0.

2.3 Data sets and methods

We aim to set conservative, robust constraints on the annihilation and decay of DM into various SM final states. We consider the inclusive photon spectrum observed by the *Fermi*-LAT, and use simulated data to first find the "optimal" ROI in the γ-ray sky, i.e. the one that yields the strongest constraint.

We then require the DM signal to be less than the observed photon counts. We note that our approach does not allow us to search for the existence of a DM signal.

In this section we describe the event selection, how we use the simulated data sets in our analysis, the ROI choice, and how we construct optimal upper bounds on the DM annihilation cross section and lower bound on the DM decay lifetime. We also provide a detailed example of our procedure.

2.3.1 Event Selection

The data set used for this study consists of ~ 5.84 years of *Fermi*-LAT data (from August 2008 until June 2014) in the energy range $1.5 - 750$ GeV. We select photons using the `P7REP_CLEAN` event-class selection [154], to minimize contamination by residual cosmic rays. We also require the zenith angle to be smaller than 100° to remove photons originating from the bright Earth's Limb. Details on the *Fermi*-LAT instrument and performance can be found in [49, 155]. All data reduction and calculation of the exposure maps were performed using the *Fermi*-LAT *ScienceTools*, version v9r34p1 [156]. As for the *Fermi*-LAT instrument response functions (IRFs), we use `P7REP_CLEAN_V15` for both MCs and data. As described in Appendix 2.C, the results shown in this chapter are obtained after masking all known point sources identified in the 5-year *Fermi* catalog (3FGL) [157], using a PSF (point spread function)-like masking radius, except for those photons coming from within the inner $2^\circ \times 2^\circ$ square at the GC. Moreover, we include both front- and back-converting events. In Appendix 2.C we show that, although this choice is generally optimal, our results are not significantly affected if we mask only the brightest sources, or no sources at all, and if we include only front- or only back-converting events.

2.3.2 Simulated (Monte Carlo) Data Sets

For our study, we use 10 Monte Carlo (MC) data sets, each a statistically independent ~ 5.84-year representation of the γ-ray sky. The same event selection described above is applied to MC data. We use the simulated data sets

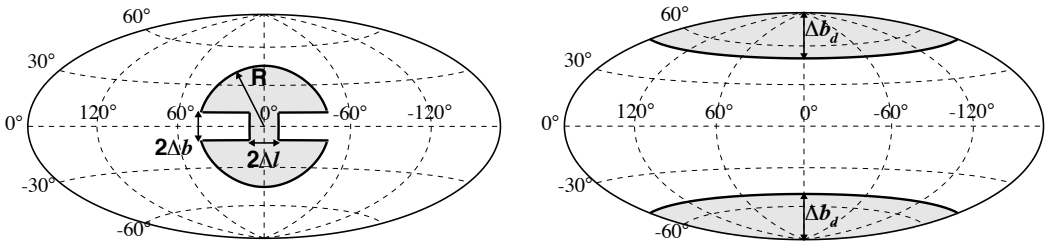

Figure 2.2: **Left:** The choice of ROI (shaded) in the γ-ray sky for dark-matter annihilation. The ROI depends on 3 parameters, as indicated. **Right:** The choice of ROI for dark-matter decays (shaded), which depends on one parameter, as indicated.

to select "optimized" ROIs, independent of the real data, as described below in §2.3.3. By finding optimal ROIs based on the MC simulations, we avoid the possibility of accidentally obtaining a strong constraint due to statistical fluctuations in the data. We describe the details of the simulated data in Appendix 2.E. Note that the MC simulations contain photons with an energy range of 0.5 GeV to 500 GeV (as opposed to 1.5 GeV to 750 GeV in the data). We account for this difference by extrapolating the MC data up to 750 GeV as described in Appendix 2.E.

2.3.3 ROI Choice

We take the ROI for annihilating DM to have the dumbbell shape as shown in Fig. 2.2 (**left**). This shape depends on three parameters: the radius from the GC to the edge of the ROI, R, the width in latitude of the Galactic plane (GP) that is to be excluded from the ROI, $2\Delta b$, and the width in longitude of the GC region that is to be included in the ROI, $2\Delta\ell$. While the Galactic foregrounds are largest in the GC and GP regions, we include the GC in our ROI as this is where the DM signal peaks as well, dramatically so for cuspy profiles (since $N_{\gamma,\mathrm{DM}} \propto \rho^2_{\mathrm{DM}}$). Beyond the GC, the choice of a circular region, parametrized by R, is motivated by the symmetric distribution of DM.

For decaying DM, our choice of ROI will consist of the two high-latitude regions shown in Fig. 2.2 (**right**), and depends on only one parameter: the

width in latitude from the Galactic poles to the edge of the ROI, Δb_d. In contrast to annihilation, the decaying DM signal is expected to be much less concentrated in the GC, since $N_{\gamma,\mathrm{DM}} \propto \rho_{\mathrm{DM}}$.

2.3.4 Optimizing the ROIs and Energy Ranges using Simulated Data

A particular DM model or *Theory Hypothesis*, $T_H = [m_{\mathrm{DM}}, \rho, \text{annihilation/decay}, \text{channel}]$, is characterized by the DM mass (m_{DM}), the DM density profile (ρ), whether it is annihilating/decaying DM, and the annihilation/decay final state. Given any ROI and a photon energy range, [ROI, ΔE], we obtain a constraint on either the DM annihilation cross section, $\langle\sigma v\rangle$, or decay lifetime, τ, for a given T_H by requiring that the number of DM events, $N_{\gamma,\mathrm{DM}}$, in [ROI, ΔE] does not exceed the observed value, $N_{\gamma,O}$. More precisely, to set a limit with a confidence level (C.L.) of $1-\alpha$, we vary $\langle\sigma v\rangle$ or τ until the probability that $N_{\gamma,\mathrm{DM}} > N_{\gamma,O}$ is α; in equations, the bound on $\langle\sigma v\rangle$ or τ is obtained by solving

$$\sum_{k=0}^{N_{\gamma,O}} \mathrm{Poisson}\left(k \,|\, N_{\gamma,\mathrm{DM}}\right) = 1-\alpha, \tag{2.3.19}$$

where as usual

$$\mathrm{Poisson}(k\,|\lambda) = \frac{\lambda^k\, e^{-\lambda}}{k!}\,. \tag{2.3.20}$$

For each T_H, we find the optimal ROI and optimal photon energy range, [ROI, $\Delta E]_O$, which provides the best limit on $\langle\sigma v\rangle$ or τ. If we simply scan over all [ROI, ΔE] in the data, this would subject our constraints to statistical fluctuations. Instead, we use the 10 simulated data sets to find [ROI, $\Delta E]_O$ as follows. For the i-th ROI and energy range, [ROI, $\Delta E]_i$, and j-th simulated data set, we calculate the bound on the cross section or lifetime, $\langle\sigma v\rangle_{i,j}$ or $\tau_{i,j}$, as described above in Eq. (2.3.19). We then average the resulting expected

limit across the 10 simulations, i.e.

$$\overline{\langle\sigma v\rangle}_i = \frac{1}{10}\sum_{j=1}^{10}\langle\sigma v\rangle_{i,j}\,, \tag{2.3.21}$$

$$\overline{\tau}_i = \frac{1}{10}\sum_{j=1}^{10}\tau_{i,j}\,. \tag{2.3.22}$$

We then find [ROI, $\Delta E]_O$ by scanning over all [ROI, $\Delta E]_i$'s and selecting the one that yields the minimum $\overline{\langle\sigma v\rangle}_i$ (maximum $\overline{\tau}_i$), i.e.

$$\overline{\langle\sigma v\rangle} = \min_i \overline{\langle\sigma v\rangle}_i\,, \tag{2.3.23}$$

$$\overline{\tau} = \max_i \overline{\tau}_i\,. \tag{2.3.24}$$

We then use [ROI, $\Delta E]_O$ on the real data to calculate the limits on $\langle\sigma v\rangle$ or τ for the given T_H.

The ROIs used in our optimization are given in §2.3.3. We bin each simulated data set into $0.18^\circ \times 0.18^\circ$ rectangular pixels in Galactic latitude and longitude and $N = 127$ logarithmically-uniform energy bins between $1.5 - 750$ GeV. We then vary the ROI shape parameters described in §2.3.3 in steps of 0.5° for R, steps $\sim 1^\circ$ for Δb and $\Delta\ell$, and 2.5° for Δb_d. For each choice of ROI, we scan over all $(N-1)(N-2)/2 = 8064$ choices of adjacent bins in energy, assuming a minimum of three adjacent bins. In Appendix 2.B we show a sample of the resulting optimized ROIs and energy ranges.

We note that for large enough $N_{\gamma,\mathrm{DM}}$ or $N_{\gamma,O}$, the statistical distributions are approximately Gaussian, and we would obtain a 95% C.L. bound by requiring $N_{\gamma,\mathrm{DM}} < N_{\gamma,O} + 1.64\sqrt{N_{\gamma,O}} \simeq N_{\gamma,O}$. Even our smallest optimal ROIs with the highest optimal energy ranges contain at least $\mathcal{O}(10)$ photons. Our method thus does not produce constraints that are susceptible to Poisson fluctuations of the number of events in [ROI, $\Delta E]_O$, and, as a consequence, our constraints are not expected to improve significantly with more data (some small improvements may arise from, e.g., a better rejection of backgrounds).

We also note that since [ROI, $\Delta E]_O$ was selected using simulated data,

other choices of [ROI, ΔE] may provide a stronger constraint on the data. Also, the simulated data is not a perfect representation of the data. Indeed, there are certain regions in the sky where the simulations do not model the data perfectly, and the "expected" limits using MC data may differ from the limit obtained on the real data (see Appendix 2.F). One notable example is in the GC and in the Inner Galaxy region, which has led to claims of a γ-ray excess, see Appendix 2.A. However, an imperfect modeling of the sky does not affect the validity of our constraints. We use the simulations as a tool to pick [ROI, ΔE] in an unbiased way. Even if the simulations were a totally inaccurate representation of the real data, it would not *invalidate* our limits, although other choices of [ROI, ΔE] would provide stronger constraints.

We note that for prompt radiation we include the effects of the *Fermi*-LAT's PSF, by performing its convolution with the J-factors, using the *Fermi*-LAT *ScienceTools*. For the constraints that include prompt and ICS, however, convolving the PSF for the DM signal calculation is computationally intensive, so we do not account for these effects. To see by how much this could potentially affect our limits, we constrained the ROIs to have a shape which is safe w.r.t. the PSF containment radius at the lowest energies considered. If the ROI includes a portion of GC (i.e. $\Delta\ell > 0^\circ$), then we require the width of this window to be at least 6° (i.e. $\Delta\ell > 3^\circ$); for the width of the top and bottom of the ROI shape (resembling crescents) we require that $R < \Delta\ell$ (so the ROI is a circle), $R < \sqrt{\Delta b^2 + \Delta\ell^2}$ (so the two crescents have no tips), and $R > 4^\circ + \Delta b$ (so the two crescents are thick enough). The upper bounds thus obtained are only degraded by at most $\sim 20 - 40\%$ with respect to the unconstrained-ROI case. This is a small number; especially in view of the fact that the largest uncertainty for the DM ICS signal comes from the value of the magnitude of the local magnetic field, see Appendix 2.D.

We note that systematic effects of the PSF are not included in our analysis, as they are much smaller than the other sources of systematic uncertainty considered, such as in the ICS signal and DM density profile.

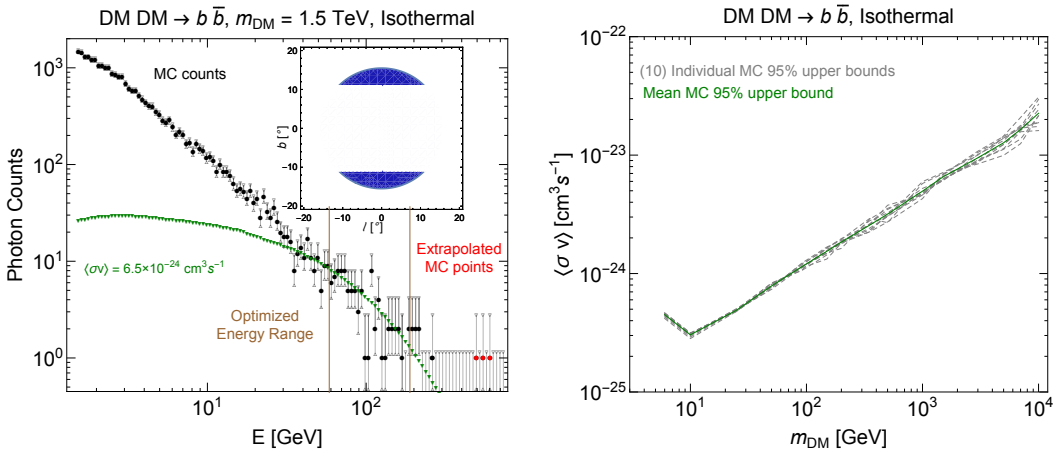

Figure 2.3: **Left:** Count spectrum from one of the MC data sets for the ROI shown in the inset. The green points show the spectrum for 1.5 TeV DM distributed according to the Isothermal profile, annihilating to $b\bar{b}$, with a cross section chosen such that the number of signal events in the energy range from 68 GeV to 142 GeV (vertical brown lines) is larger than the number of events in the MC data (at 95% C.L.), as given by Eq. (2.3.19). Since the simulated data only contains photons up to 460 GeV, we extrapolate it to 750 GeV (red points), using a power-law fit to the photon spectrum above ~ 6.2 GeV. See Appendix 2.E for more details. **Right:** The best cross-section limit averaged over all ten MC data sets is shown with a green solid line, while the individual cross-section limits for each of the 10 MC data sets are shown with dashed gray lines. As explained in §2.3.5, the average cross-section limit is used as a figure of merit for our ROI/energy range optimization.

2.3.5 Illustration of Procedure

An illustration of our method is shown in Fig. 2.3. The left plot shows the count spectrum from one of the MC data sets for the ROI shown in the inset. The green triangles show the spectrum for a 1.5 TeV DM annihilating to $b\bar{b}$, assuming isothermally distributed DM, with the cross section set at the 95% C.L. upper limit. This limit is derived by requiring that the number of signal events in the optimal energy range from 68 GeV to 142 GeV (vertical brown lines) be larger than the number of events in the MC data as given by Eq. (2.3.19), where we set $\alpha = 0.95$. The number of events in this ROI and energy range will fluctuate from one MC data set to another, and we calculate

the average cross-section limit for all ten MC data sets. We show the best average cross-section limit as a function of DM mass with a green solid line in Fig. 2.3 (**right**), together with the cross-section limit for the ten individual MC data sets (dashed gray lines). In Fig. 2.3, we masked all point sources and included both front- and back-converting events.

We now have all the ingredients put in place for calculating constraints from the γ-ray sky observed by the *Fermi*-LAT. In the next section we give the 95% C.L. bounds on the annihilation cross section (upper bound) and on the DM lifetime (lower bound) for annihilations and decays into various SM modes, respectively.

2.4 Results and discussion

In this section we give the results from the optimization procedure described in §2.3. We emphasize that the constraints obtained in this study are conservative and robust, since they do not depend on the modeling and subsequent subtraction of astrophysical foregrounds. In §2.4.1 (§2.4.2) we discuss the constraints on annihilating (decaying) DM. Additionally, in Appendix 2.A we use our method to derive bounds on models invoked to explain a putative γ-ray excess at the GC [92–103]. The effect on our constraints due to different choices of source-masking, and due to the variation of ICS parameters is discussed in Appendix 2.C and Appendix 2.D, respectively.

2.4.1 Constraints on Dark Matter Annihilation

The constraints on the DM-annihilation cross section as a function of DM mass are presented in Fig. 2.4 for annihilation to e^+e^-, $\mu^+\mu^-$, $\tau^+\tau^-$, and $\phi\phi$, where ϕ decays either only to e^+e^- (with $m_\phi = 0.1$ GeV), or only to $\mu^+\mu^-$ (with $m_\phi = 0.9$ GeV), or to e^+e^-, $\mu^+\mu^-$, and $\pi^+\pi^-$ in the ratio $1:1:2$ (with $m_\phi = 0.9$ GeV). Fig. 2.5 shows the results for the final states $b\bar{b}$, W^+W^-,[2] $u\bar{u}$,

[2]Note that limits for the W^+W^- channel extend to $m_{DM} < m_W$. In this region, the W^+W^- final state is not produced on-shell, but instead the annihilation is to a three- or four-body final state consisting of leptons and/or quarks through off-shell $W^\pm$. (The

and gg. In all cases we present the results for four different assumptions about the DM profile $\rho(r)$ introduced in §2.2.1. We note that each DM mass for each spatial distribution and final state choice has been separately optimized, and an optimal ROI, $\mathrm{ROI}_{o,i}$, and photon energy range, $\Delta E_{o,i}$, were obtained to set the 95% C.L. constraint. In Appendix 2.B we illustrate how the optimal ROI and energy range change for various DM density profiles and for different DM masses (see Figs. 2.A.2 and 2.A.3).

The constraints disfavor the thermal WIMP cross section for low DM masses and for the cuspiest profiles (mostly the NFW_c profile). For those cases in which the final states contain high-energy electrons, i.e. Fig. 2.4, there is a contribution from prompt radiation from FSR as well as ICS. The latter, while more uncertain, considerably strengthens the bounds, especially for high DM masses. In Fig. 2.4 the shaded band denotes the constraint from ICS as the magnitude of the Galactic magnetic field at our Solar System's location, B_0 is varied from 1 μG to 10 μG and correspondingly the diffusion coefficient D_0 from 4.797×10^{28} cm^2/s to 6.311×10^{28} cm^2/s (see §2.2.2). The propagation was performed as described in §2.2.2, i.e. over a cylindrical geometry with radius $R_h = 20$ kpc and half-height $z_h = 4$ kpc. With ICS included and for cuspy profiles, DM annihilation to leptonic final states, particularly for electrons, can be probed well into the annihilation-cross-section regime of a thermal relic that freezes out early in the Universe, $\langle \sigma v \rangle_{\mathrm{relic}} \approx 3 \times 10^{-26}$ cm^3/s. The inclusion of extra particle content in DM annihilations, namely the particle ϕ, is motivated by the best fit to the PAMELA, *Fermi*, and AMS-02 cosmic-ray positron and electron data [51, 141–143], if those excesses are interpreted as coming from DM annihilation. Fig. 2.4 shows the approximate regions (shaded gray) in the cross-section–versus–mass plane, in which annihilating DM could offer an explanation for these excesses. These regions are meant to be illustrative only and chosen so that they contain the parameter choices found in [158], shown with black dots. (See also [159].) The inclusion of ICS severely constrains

expected cross-section in any concrete DM model for the off-shell process would be highly suppressed compared to the on-shell process.)

the favored parameter regions for all profiles except isothermal, while including only the prompt signal challenges the favored regions only for the cuspy NFW_c profile.

The constraints from [79], which, using 4 years of P7REP data, analyzed 15 dwarf spheroidal satellite galaxies (dSph) of the Milky Way to set robust constraints on DM, are shown in Fig. 2.4 with a cyan dashed line. Due to the dSph's proximity, high DM content, and lack of astrophysical foregrounds, they are excellent targets to search for annihilating DM. Moreover, the available data on the velocity distribution of the stars in the dSph allows one to predict rather accurately the expected γ-ray flux from DM annihilation. This prediction is not subject to the same uncertainties as the expected flux in the Milky Way halo, which suffers from large uncertainties in the DM density profile. Our constraints are stronger than the dSph constraints over much of the DM mass range and for several of the DM profiles that we consider, especially at high energies. For DM masses $\lesssim 10$ GeV, our constraints are stronger than the dSph constraints for the NFW_c profile, and comparable in strength for the Einasto profile, although weaker for the NFW and isothermal profiles. New results using P8 data to perform a similar analysis of the dwarf galaxies are expected soon and are somewhat more stringent than the P7REP results.

Notice that some of the ICS-inclusive limits are actually weaker than the ones with prompt radiation only. This might seem puzzling, as for a given ROI and energy range, the signal that includes prompt and ICS is obviously larger than the one with prompt only and should lead to more stringent constraints. However, our ROI and energy range used to derive the limits from the data are dictated by the optimization of the average MC limit, such that the optimized ROIs and energy ranges for prompt+ICS and prompt-only might differ from each other. If one considers this along with the fact that the simulated data sets are not perfect representations of the real sky, the limit that includes ICS can be weaker on occasion than the prompt-only limit.

It is useful to compare our limits with those obtained from similar analyses in the literature where no attempt was made to model the astrophysical foregrounds. These analyses usually differ in their choice of DM-profile pa-

rameters, their procedure for constructing the limits (Gaussian error on flux versus Poisson limit on counts), their choice of propagation models for the ICS signal, and the data energy range utilized. Nevertheless, we can try to single out the effect of our ROI and energy-range optimization method alone by rescaling these other results to compensate for the different choices mentioned above. In [88], the limit was also constructed by scanning over a few differently shaped and located ROIs. Consequently our results are only within a factor of 1-2 stronger than theirs, across all channels. In [89], the construction of the bound is quite different from ours, and our results are around 2 times more stringent than theirs. In [87], an optimization procedure is performed on ROIs that look very different from ours, and a less extensive optimization is done on the energy window. For annihilations we improve on these limits by a factor of 1–20, depending on channel and profile, and by a factor 2–4 when including ICS. In [90], the ROI is optimized using the signal-over-background ratio as a figure of merit. For harder spectra, our improvement is between a factor of 3–8, while for softer spectra, the improvement is a factor of 1–4.

2.4.2 Constraints on Dark Matter Decays

While a favorite target for the DM annihilation rate comes from the thermal freeze-out of a thermal relic, which gives the correct present-day abundance, for decaying DM no such "favored" lifetime exists — the DM lifetime only has to be larger than the age of the Universe. One possible target comes from explaining the rising fraction in the cosmic-ray positron spectrum with DM decays to final states that produce high-energy electrons and positrons, with the preferred DM lifetime being in the range $10^{26} - 10^{27}$ s, depending on the precise final states and astrophysical assumptions [88, 119, 161–167]. Such lifetimes do not only have a phenomenological motivation, but also arise naturally for TeV-scale DM particles that decay via a dimension-six operator generated near the scale of Grand Unified Theories (GUT's), $M \sim 10^{16}$ GeV,

namely

$$\tau \sim 8\pi \frac{M^4}{m_{\rm DM}^5} \sim 2 \times 10^{26}\ {\rm s} \left(\frac{1\ {\rm TeV}}{m_{\rm DM}}\right)^5 \left(\frac{M}{10^{16}\ {\rm GeV}}\right)^4 . \qquad (2.4.25)$$

For example, in [161] DM decaying via dimension-six operators in supersymmetric GUT's were posited to explain the cosmic-ray data from PAMELA.

The results for DM decays to leptonic and $\phi\phi$ final states are included in Fig. 2.6, whereas those decays to $b\bar{b}, u\bar{u}, gg, W^+W^-$ are shown in Fig. 2.7. We only show the constraints for the NFW profile, as the other profiles lead to virtually identical constraints. As in the case for DM annihilation, we include ICS for decaying DM for the leptonic final states only. The additional ICS component, while very sensitive to the value of the Galactic magnetic field, can enhance the constraints significantly, as in the case for annihilating DM. Note that the bounds from prompt radiation start to deteriorate near DM masses of 1.5 TeV due to the maximum-energy selection of 750 GeV used in this study. Our constraints compare favorably with existing constraints in the literature; for example, they are a factor of 2–3 stronger compared to [87–89].

While the DM decay lifetime can span an enormous range consistent with all astrophysical data, there are many scenarios that are being probed by the constraints presented in this analysis. In particular, Fig. 2.6 shows with a gray shaded parallelogram the vaguely approximate preferred regions in which decaying DM can explain the cosmic-ray positron and electron data. Black dots indicate the best-fit regions found in [160], although note that these results do not include the latest data release from AMS-02 [143] (a more careful analysis of the preferred regions is beyond the scope of this chapter); nevertheless, we expect that the preferred regions would not shift significantly, and our regions are meant to be taken as a useful but rough qualitative guide only. We see that decays to $\tau^+\tau^-$ are thoroughly disfavored, but our constraints for other channels are not strong enough to probe the relevant parameter regions.

2.5 Conclusions

In this chapter we presented a conservative method for setting constraints on γ rays originating from DM annihilation and decay, which does not rely on modeling of astrophysical foregrounds when setting a limit. Optimal regions in the sky and energy were obtained by using simulations of the γ-ray sky, and a constraint was found by only requiring that the DM signal does not over-predict the observed photon counts.

For models of both annihilating and decaying DM, this method allows us to constrain theoretically-motivated parameter regions. For example, for cuspy enough profiles (e.g., contracted NFW), our method is able to disfavor the thermal-relic cross section for some leptonic and hadronic final states. Also, for steep-enough profiles, our constraints disfavor various annihilating DM scenarios designed to explain the PAMELA/*Fermi*/AMS-02 cosmic-ray positron and electron data. For decaying DM, a wide range of lifetimes are excluded for various SM final states, including the preferred parameter regions for DM decaying to $\tau^+\tau^-$ to explain the PAMELA/*Fermi*/AMS-02 data. The conservative constraints obtained in this study are often competitive with, and in many cases stronger than, other available constraints in the literature.

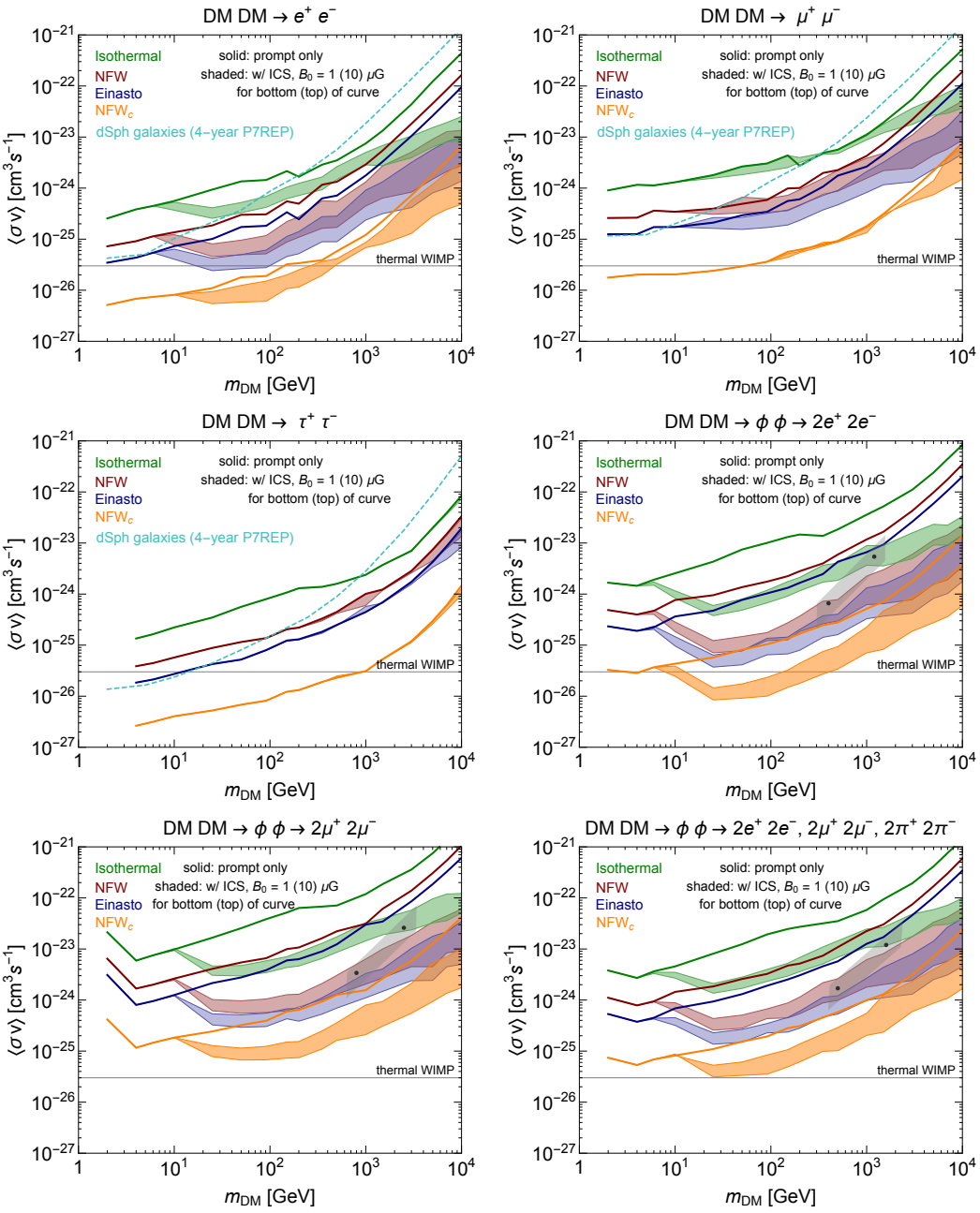

Figure 2.4: 95% C.L. upper limits on DM annihilation cross section vs. DM mass from *Fermi*-LAT's inclusive photon spectrum for the indicated final states. Each plot shows constraints for the Isothermal (green), NFW (red), Einasto (blue), and NFW$_c$ (orange) DM density profiles. Solid lines show constraints from the inclusion of only the prompt radiation from the annihilation, while the bands include the ICS off background light, with the Galactic B-field varying within $1-10$ μG and D_0 within $D_{0,\rm min} - D_{0,\rm max}$ (bottom-top of band). When available, we show the limits from the P7REP analysis of 15 dwarf spheroidal galaxies with a cyan dashed line [79]. For the XDM models we show the approximate regions (gray) in which annihilating DM could account for the PAMELA/Fermi/AMS-02 cosmic-ray excesses. The best-fit parameters from [158] are shown as black dots.

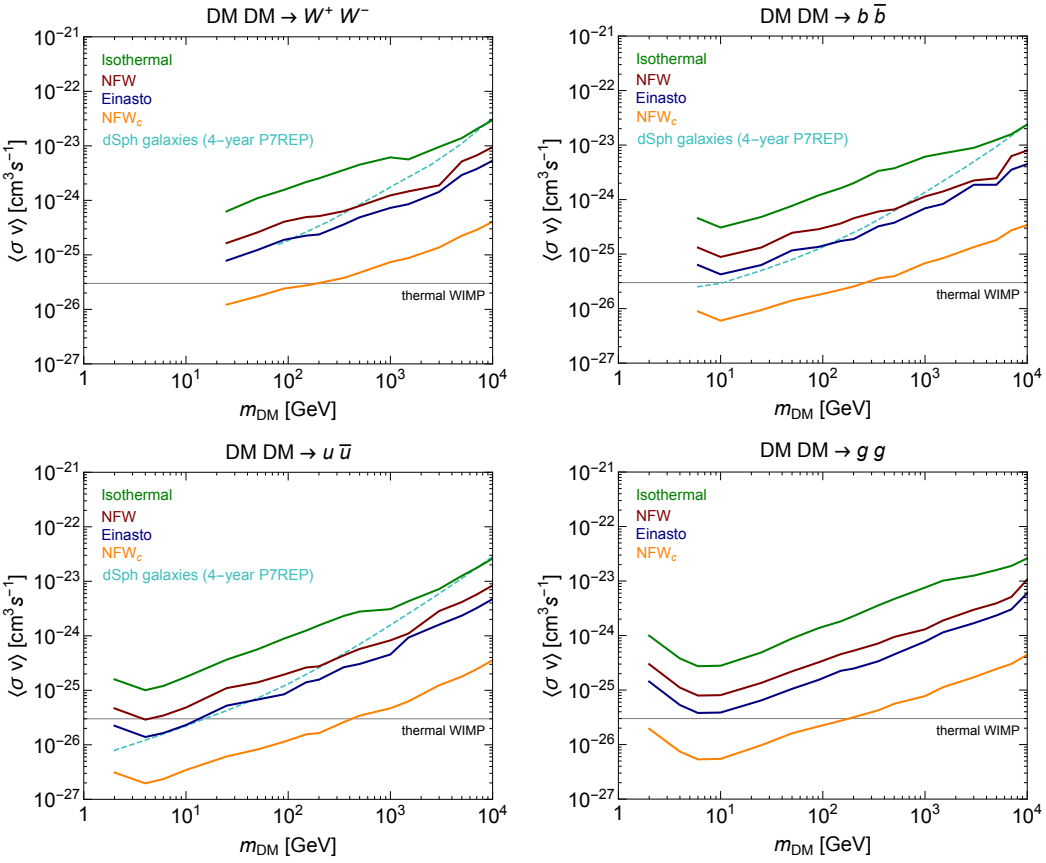

Figure 2.5: 95% C.L. upper limits on DM annihilation cross section vs. DM mass from *Fermi*-LAT's inclusive photon spectrum for the indicated final states. Each plot shows constraints for the Isothermal (green), NFW (red), Einasto (blue), and NFW$_c$ (orange) DM density profiles. Solid lines show constraints derived from including only the prompt radiation produced in the annihilation process (i.e. final-state radiation or in the decay of hadrons). When available, we show the limits from the 4-year P7REP analysis of 15 nearby dwarf spheroidal galaxies with a cyan dashed line [79].

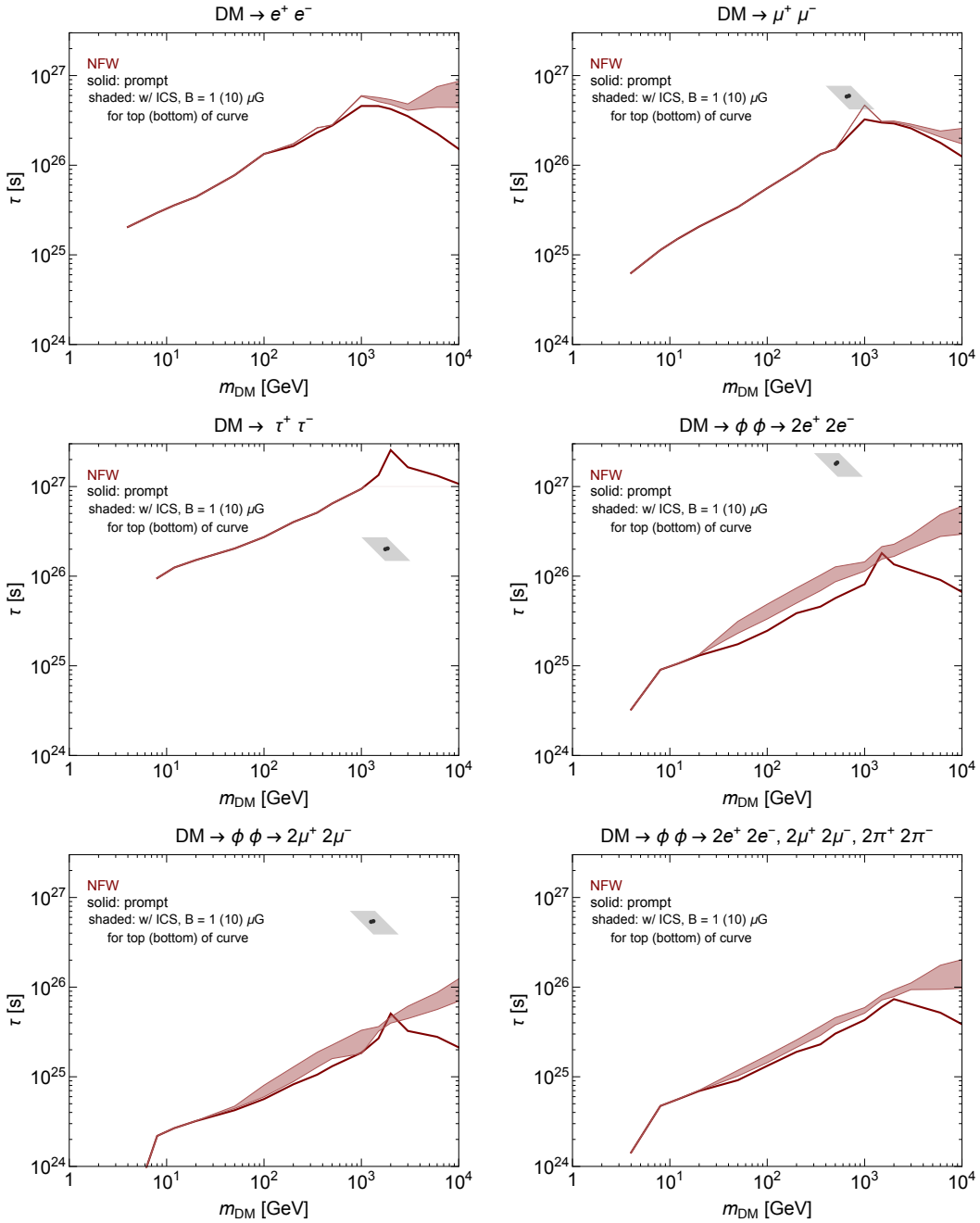

Figure 2.6: 95% C.L. lower limits on DM decay lifetime vs. DM mass from *Fermi*-LAT's inclusive γ spectrum for the indicated final states. Shown are constraints for the NFW profile (other profiles are very similar). Solid lines show constraints derived from including only the prompt radiation produced in the annihilation process (i.e. final-state radiation or in the decay of hadrons), while the bands include the ICS off background light, with the Galactic B-field varying within $1-10$ μG and D_0 within $D_{0,\rm min} - D_{0,\rm max}$ (bottom-top of band). For some models we show the approximate regions (gray) in which decaying DM could account for the PAMELA/Fermi/AMS-02 cosmic-ray excesses. The best-fit parameters from [160] are shown as black dots.

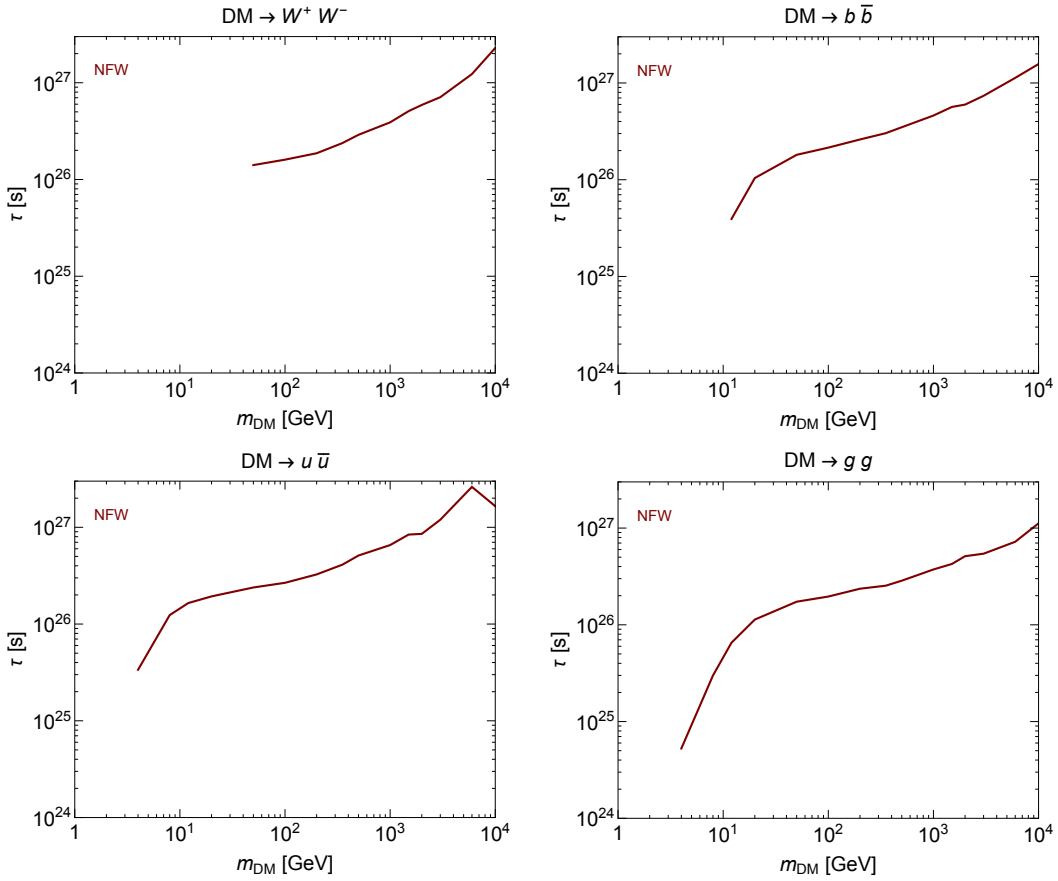

Figure 2.7: 95% C.L. lower limits on DM decay lifetime vs. DM mass from *Fermi*-LAT's inclusive photon spectrum for the indicated final states. Shown are constraints for the NFW profile (the other profiles are virtually identical). The constraints are derived from including only the prompt radiation produced in the annihilation process (i.e. final-state radiation or in the decay of hadrons).

Appendix

2.A Constraints on DM Models invoked to explain γ Rays from Inner Galaxy

In this appendix we address claims made by several groups in recent years regarding a γ-ray excess from ~ 300 MeV to ~ 5 GeV, peaking in the 1–3 GeV window, in the Inner Galaxy [92–103]. While modeling uncertainties are large and the excess may very well have a non-DM origin, we use our method to set constraints on DM scenarios that have been invoked to explain the excess. Since we perform no foreground subtraction, *a priori* we do not expect the limits derived with our method to disfavor the best-fit DM scenarios found in the literature; nevertheless, it is worthwhile to perform a careful check.

The best fit for WIMP DM found in [99, 100] is for $\sim 30 - 40$ GeV DM annihilating predominantly to $b\bar{b}$. Furthermore, the spatial distribution of the putative signal is best fit by a generalized NFW profile,

$$\rho_{\mathrm{NFW},\,\gamma}(r) \;=\; \frac{\rho_0}{(r/r_s)^{\gamma}\,(1+r/r_s)^{3-\gamma}}\,, \tag{2.A.26}$$

with a χ^2 best fit obtained for $\gamma \approx 1.26$, although any γ in the range $\sim 1.1-1.4$ allows for a reasonable fit. Analyses by other groups give results that are broadly consistent with the findings in [99, 100]. In [102], it was found that DM annihilating dominantly to $b\bar{b}$ but with some admixture of $\tau^+\tau^-$ also provides a good fit. Other annihilation channels may also be possible [168].

In Fig. 2.A.1 we show the results of our optimization procedure applied to

generalized NFW, Eq. (2.A.26), with parameters chosen from best fits found in [98, 100, 103] (which differ in part from the assumptions made in §2.4.1). The authors of [100] ([103]) exclude from their analysis a band around the GP defined by $|b| < 1^\circ$ (2°), thus not specifying a specific DM distribution within this latitude. We therefore use our usual ROIs shown in Fig. 2.2, but mask a square centered on the GC of side 2° (4°). We show DM annihilating to $b\bar{b}$ (**left plot**) and $\tau^+\tau^-$ (**right plot**). Unsurprisingly, the bounds that we obtain on the annihilation cross section are still a factor of ~ 3 or more from probing the best-fit regions shown with open or closed contours in Fig. 2.A.1. As a reference for the reader, adopting all the assumptions in [100], for annihilation into $b\bar{b}$, and choosing $m_{DM} = 25$ GeV, the optimal ROI found with our method is determined by the following parameters: $R = 2^\circ$, $\Delta b = 1.98^\circ$, $\Delta \ell = 0.54^\circ$, while the optimal energy range is 1.9 GeV$\lesssim E \lesssim$ 4.0 GeV.

2.B Dependence of Optimal ROI and Energy Range on DM Profile and DM Mass

The optimal ROI and photon-energy range are found separately for each choice of DM spatial distribution, mass, and final state. In this section, we briefly illustrate the generic features of the optimal search region and its dependence on the theory hypothesis. Fig. 2.A.2 shows the obtained ROI and energy range for DM annihilation to $b\bar{b}$ for each of the four spatial distributions studied, and for a fixed DM mass of 25 GeV. For this final state, with the exception of NFW$_c$, where it is beneficial to look near the GC, the optimal regions in the sky involve semi-circular regions, symmetric in latitude b, with the GC removed. Furthermore, we find narrower optimal energy ranges for NFW$_c$-distributed DM.

For the $b\bar{b}$ final state, the effect of varying the DM mass is addressed in Fig. 2.A.3, where the optimal regions are shown for two different masses: 350 GeV and 7 TeV, assuming NFW$_c$-distributed DM. As the DM mass is increased, the strongest optimal regions are obtained by including semi-circular

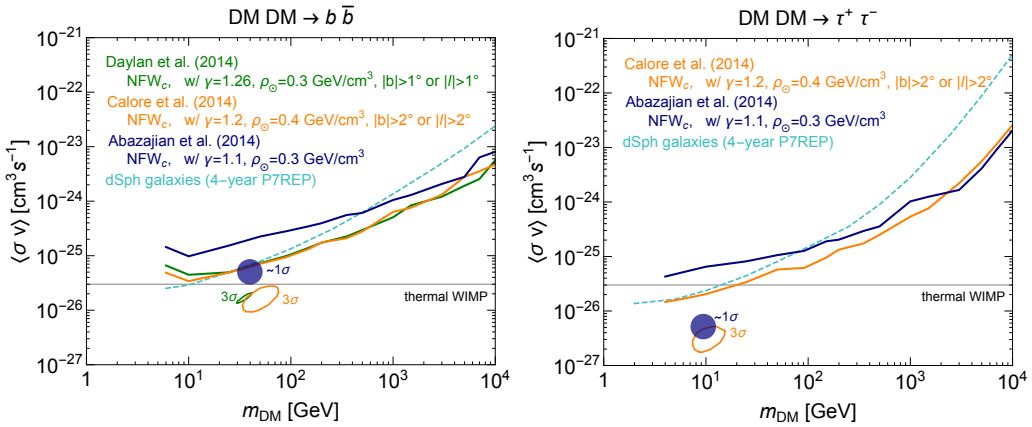

Figure 2.A.1: 95% C.L. annihilation cross section upper limits on DM annihilating to $b\bar{b}$ (**left**) and $\tau^+\tau^-$ (**right**) for an NFW$_c$ profile with various inner slopes and local DM densities (note that the assumptions made in deriving these limits differ in part from those made in §2.4.1). Also shown are the preferred regions from [98, 100, 103] for DM to fit the claimed Galactic-Center γ-ray "excess". The constraints have been computed with the same model assumptions as the best-fit regions (including masking a square centered on the GC of side 2° or 4° for analyses that excluded a band around the GP with the same thickness – see text for details). We also show with a cyan dashed line the limit obtained from the 4-year P7REP analysis of 15 nearby dwarf spheroidal galaxies [79].

regions in latitude, in addition to a rectangular area around the GC. We note that finite-resolution effects were included, by convolving the instrument's PSF with the J-factors, in the DM signal for all of the results in Fig. 2.A.2 and Fig. 2.A.3.

2.C Effect of Source Masking and Choice of Front-/Back-converting events on Limits

In this appendix we investigate the effect on the DM-cross-section upper limits when masking known point sources and using front- and/or back-converting events.

Masking known sources reduces the observed counts in an ROI and can

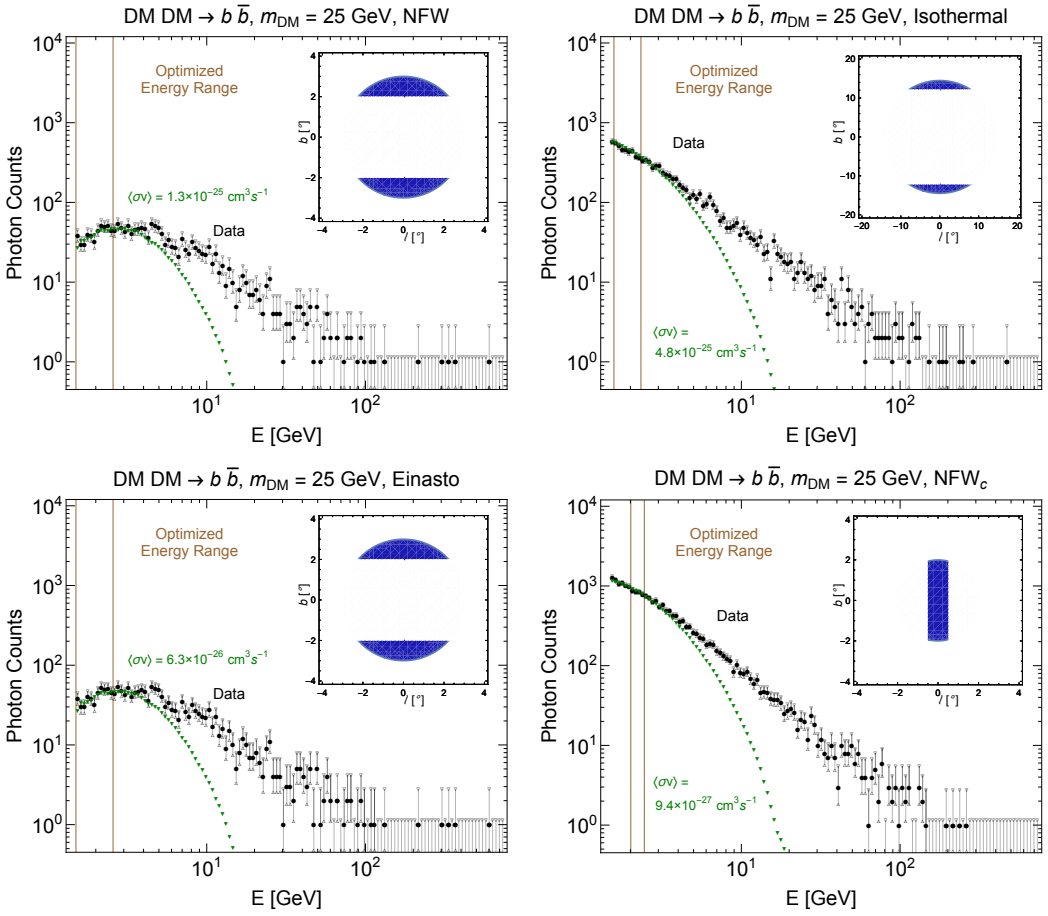

Figure 2.A.2: Count spectrum for 25 GeV DM annihilating to $b\bar{b}$ for various DM density profiles. The vertical (brown) lines show the optimal energy range for each DM model assumption. The inset shows the optimal ROI. Note that PSF-convolution effects were included for the DM signal. The quoted $\langle\sigma v\rangle$ is the annihilation cross section that saturates the 95% C.L. from the data.

strengthen the DM constraints, assuming that the masking does not also remove much of a potential DM signal. This is the case if the ROI is large, as it is expected to be for decaying DM, or for annihilating DM with shallow DM density profiles (e.g., isothermal). Since astrophysical point sources at very large energies (> 20 GeV) typically exhibit a small flux, their masking is expected to improve the limits for lower DM masses. For very cuspy profiles the ROIs tend to be small and concentrated around the GC region, where the number of known sources is also large; in this case, masking all the point

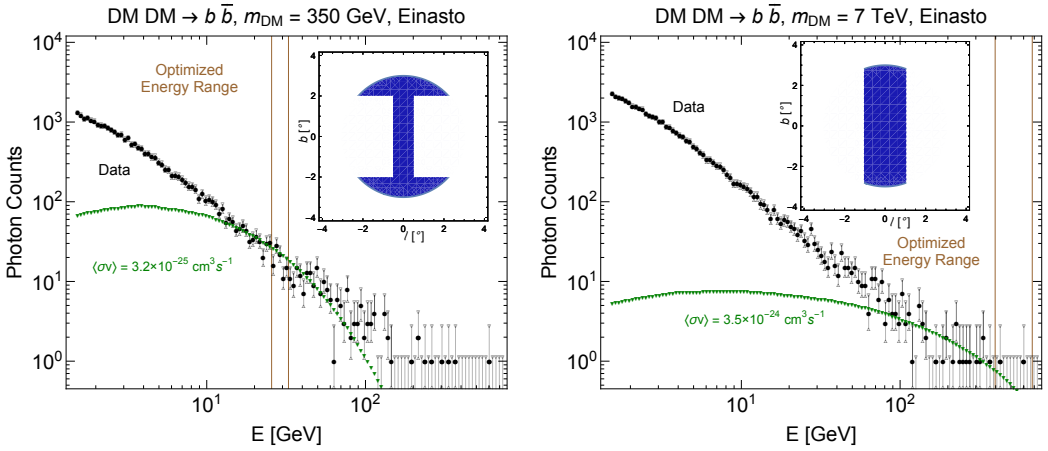

Figure 2.A.3: Count spectrum for 350 GeV (**left**) and 7 TeV (**right**) DM annihilating to $b\bar{b}$, assuming an Einasto profile. The vertical (brown) lines show the optimal energy range for each DM-model assumption. The inset shows the optimal ROI. Note that PSF-convolution effects were included for the DM signal. The quoted $\langle\sigma v\rangle$ is the annihilation cross section that saturates the 95% C.L. from the data.

sources would remove most of the DM signal as well and will thus not likely lead to stronger limits.

The amount of sky that needs to be masked to remove a point source depends on the *Fermi*-LAT PSF, which depends on the energy and on where the photon converts in the detector. In particular, photons that convert to an e^+e^- pair in the front part of the *Fermi*-LAT (consisting of the first 12 layers of thin tungsten foil) have a better angular resolution (smaller PSF) than those photons that convert in the back (next 4 layers of thick tungsten foils). For very cuspy profiles the choice of including only front- or only back-converting events, or both, could potentially have important effects on the constraints.

We obtain the point-source coordinates from the 3FGL catalog [157] and exclude all the photons contained in pixels whose center lies within an angular radius of $2\,\theta_{68}(E)$ from any point source; here θ_{68} is an approximation of the energy-dependent P7REP 68% point-source containment angle,

$$\theta_{68}(E)[^\circ] = \sqrt{c_0^2\,(E/1\,\mathrm{GeV})^{-2\beta} + c_1^2}\,, \tag{2.C.27}$$

and the parameters for (front-, back-) converting events are $c_0 = (0.645, 1.103)\,, c_1 =$

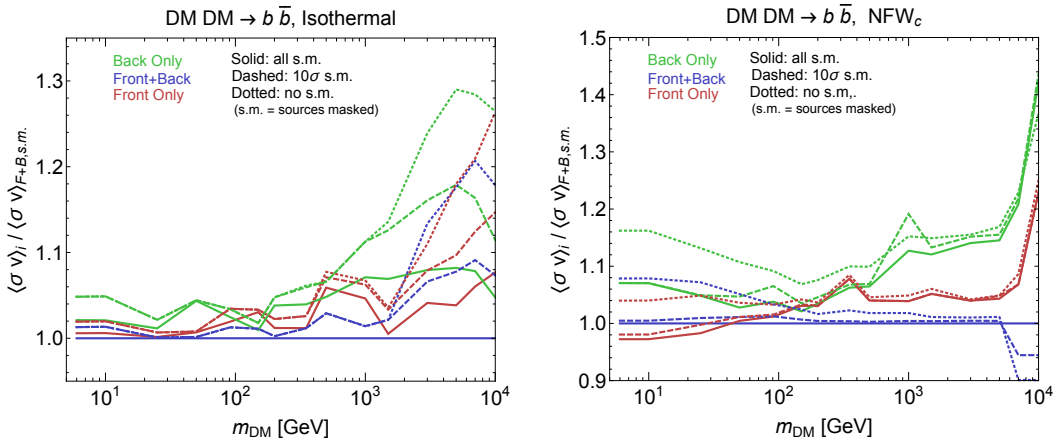

Figure 2.C.1: Ratio of expected cross section upper limits vs. DM mass from simulated MC data for DM annihilation to $b\bar{b}$ for isothermal (**left**) and NFW$_c$ (**right**) profiles. The denominator of the ratio, $\langle\sigma v\rangle_{\rm F+B,s.m.}$, is the cross section upper limit obtained when masking all known point sources in the 5-year *Fermi*-LAT point-source catalog, outside a $2^\circ \times 2^\circ$ square centered at the GC and including front- and back-converting events. The numerators of the ratios, $\langle\sigma v\rangle_i$, are the cross section upper limits obtained when masking all known point sources outside the $2^\circ \times 2^\circ$ GC square (solid lines), masking only those sources detected at more than 10σ (outside the same $2^\circ \times 2^\circ$ GC square) (dashed lines), and masking no sources (dotted lines). In each case we either include both front- and back-converting events (blue lines), only front-converting events (red lines), and only back-converting events (green lines).

$(0.0821, 0.166)$, and $\beta = (0.762, 0.750)$. No source masking is performed within the inner $2^\circ \times 2^\circ$ square at the GC, where the density of sources is very high and the expected DM signal peaks.

The effect on the cross-section upper limits versus DM mass, when masking known point sources, and when including front- and/or back-converting events, is shown in Fig. 2.C.1 on simulated data sets. The left (right) plot assumes DM annihilation to $b\bar{b}$ for our choice of an isothermal (NFW-contracted) density profile. We choose a shallow and cuspy profile to see how the results depend on having either large or small optimized ROIs, respectively. For each DM mass, and for each choice of source masking and inclusion of front-/back-converting events, we optimize the ROI choice and derive the average limit obtained from

the ten simulated MC data sets. In Fig. 2.C.1, we show a ratio of expected cross section upper limits versus DM mass: the denominator of the ratios, $\langle\sigma v\rangle_{\mathrm{F+B,\,s.m.}}$, is the cross section upper limit obtained when masking all known point sources as described above and including front- and back-converting events; the numerators of the ratios, $\langle\sigma v\rangle_i$, are the cross section upper limits obtained when masking all known point sources (outside the $2^\circ\times2^\circ$ GC square) (solid lines), masking only those sources detected at more than 10σ (outside the same $2^\circ \times 2^\circ$ GC square) (dashed lines), and masking no sources (dotted lines). In each case we either include both front- and back-converting events (blue lines), only front-converting events (red lines), or only back-converting events (green lines).

We see from Fig. 2.C.1 that, at least for the two annihilation models considered in this section, the expected limits are the same within $\mathcal{O}(10-30\%)$. Moreover, the strongest constraints are generically obtained when masking all point sources. For DM masses below $\sim$ 50 GeV and cuspy profiles, the inclusion of only front-converting events is expected to provide the strongest constraints, but only marginally so. Above $\sim$ 50 GeV, the inclusion of both front- and back-converting events is best, since the photons produced in the annihilation of DM have such high energies that the PSF effects are negligible, and the inclusion of as much data as possible leads to stronger expected limits.

Based on this, we conclude that the effect of source masking and choice of front-/back-converting events is not large on our results. We also note that the inclusion of both event-conversion types and the masking of point sources (blue solid line in Fig. 2.C.1) is expected to give constraints that are among the best. We thus make this our standard choice when showing the results in §2.4.

2.D Inverse Compton Scattering

In this appendix we discuss how the results from §2.4 depend on the parameters in the ICS computation performed in `GALPROP`. The amount of ICS radiation depends sensitively on various key propagation parameters whose

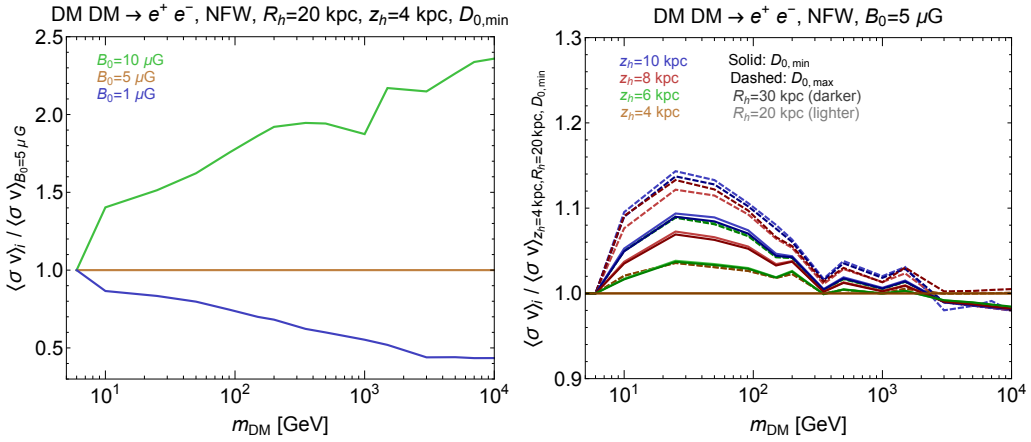

Figure 2.D.1: Ratios of cross-section upper limits from simulated data on DM annihilation to e^+e^- for an NFW profile, including prompt and ICS radiations, for different values of the Galactic magnetic field (**left**) and different combinations of other propagation model parameters (**right**). The magnetic field has the largest effect on our analysis.

values are not known to a satisfactory degree. Here we describe the effect on our constraints from varying these parameters in order to capture some of the systematic uncertainties associated with the DM-generated ICS signal.

We study how different models of propagation impact our results. We use, as a starting point, the *Fermi*-LAT results from [169], in which various propagation models are fit to cosmic-ray spectra for various choices of the region of containment of the cosmic rays (parametrized with a cylindrical geometry of half-height z_h and radius R_h). In our study, we vary z_h and R_h, and two other important parameters that have a big effect on the DM ICS signal, namely the Galactic magnetic field value in the Solar System, B_0, and the spatial diffusion coefficient D_0. The values used in our study are:

1. $z_h = 4, 6, 8, 10\,\mathrm{kpc}$

2. $R_h = 20, 30\,\mathrm{kpc}$

3. $D_0 = D_{0,\mathrm{min}}, D_{0,\mathrm{max}}$, where $D_{0,\mathrm{min}}$ and $D_{0,\mathrm{max}}$ are the minimum and maximum values of D_0 spanned by the various `GALPROP` models studied

in [169] for a given (z_h, R_h).

4. $B_0 = 1, 5, 10$ μG

As an illustration of the dependence of the DM ICS signal on these parameters, Fig. 2.D.1 shows the constraint on DM annihilation to e^+e^-, assuming an NFW$_c$ DM profile. The greatest effect on the uncertainty of the DM ICS signal originates from the variation in the magnitude of B_0, as clearly shown in the left plot. Varying the other parameters (right plot) has less of an effect on the DM ICS signal. We are therefore allowed, when showing the results in §2.4, to fix $z_h = 4\,\text{kpc}$ and $R_h = 20\,\text{kpc}$; whereas we show the variation of our results with B_0 and correspondingly $D_0 = D_{0,\text{min}} = 4.797 \times 10^{28}$ cm^2/s for $B_0 = 1$ μG (parameters yielding the strongest constraints) and $D_0 = D_{0,\text{max}} = 6.311 \times 10^{28}$ cm^2/s for $B_0 = 10$ μG (parameters yielding the weakest constraints).

2.E Details on the Simulated Data Sets

The optimization procedure described in §2.3.4 to find the optimal ROIs and energy ranges, $[\text{ROI}, \Delta E]_O$, is performed on ten simulated data sets, each a 5.84-year representation of the γ-ray sky. Here we provide a few more details on the simulations.

The generation of mock *Fermi*-LAT observations was carried out with the `gtobssim` routine, part of the Fermi Science Tools package v9r34p1. Its output is a list of MC-simulated γ-ray events with relative spatial direction, arrival time and energy, distributed according to an input source model and IRFs.

A number of model elements were put into `gtobssim` (see [170]). These include the *Fermi*-LAT Collaboration's model of the diffuse Galactic component,[3] the isotropic component (derived for Pass 7 Reprocessed Clean front and back IRFs),[4] and the 3FGL source catalog for point and small extended sources [157].

[3] `gll_iem_v05_rev1.fit`

[4] `iso_clean_front_v05.txt` and `iso_clean_back_v05.txt`

In addition, the full-sky simulations were calculated through `gtobssim` with the actual pointing and livetime history (FT2 file) of the *Fermi*-LAT for the first 5.84 years of the scientific phase of the mission. The source model simulated did not contain the Earth's Limb emission, which is negligible at energies above 1 GeV, compared to the celestial γ-ray signal, when a zenith angle $< 100^{\circ}$ cut is applied. The `gtobssim` tool convolves the flux components mentioned with the *Fermi*-LAT's response, i.e. PSF, energy dispersion, and effective area.

Ten instances of the MC gtobssim-generated data were run, each with an independent starting seed and the same source model; thus obtaining ten statistically independent instances of the γ-ray sky. The same event selection criteria were used for the MC data sets as for the real data. One important difference between the simulated data sets and the real data is the energy range. Each simulated data set was calculated in an energy range of 0.5 GeV to 500 GeV (as opposed to 1.5 GeV to 750 GeV for the actual data). The upper bound of 500 GeV in the `gtobssim` simulations is the upper limit in the energy map of the interstellar diffuse model [170]. To deal with this mismatch, we simply fit a power-law curve to each of the ten simulated data spectra for 6.2 GeV$< E <$ 460 GeV that we obtain for each ROI, and extrapolate it to 750 GeV. (The lower value of 6.2 GeV is low enough to have enough photons to perform a meaningful fit even for small ROIs, and high enough for a single featureless power law to provide a reasonable fit to the spectra. The upper value of 460 GeV is low enough to avoid count leakages due to finite energy resolution on the sharp 500 GeV input-energy cutoff.) We then populate each bin above 460 GeV with a random number of events chosen from a Poisson distribution whose expectation value equals the extrapolated value in a given bin. The subsequent optimal ROI and energy range for each theory hypothesis T_H is found using the original plus extrapolated spectra.

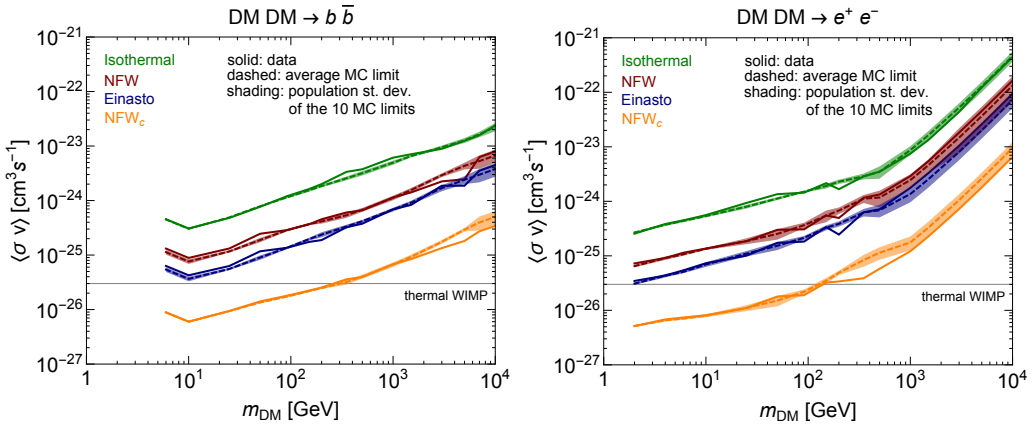

Figure 2.F.1: Comparison between average MC-based expected (dashed) and real-data (solid) 95% C.L. annihilation cross section upper limits on DM annihilating to $b\bar{b}$ (**left**) and e^+e^- (**right**) for the Isothermal (green), NFW (red), Einasto (blue), and NFW$_c$ (orange) DM density profiles (we only consider prompt photons). The population standard deviations of the limits from the 10 individual MC simulations are also shown as shadings around the dashed lines.

2.F Comparison of limits between simulated and real data

In this appendix we compare the results derived from the real data with those derived from simulated data. Since our simulated data is of course not a perfect representation of the real data, we do not expect that the limits derived on the real data will agree perfectly with the limits derived on simulated data.

Fig. 2.F.1 compares the simulated and observed limit on DM annihilation to $b\bar{b}$ (**left plot**) and e^+e^-, including only prompt photons, (**right plot**), for the four different DM density profiles introduced in §2.2.1. Since the simulated data used in this study consists of 10 statistically independent realizations of the γ-ray sky, we present the arithmetic mean of the 10 limits (dashed lines) and the standard deviation of the population (shaded bands), as well as the observed limits (solid lines). We see that the limits derived using real versus simulated data agree over a wide range of masses and profiles.

Chapter 3

Light Dark Matter Direct Detection with Scintillating Targets

3.1 Introduction

Dark matter (DM) with a mass in the MeV–GeV range is phenomenologically viable and has received increasing attention in recent years [68, 70, 139, 140, 147, 171–216]. An important probe for DM is with *direct detection* experiments, in which a DM particle in the Milky-Way halo interacts with some target material in a detector, producing an observable signal in the form of heat, phonons, electrons, or photons [55]. The traditional technique of searching for nuclear recoils loses sensitivity rapidly for DM masses below a few GeV, since the DM is unable to transfer enough of its energy to the nucleus, resulting in no observable signal above detector thresholds. However, DM scattering off electrons, whose mass is much less than a nucleus, can lead to observable signals for masses well below 1 GeV [68], opening up vast new regions of parameter space for experimental exploration.

DM-electron scattering in direct detection experiments has been investigated for noble liquid targets [68, 173] and was demonstrated explicitly to

have sensitivity down to DM masses of a few MeV and cross-sections of $\sim 10^{-37}$ cm^2 [173] using published XENON10 data [217]. Semiconductor targets like silicon (Si) and germanium (Ge) could probe potentially several orders of magnitude of unexplored DM parameter space for masses as low as a few hundred keV [68, 70, 171, 172]. The feasibility of the required detector technology to detect small ionization signals still needs to be demonstrated and may become available in the next few years, e.g. with SuperCDMS [218] and DAMIC [219]. In the future, 2D targets could probe a directional signal [177] or superconductors or superfluids could probe even lower masses [174–176].

In this chapter, we explore using a *scintillator* as the target material to search for dark matter with masses as low as a few hundred keV. One or more scintillation photons are emitted when an electron excited by a DM-electron scattering interaction relaxes to the ground state [68][1]. Scintillation photons with an energy of $\mathcal{O}$(few eV) could be detected by an array of transition edge sensors (TES) or microwave kinetic inductance detectors (MKIDs) operated at cryogenic temperatures, which surround a scintillating target of volume $\sim \mathcal{O}((\text{few cm})^3)$. The development of such a large array of photodetectors sensitive to single photons is an active area of research [221]. The target itself should be cooled to cryogenic temperatures to avoid excitations induced by thermal fluctuations and large thermal gradients between it and the detector array.

Several good scintillating materials exist. In this chapter, we focus on three crystals, sodium iodide (NaI), caesium iodide (CsI), and gallium arsenide (GaAs). Other materials will be mentioned briefly.

3.2 Scintillators: Advantages & Challenges

Several signals are possible when sub-GeV DM scatters off a bound electron in an atom or a crystal, exciting the electron to a higher energy level or an unbound state [68]. Depending on the target material, an experiment can either measure an ionization signal, which is obtained by manipulating the

[1]Note that [220] proposed the search of one or more photons from Weak-scale dark matter through atomic excitations.

electron with an electric field, or one or more scintillation photons, which are emitted as the electron relaxes back to its ground state. Until now, the latter approach has not been considered in detail.

Measuring the ionization signal has already constrained DM as light as a few MeV [173], using XENON10's two-phase xenon time projection chamber (TPC). Unfortunately, several possible detector-specific backgrounds exist, so one cannot currently claim that the observed one- and few-electron events are from DM [173, 217, 222]. Using semiconductors, CDMSlite [218] applied a bias voltage, forcing a conduction-band electron to traverse the material and generate enough Neganov-Luke phonons [223, 224] to be measured by phonon detectors. The CDMSlite setup with improved phonon detectors may in the future surpass xenon-based TPCs in their sensitivity to sub-GeV DM. However, while there may be fewer dark counts than for two-phase xenon TPCs, the presence of an electric field may create spontaneous electron-hole pairs that could mimic a DM signal. Therefore, more work is needed to establish the potential of the CDMSlite setup.

Sub-GeV DM searches are unlikely to be limited by traditional backgrounds like Compton scattering, cosmogenics, or neutrons. These backgrounds typically produce electron recoils at higher energies, and ≤ 1 event/kg/year is expected in SuperCDMS in the $\sim 1 - 50$ eV range [225]. Great care must be taken to limit the material's surface exposure and radioactive contaminants. Coherent nuclear scattering of solar neutrinos is similarly insignificant. Instead, the discussion above highlights that understanding and controlling detector dark counts will likely determine the sensitivity.

Instead of searching for an ionization signal, one could search for one or more scintillation photons. Scintillators possibly have two distinct advantages. First, the detection of such a low number of photons may turn out to be technologically easier than detecting a low number of electrons with the CDMSlite setup (or with the DAMIC setup [219]). Second, no electric field is required to detect the photons, which may lead to fewer dark counts.

A potential background for scintillators is phosphorescence induced from a previous interaction (afterglow). Our candidate targets scintillate on nano-

to-millisecond timescales, but some photons could arise from excited states whose lifetimes are much longer (phosphorescent) due to a "forbidden" radiative transition. The phosphorescent photons typically have a lower energy, so if the photodetector's energy resolution is too low, a narrow-band optical filter could be placed between scintillator and photodetector to remove phosphorescent photons.

3.2.1 Scintillation in Crystals

Scintillation is the process of promoting a material to an excited state and collecting photons from the de-excitation. In crystals the excited states are electronic. We will here consider the case of an insulator or semiconductor, materials characterized by a gap in energy between the fully occupied electron states and the empty ones above. The excitation process will typically have an electron in the valence or core band being up-scattered to the conduction band. The succession of different quantum states that the resulting e-h pair goes through before radiative recombination leads to a classification into several scintillation mechanisms [226]. Broadly speaking, scintillation may be intrinsic (or self-activated, when it is present regardless of the crystal's purity level), extrinsic (due to alterations to the crystal), or cross-luminescent (from the direct recombination of a deep core hole and a valence electron). The last step of the scintillation process might involve the decay of bound e-h pairs (exciton) or of atomic states of impurities (activators, see also Fig. 3.A.1). For luminescence photons to effectively escape the material, mechanisms are in place to avoid re-absorption (transparency).

Let us follow the different fates of a crystal excitation and give examples[2] of scintillators exhibiting them.

First of all, it should be noted that for highly doped materials the impurities are themselves non negligible excitation targets and so the scintillation can proceed directly from the decay of an impurity's atomic excitation (*e.g.* CeF_3 [227]). Most typically, though, it will be an electronic state in the valence or core bands to be excited into the conduction band. After this happens

[2]For a very extensive list of scintillators, see http://scintillator.lbl.gov/

the fastest process to take place is the production of further (secondary) e-h pairs, if allowed by the total energy of the primary excitation. This process is rather efficient and a very high fraction of the energy lost by the primary e-h pair will be ceded to the secondaries (an empirical model for this process can be found in [228]). After the e-h pairs cannot excite any more other pairs, thermalization happens. This is the process whereby the electron and the hole within the respective bands will lose energy through non radiative processes and reach the top (resp. bottom) of the bands. In the case of an electron being up-scattered from a core band, the crystal's band structure might be such that thermalization of the hole is impossible and therefore a high-energy recombination happens with emission of a scintillation photon. This process is called *cross-luminescence* and the archetypal case is BaF_2 [229].

After thermalization the e-h pair might or might not be spatially correlated. If it is, the effective coulomb interaction between electron and hole will cause them to form a bound state with a hydrogen-like discrete spectrum below a continuum (which will constitute the conduction band). This two-particle state is called an *exciton* and we defer its detailed discussion to section 3.F. Suffice here to say that, while a bound state, it can have a finite momentum and travel through the crystal as a Bloch wave (*free exciton*). This free-traveling state can directly decay radiatively and this goes under the name of *free-exciton luminescence*. For this effect to be visible, it is often required that the crystal is extremely pure and kept at cryogenic temperatures. TlBr is a good such scintillator [230]. However, most typically the exciton will travel to and be trapped into an activator center such as an impurity (*Wannier excitons* [231]), an ion complex (*Frenkel excitons* [232]), or a lattice defect (which can be induced by the carrier itself: *self-trapping* [233]). Here, two options are available: the exciton settles and decays radiatively (*bound-exciton luminescence*, Example: ZnO:Ga [234], $CdWO_4$ [235], ultra-pure NaI [236] respectively), or it is converted into an excited state of the impurity (quenching), which then decays radiatively.

If instead the electron and the hole are far away from each other (for example because of phonon scattering), then it might happen that either carrier

is trapped in the same ways that we have described for the excitons (possibly forming ionized versions of the impurity atoms). At this point the opposite carrier can be captured by this potential well and either the carrier once again form a bound exciton which decays radiatively (e.g. Example: NaI:Tl [237]) or recombination of the impurity ion occurs with ensuing luminescence.

As stated above, for luminescence to be effectively observable, the photons need to be able to exit the crystal with little re-absorption probability, and it is this reverse process that finally determines the brightness of a scintillator (that is how much of the energy transferred to the scintillator is returned in luminescence photons). Naturally, it is the presence of virtual states with the same energy of the photons that makes re-absorption possible. It is clear then that when the radiative decay involves activating centers (defects or impurity states), the energies of these transitions will be shifted w.r.t. those of the crystal's bulk and therefore only other activating centers will be able to re-absorb the photons. However, the spatial density of such centers is very low and therefore most photons escape the crystal. Another mechanism in place is the so-called *Stokes' shift* [238]. This is a thermal effect whereby the ground states of the excited and unexcited particles are shifted by a small amount in momentum and therefore the up-transition and the down-transition (when they happen radiatively, and thus with zero momentum transfer) have slightly different energies. It particularly helps in those cases, like with free-exciton luminescence, where the density of potentially re-absorbing states is very large (virtual free-exciton states are found everywhere throughout the crystal).

3.3 Schematic Experimental Concept

Fig. 3.1 shows the experimental concept: a scintillating target is surrounded by a detector-array sensitive to single photons. An active shield surrounds the detector to veto radioactive backgrounds, including gamma rays that Compton-scatter in the target material. An optical filter between the scintillator and the photodetector could ensure passage of only the expected photon wavelengths.

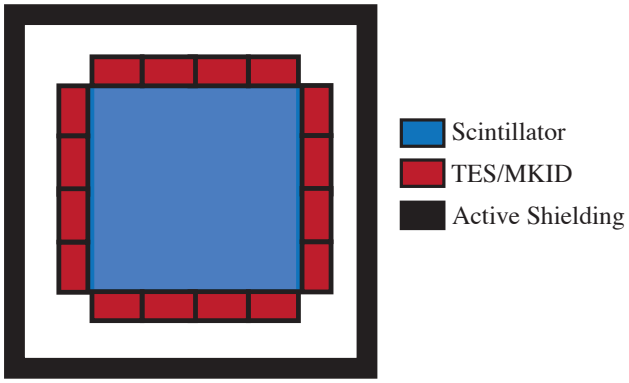

Figure 3.1: Schematic experimental concept: a DM particle scatters off an electron in a scintillating target, exciting it to a higher-energy level; one or more scintillation photons from the relaxation of the electron to the ground state are observed by a surrounding photodetector array. The detector is encased in an active shield to eliminate environmental backgrounds. No electric field is needed, reducing or eliminating many potential detector-specific backgrounds.

Detectors with single-photon sensitivity and no dark counts exist, e.g. MKIDs [239] and TESs [240], which operate at $\mathcal{O}(100$ mK) temperatures. These detectors can have few-percent energy resolution and microsecond time resolution [239]. MKIDs (TESs) have demonstrated single-photon sensitivity at photon energies of $\sim 0.25 - 12.4$ eV [239] ($\sim 0.04 - 3.1$ eV [241]), with the potential to be sensitive to meV phonon energies [175, 242]. Currently the most sensitive single-photon devices [175, 243–245] are small in size, $\sim((5 - 125)\ \mu\text{m})^3$, but efforts exist to enlarge them [221]. CRESST-II currently has the best detector of few-cm size, sensitive to $\mathcal{O}(10)$ photons, which uses a TES read out by SQUIDs [246, 247]. Silicon photomultipliers (SiPM) are possible photodetectors and operate well at cryogenic temperatures, but the dark-count rate may be too large [248, 249].

3.4 Distinguishing Signal from Backgrounds

A few handles exist to distinguish a DM signal from a background. First, the signal rate modulates annually and daily due to the motion of the Earth [250]. The modulation is larger than for elastic WIMP-nucleus recoils, since the scattering is inelastic [251], and increases with threshold. Backgrounds are not expected to have the same phase, amplitude, period, and energy dependence.

Second, the DM-induced electron-recoil spectrum is distinctive and unlikely to be mimicked by a background. Third, the DM signal scales with the target volume, in contrast to many potential backgrounds arising from the surrounding detector package. This can be confirmed by using the same detector but with a hollow crystal[3]. Backgrounds that scale with the target volume, such as external gammas and phosphorescence, can be determined by measuring the change in signal when a gamma ray source is placed outside the detector.

3.5 Dark Matter-Electron Scattering

To inform our choice of scintillating materials, we review here the scattering of sub-GeV DM off a bound electron in a crystal. The salient features emphasized below also apply to atoms. See [70] for details.

The rate for DM-electron scattering to excite an electron from level i to f is

$$\frac{\mathrm{d}R_{\mathrm{crystal}}}{\mathrm{d}\ln E_e} = \frac{\rho_\chi}{m_\chi}\, N_{\mathrm{cell}}\, \overline{\sigma}_e\, \alpha\, \frac{m_e^2}{\mu_{\chi e}^2}\, \times \int \mathrm{d}\ln q \left(\frac{E_e}{q}\eta\big(v_{\mathrm{min}}(q,E_e)\big)\right) F_{\mathrm{DM}}(q)^2 \left|f_{\mathrm{crystal}}(q,E_e)\right|^2, \tag{3.5.1}$$

where $\alpha \simeq 1/137$ is the fine-structure constant, m_χ (m_e) denotes the DM (electron) mass, $\rho_\chi \simeq 0.4$ GeV/cm^3 is the local DM density, E_e is the total energy deposited, q is the DM-to-electron momentum transfer, $N_{\mathrm{cell}} = M_{\mathrm{target}}/M_{\mathrm{cell}}$ is the number of unit cells in the target crystal of total (cell) mass M_{target} (M_{cell}), and $\mu_{\chi e}$ is the DM-electron reduced mass. The *crystal form-factor* is

$$\left|f_{\mathrm{crystal}}(q,E_e)\right|^2 = \frac{2\pi^2 V_{\mathrm{cell}}}{\alpha m_e^2} \sum_{i\,f} \int_{\mathrm{BZ}} \frac{\mathrm{d}^3k\ \mathrm{d}^3k'}{(2\pi)^6} \delta(E_e - \Delta E) \times \sum_{\vec{G}'} q\delta(q - |\vec{k}' - \vec{k} + \vec{G}'|) \left|f_{[i\vec{k}, f\vec{k}', \vec{G}']}\right|^2, \tag{3.5.2}$$

where $\Delta E = E_{f\vec{k}'} - E_{i\vec{k}}$, V_{cell} is the volume of the unit cell, $\vec{k}, \vec{k}'$ are wavevectors

[3]We acknowledge Matthew Pyle for insightful discussions.

in the first Brillouin Zone (BZ), and $\vec{G}'$ is the reciprocal lattice vector. The reference cross-section $\overline{\sigma}_e$ and DM form factor $|F_{\rm DM}(q)|^2$ are parameterizations of the DM-electron interaction defined as

$$\overline{|\mathcal{M}_{\rm free}(\vec{q})|^2} \equiv \overline{|\mathcal{M}_{\rm free}(\alpha m_e)|^2} \times |F_{\rm DM}(q)|^2 \tag{3.5.3}$$

$$\overline{\sigma}_e \equiv \frac{\mu_{\chi e}^2 \overline{|\mathcal{M}_{\rm free}(\alpha m_e)|^2}}{16\pi m_\chi^2 m_e^2}, \tag{3.5.4}$$

where $\overline{|\mathcal{M}_{\rm free}|^2}$ is the absolute value squared of the elastic DM-free-electron scattering matrix element, averaged over initial-, and summed over final-state particle spins. The DM-halo profile is

$$\eta(v_{min}) = \int {\rm d}^3 v_\chi \, g_\chi(\vec{v}_\chi) \frac{1}{v_\chi} \Theta(v_\chi - v_{\rm min}) \tag{3.5.5}$$

$$= \frac{1}{K} \int {\rm d}\Omega \, {\rm d}v_\chi \, v_\chi \, e^{-|\vec{v}_\chi - \vec{v}_{\rm E}|^2/v_0^2} \times \Theta(v_\chi - v_{\rm min}) \Theta(v_{\rm esc} - v_\chi) \,, \tag{3.5.6}$$

where in Eq. (3.5.5) we chose for $g_\chi(\vec{v}_\chi)$ the standard Maxwell-Boltzmann distribution with a sharp cutoff. We take $v_0 = 230$ km/s, the Earth velocity about the galactic center $\vec{v}_{\rm E} = 240$ km/s, and the DM escape velocity from the galaxy as $v_{\rm esc} = 600$ km/s. $K = 6.75 \times 10^{22} ({\rm cm/s})^3$ is the normalization factor. The minimum velocity required for scattering is

$$v_{\rm min}(q, E_e) = \frac{E_e}{q} + \frac{q}{2m_\chi} \,. \tag{3.5.7}$$

There are four salient features worth emphasizing for sub-GeV DM scattering off electrons:

- First, since the bound electron's momentum can be arbitrarily high (albeit with suppressed probability), q can be arbitrarily high, so that in principle all of the DM's kinetic energy can be transferred to the electron (in sub-GeV DM scattering off nuclei only a fraction is transferred to a much heavier nucleus). Thus, $E_\chi = \frac{1}{2} m_\chi v_\chi^2 \geq E_e$ implies

$m_\chi \gtrsim 250$ keV $\times (E_e/1$ eV) for $v_\chi \lesssim v_{\rm esc} + v_{\rm E}$. Therefore, smaller ionization energies or band gaps can probe lower DM masses, with crystal targets being sensitive down to a few hundred keV.

- Second, since the electron moves at a speed of $\sim \alpha$, much faster than the DM ($\sim 10^{-3}$), the electron determines the typical q, $q_{\rm typ}$. A rough estimate for $q_{\rm typ}$ is the crystal momentum, $2\pi/a \sim 2.3$ keV, where $a \sim 10\alpha m_e$ is the lattice constant for our target choices (see below). Since $E_e \sim \vec{q} \cdot \vec{v}_\chi$, the minimum q to obtain a particular E_e is given by $q \gtrsim q_{\rm typ} \times E_e/(2.3$ eV). A similar estimate holds for atoms [70]. The signal rate is thus larger in semiconductors with low band gaps ($\Delta E \sim 1-2$ eV) than insulators ($\Delta E \gtrsim 5$ eV) or noble liquids ($\Delta E \sim 12$, 16, 25 eV for xenon, argon, helium, respectively).

- Third, while the value of q is naturally $q_{\rm typ}$, q can in fact be much larger as mentioned above. This allows for much larger momentum transfers and recoil energies, although these are strongly suppressed.

- Fourth, since the scattering is inelastic, the annual modulation of the signal rate is larger than for typical WIMP elastic scattering [251].

3.6 Scintillating Targets

The previous discussion suggests using scintillating crystals with low band gaps. However, the crystals must also have high purity, high radiative efficiency (i.e. little non-radiative recombination of excited electron-hole pairs), and few native defects, all while being grown to large sizes ($\gtrsim 1$ kg). We thus focus on NaI and CsI, but include GaAs, which may also satisfy these criteria. Table 3.1 (*top*) lists salient features.

NaI and CsI are insulators that scintillate efficiently through the decay of self-trapped excitons. They are used extensively due to their high light output and ease of production [252–259]. Pure CsI is being considered for a DM-nucleus-recoil search [247]. Early measurements of GaAs, a direct-gap semiconductor, showed a radiative efficiency (internal) of ~ 0.6 at 77 K when

Material	E_g [eV]	Rad. Eff.	$E_{\rm em}^{\rm max}$ [eV]	τ [ns]	Mechanism
NaI [262]	5.9	0.95	4.1	300	SX
CsI [252, 263]	6.4	~ 1	4.0	10^3	SX
GaAs [260]	1.52	~ 0.6	~ 1.5	$10^{3(a)}$	BE

Material	E_g [eV]
Si	0.67
Ge	1.1

Table 3.1: Band gap (E_g), radiative efficiency, photon emission energy peak ($E_{\rm em}^{\rm max}$), radiative recombination time (τ), and scintillation mechanism (SX = self-trapped excitons, BE = bound excitons) for candidate scintillators. We focus on (*top table*): pure NaI, pure CsI, and GaAs (doped with acceptors or donors). Si and Ge (*bottom table*) are used for comparison, and suitable dopants could allow them to scintillate. $^{(a)}$Expected (no measurement).

doped with donors or acceptors [260]. Conventional coupling to photodetectors is inefficient due to the high refractive index (~ 3.8) but one could apply photonic coatings or deposit the photodetectors directly onto the surfaces of the GaAs crystal to reduce internal reflection [261].

In addition to GaAs, other suitable low band gap materials may exist. Crystals with band gaps $\lesssim$ few eV are likely semiconductors [264]. Among these, direct-gap semiconductors have a high radiative efficiency, but no obvious candidates exist besides GaAs. Indirect-gap semiconductors are more common, but their scintillation is slow and inefficient without doping. However, luminescence has been reported from Si [265, 266] and Ge [267] at cryogenic temperatures (Table 3.1, *bottom*). More research could reveal suitable dopants to achieve high radiative efficiency. We show results for Ge and Si below since they are potential scintillators and are also used in current experiments sensitive to an ionization signal (e.g. SuperCDMS, DAMIC).

Other scintillator targets are possible. The appendices will mention several, and review the scintillation mechanisms of the substances in Table 3.1.

	a (bohr)	V_{cell} (bohr^3)	N_{bands}	N_e	N_k
CsI	8.6868	655.51	80	$8_v + 8_{c,\text{Cs}}$	30×125
NaI	12.927	464.88	50	8_v	30×216
GaAs	10.8690	321.00	60	$8_v + 10_{c,\text{Ga}}$	30×216
Ge	10.8171	316.4269	66	$8_v + 20_c$	$1\times$ 243
Si	10.3305	275.6154	56	8_v	$1\times$ 243

Table 3.2: Computational parameters for various materials. Lattice constant (a), cell volume (V_{cell}), number of valence+conduction bands (N_{bands}), number of valence v and core c electrons (N_e), and number of runs with independent random k-point meshes times number of k-points in each mesh (N_k). Note that there are two atoms per unit cell.

3.7 Calculations

We calculate the DM-electron scattering rates in NaI, CsI, and GaAs using the `QEdark` module developed in [70]. We use PBE functionals [268], norm-conserving pseudopotentials [269], and adjust the band gaps to the values in Table 3.1 using a scissor correction [270, 271]. Table 3.2 lists the required calculation parameters. We include in the density functional theory (DFT) calculation all electrons with binding energies E_B as low as the $3d$-shell of Ga (binding energy $E_B \sim 32$ eV), the $5p$- and $5s$-shell electrons ($E_B \sim 13$ eV and ~ 23 eV, respectively) of Cs, and the $3d$-shell electrons of Ge as in [70, 172] (deeper electrons are irrelevant). The numerical uncertainty is estimated by choosing 30 random k-point meshes. The sensitivity lines for Ge and Si are from [70] (only one mesh is shown, but the uncertainty is small [70]).

Our calculations do not include exciton effects. In the appendices we argue that exciton effects are negligible for the low-gap materials GaAs, Ge, or Si, and may have an $\mathcal{O}(1)$ effect for NaI and CsI.

3.8 Results

Fig. 3.1 (*left*) shows the potential sensitivity to $\overline{\sigma}_e$ (Eq. (3.5.3)) for two different F_{DM} (Eq. (3.5.4)), various materials, two thresholds, and data taken over one year with 1 kg of material. We assume a radiative efficiency of 1. The low-gap materials GaAs, Si, and Ge can reach potentially DM masses as

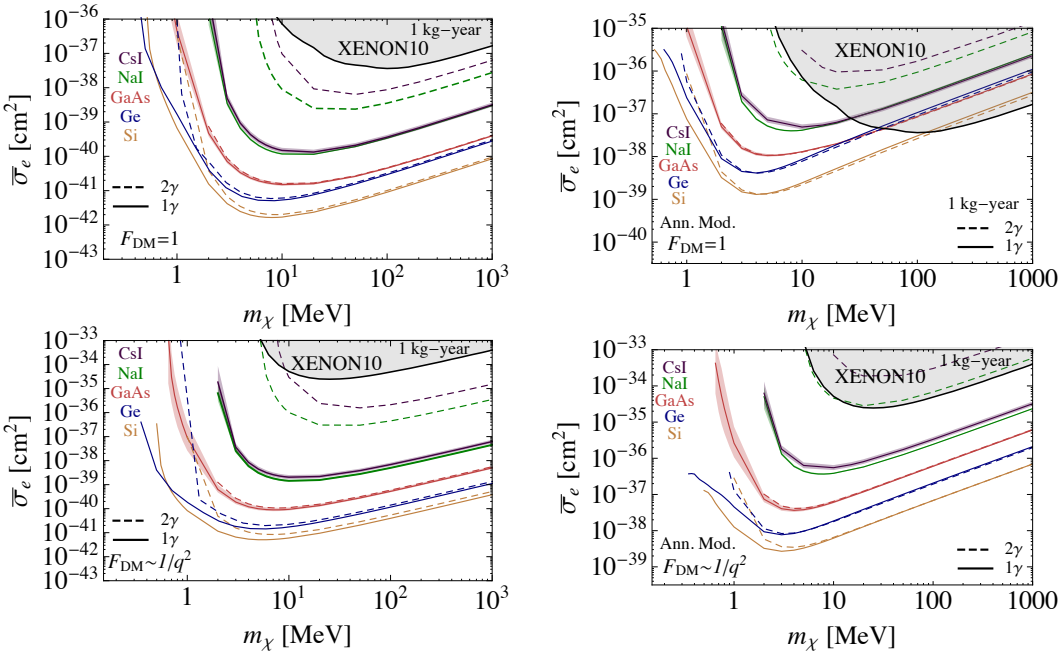

Figure 3.1: DM-electron-scattering-cross-section ($\overline{\sigma}_e$) reach vs. DM mass (m_χ) for $F_{DM}(q) = 1$ (*top*) and $F_{DM}(q) = 1/q^2$ (*bottom*), assuming an exposure of 1 kg for 1 year and a radiative efficiency of 1. *Left:* Solid (dashed) lines show 3.6 events for a threshold of one (two) photons, corresponding to the 95% c.l. reach for zero background events in CsI (purple), NaI (green), and GaAs (red). Bands around solid lines show the numerical uncertainty. Solid (dashed) lines for Ge (blue) and Si (gold) are the one(two)-electron threshold lines from [70]. *Right:* Solid (dashed) lines show 5σ-discovery reach using annual modulation for a threshold of one (two) photons, assuming zero backgrounds. The gray region is excluded by XENON10 [173].

low as a few hundred keV, whereas the reach of NaI and CsI is 1–2 MeV. This could probe lower masses than XENON10 [173], and extend the high-mass reach by one to several orders of magnitude.

The signal in GaAs, NaI, and CsI consists of one or more photons, while in Ge and Si it consists of either one or more electrons, or (if suitable dopants can provide a high radiative efficiency) one or more photons. We show two thresholds: "1γ" requires $E_e \geq E_g$, while "2γ" requires $E_e \geq E_g + \langle E \rangle$, where $\langle E \rangle$ is the mean energy needed for the recoiling electron to form another

electron-hole pair. A phenomenological approach gives $\langle E \rangle \sim 2.9$ eV (3.6 eV, 4.2 eV) for Ge (Si, GaAs) [70, 272, 273]. Precise values for CsI and NaI are unavailable, so we show $\langle E \rangle = 3E_g$ [273]. More theoretical work and an experimental calibration can better quantify the number of photons produced by low-energy electron recoils. The mass threshold is different for the 1γ and 2γ lines. However, the low-gap materials have a similar high-mass reach for either threshold, since E_e is typically several eV and more likely to produce two rather than one photon. Resolving two photons in coincidence can help reduce backgrounds.

The annual modulation of the signal rate can be used as a discriminant from background [250]. Fig. 3.1 (*right*) shows 5σ discovery lines for which $\Delta S/\sqrt{S_{tot} + B} = 5$ with $B = 0$. Here ΔS is the modulation amplitude and S_{tot} (B) is the total number of signal (background) events. The sensitivity weakens $\propto \sqrt{B}$, assuming B is constant in time.

To summarize, we described a novel search for sub-GeV DM, using scintillators. Scintillators provide a complementary path with potential advantages over other approaches searching for a low ionization signal: the detection of photons may be technologically easier with fewer dark counts.

Appendix

3.A Brief Review of Scintillation Mechanisms

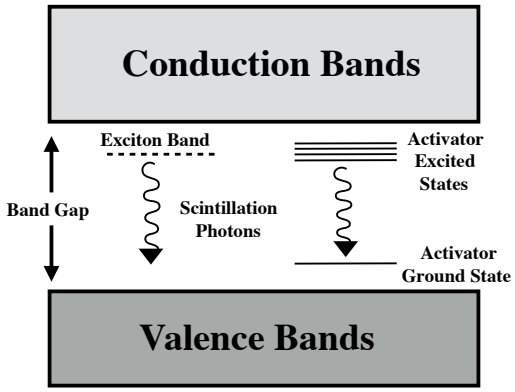

Figure 3.A.1: Illustration of the different mechanisms for light emission in a scintillating crystal.

We review briefly the scintillation mechanisms of the materials listed in Table 3.1 of this chapter. In general, for a material to be a scintillator, it must contain luminescent centers. These centers can be either extrinsic (e.g. dopants and impurities) or intrinsic (e.g. defects of the lattice or excitons), and give rise to a transition between a higher- and a lower-energy state. Moreover, the energy levels involved in the transition must be contained in a forbidden energy region (e.g. the band gap for semiconductors and insulators, or excimer states in gases) to avoid re-absorption of the emitted light or photoionization of the center (Fig. 3.A.1).

Pure CsI and NaI at cryogenic temperatures scintillate via the formation

of self-trapped excitons, where an exciton (an electron-hole bound state) becomes self-trapped by deforming the lattice structure around it. At cryogenic temperatures the system lies at the minimum energy in lattice configuration space, and the system can only return to the ground state by emission of a photon. At higher temperatures, thermally induced lattice vibrations allow the system to return to the ground state by phonon emission resulting in a low radiative efficiency. At room temperature, this thermal quenching is overcome by doping the material with e.g. thallium. In these cases, Tl^+ traps the excitons and provides an efficient luminescence center.

Direct-gap semiconductors, like GaAs, have the advantage that an excited electron can recombine with a hole without requiring a change in crystal momentum. In practice, however, dopants are used to enhance the radiative quantum efficiency, by providing radiative centers, and to reduce non-radiative recombination from impurities and native defects.

Indirect-gap semiconductors, like Si and Ge, require dopants to allow radiative recombination at cryogenic temperatures through the formation of a bound exciton that can radiate without the need for a change in crystal momentum.

Plastic scintillators consist of a base polymer that contains delocalized π-orbital electrons and a small concentration of fluorescent molecules. Excited π-orbital electrons will diffuse through the base polymer and excite fluorescent molecules. These excitations have radiative lifetimes of $1-2$ nanoseconds. This process is efficient both at room and cryogenic temperatures.

In tungstate scintillators, valence-band electrons on the oxygen ions can be excited to conduction band states on the tungsten ions. In $PbWO_4$, the excited state is thermally quenched so that at room temperature the luminosity is low and the decay time is short. $CaWO_4$ and $CdWO_4$ are more efficient at room temperature and their decay times are $\sim$10 microseconds.

3.B Effect of Excitons on Dark Matter-Electron Scattering-Rate calculations

Our calculation of the DM-electron scattering rate neglects the effect of *excitons*. In this section, we discuss why we expect this to be a good approximation for the low-band-gap materials (Ge, Si, and GaAs), but that there may be an $\mathcal{O}(1)$ correction for the large-band-gap insulators (NaI and CsI).

Semiconductors or insulating crystals are characterized by a finite band gap, E_g, between the top of the valence band and the bottom of the conduction band. These bands form an energy continuum for the excitation of an electron from the valence to the conduction band, which can be viewed as the creation of a free-electron-free-hole pair. In our calculation of the DM-electron scattering rate, we included the contribution of this continuum of states.

The small electrostatic Coulomb attraction between the negatively charged electron and positively charged hole creates an exciton, a bound electron-hole pair (see e.g. [274–277] and references therein). As we will see below, this Coulomb-bound electron-hole pair can be modeled with Rydberg-like states with energies $E_g - E_{B,n}$, where $E_{B,n}$ is the binding energy and n labels the Rydberg-like energy level. The energy of these excitons is therefore in the "forbidden" band-gap region, so that the density of states is nonzero even at energies slightly below the conduction band. Moreover, the bound electron-hole pair has ionized states with a continuous energy due to their relative motion. It turns out that excitons therefore also moderately increase the density of states just above the band gap compared to a calculation that neglects them. Including exciton effects in the DM-electron scattering-rate calculation could thus be important for two reasons. First, a nonzero density of states below the band gap means that the actual mass threshold is slightly lower. Second, any calculation that neglects exciton effects might underestimate slightly the scattering rate.

Excitons are extensively studied in solid state physics and play an important role in determining the properties of various materials. For example, it is well known that excitons are crucial in understanding the spectrum for

	ε	m_e^*/m_e	m_h^*/m_e	$\Delta E_{B,n=1}$ [eV]	$a_{n=1}/a$
CsI [278, 279]	5.65	0.312	2.270	0.117	2.37
NaI [279, 280]	7.28	0.287	2.397	0.066	2.20
GaAs [278, 281]	12.85	0.067	0.45	0.005	20.3
Ge [278, 281]	16	0.2	0.28	0.006	12.7
Si [278, 281]	13	0.33	0.49	0.016	6.38

Table 3.B.1: Dielectric constant (ε), effective electron mass (m_e^*), effective hole mass (m_h^*), 1s-exciton binding energy, and 1s-exciton radius (in units of the lattice constant a in Table 3.2) for various materials.

the absorption of light, as they allow for photons with an energy just below E_g to be absorbed by an electron. Similarly, excitons can play an essential role in determining the scintillation properties of a material. For example, an electron excited from the valence to the conduction band can quickly relax to the bottom of the conduction band and then into an exciton state by emitting phonons. The radiative decay of the exciton then yields a photon whose energy is just below that of the band gap. This typically allows the photon to traverse the material without being absorbed again, i.e. the material scintillates.

We can estimate how far below the conduction band the density of states will be nonzero from exciton effects by using a hydrogen-like model for the electron-hole pair. In particular, the exciton binding energies $E_{B,n}$ can be approximated by a modified Rydberg energy, namely

$$\Delta E_{B,n} = \frac{\alpha^2 \, \mu_{eh}}{2 \, \varepsilon^2 \, n^2} \ , \tag{3.B.8}$$

where ε is the dielectric constant of the crystal, $n = 1, 2, \ldots$, and μ_{eh} is the effective electron-hole reduced mass, given by

$$\mu_{eh}^* = \left(\frac{1}{m_e^*} + \frac{1}{m_h^*} \right)^{-1} \ , \tag{3.B.9}$$

where m_e^* (m_h^*) is the effective electron (hole) mass. In this approximation, the electron-hole pair is assumed to be subject to a screened Coulomb potential characterized by the dielectric constant ε. This is a good approximation only

if the exciton radius, a_n, is much larger than the lattice constant (*Wannier* exciton). The exciton radius is given by

$$a_n = \frac{\varepsilon m_e n^2}{\mu_{eh}} a_0 \,, \tag{3.B.10}$$

where a_0 is the (hydrogen) Bohr radius. The relevant values for the materials we considered in this chapter are given in Table 3.B.1, which also lists the binding energy and size of the various 1s exciton states (i.e. with $n = 1$).

The 1s-exciton radii listed in Table 3.B.1 for GaAs, Ge, and Si are much larger than the lattice constants given in Table 3.2, so that the approximation of the binding energies with Eq. (3.B.8) is expected to be reasonable. For NaI and CsI, the approximation is expected to be worse, but not dramatically so. We can thus use this simple estimate of the binding energies to reach at least qualitative conclusions for how the inclusion of exciton effects might affect the DM-mass threshold and the DM-electron scattering-rate calculation.

First, we see from Table 3.B.1 that the 1s-exciton binding energies for the low-band-gap materials, GaAs, Ge, and Si, are very small, ~ 10 meV, but even for the insulators, NaI and CsI, the binding energy only reaches about ~ 100 meV. This lowers the mass threshold by $\sim 1 - 30$ keV, depending on the material, an effect that is smaller than the numerical uncertainty of the rate calculation without excitons.

Second, recall that the electron's recoil energy after a DM scattering event is typically several eV. The typical recoil energy is thus larger than the band gap energy for semiconductors like GaAs, Ge, and Si. A moderate increase in the density of states from the inclusion of exciton effects 10 meV below the band gap, as well as just above it, is thus not expected to be important in the rate calculation. For the insulators NaI and CsI with band gaps around 6 eV, an increase in the density of states below and above the conduction band's bottom could be somewhat important, since the electron will largely prefer to scatter to those states rather than higher-energy ones.

The calculation of exciton effects in the DM-electron scattering requires a dedicated effort. One reason for this is that existing numerical codes usually

calculate exciton effects for photon absorption or emission. However, a photon being absorbed by an electron does not significantly change the momentum of the electron, so that the transition from valence to conduction band occurs at roughly the same k-point. Instead, DM scattering off an electron does transfer a sizeable momentum, comparable with the crystal momentum.

The above discussion shows that it would be desirable to include exciton effects for NaI and CsI in the future. Neglecting the exciton effects, as we have done in our calculations, gives an overall conservative estimate for the DM-electron scattering rates.

3.C Recoil Spectra for gallium arsenide, sodium iodide, and caesium iodide

Fig. 3.B.1 shows the electron recoil spectra from DM-electron scattering for GaAs, NaI, and CsI. as a function of total deposited energy E_e, for two DM masses and two choices for the DM form factor. We include also spectra for Ge and Si for comparison (see also [70]). As expected, the spectra extend to higher recoil energies for higher DM masses, and $F_{\rm DM} \propto 1/q^2$ spectra decrease faster than those for $F_{\rm DM} = 1$, since lower momentum transfers are preferred. Bump-like features in the spectra are explained by comparing the energy at which they occur with the energies of the available valence bands.

3.D Density of States and Band Structures

Fig. 3.B.2 shows our calculated band structure and density of states (DoS) for GaAs, NaI, and CsI. For completeness, we include slightly modified plots from [70] for Ge and Si. We show all valence electron levels included in our DM-electron-scattering-rate calculation as well as the bottom of the conduction band.

3.E Dark matter-electron scattering

If a DM particle scatters with an electron in a stationary bound state such as in an atom, it can excite the electron from an initial energy level 1 to an excited energy level 2 by transferring energy $\Delta E_{1\to 2}$ and momentum $\vec{q}$. The cross section for this process takes quite a different form from the free elastic scattering cross section.

3.E.1 Scattering rate derivation

If $\mathcal{M}_{\rm free}(\vec{q})$ is the matrix element for free elastic scattering of a DM particle and an electron, then we parametrize the underlying DM–electron coupling using the following definitions [68]:

$$\overline{|\mathcal{M}_{\rm free}(\vec{q})|^2} \equiv \overline{|\mathcal{M}_{\rm free}(\alpha m_e)|^2} \times |F_{\rm DM}(q)|^2 \tag{3.E.11}$$

$$\overline{\sigma}_e \equiv \frac{\mu_{\chi e}^2 \overline{|\mathcal{M}_{\rm free}(\alpha m_e)|^2}}{16\pi m_\chi^2 m_e^2}\,, \tag{3.E.12}$$

where $\overline{|\mathcal{M}|^2}$ is the absolute square of $\mathcal{M}$, *averaged over initial and summed over final particle spins*. The *DM form factor* $F_{\rm DM}(q)$ gives the momentum-transfer dependence of the interaction – for example $F_{\rm DM} = 1$ for exchange of a heavy vector mediator or magnetic dipole moment interaction, $F_{\rm DM} = (\alpha m_e/q)$ for an electric dipole moment interaction, and $F_{\rm DM} = (\alpha m_e/q)^2$ for exchange of a massless or ultra-light vector mediator. $\overline{\sigma}_e$ parameterizes the strength of the interaction, and in the case of $F_{\rm DM} = 1$ is simply equal to the cross section for free elastic scattering. All sensitivity estimates or constraints on LDM will be given for $\overline{\sigma}_e$, which therefore plays the analogous role to $\sigma_{\chi N}$, the DM-nucleon scattering cross section, in (WIMP) DM scattering with nuclei.

With these definitions, the cross section for a DM particle to excite an electron from level 1 to level 2 can be written as

$$\sigma v_{1\to 2} = \frac{\overline{\sigma}_e}{\mu_{\chi e}^2} \int \frac{{\rm d}^3 q}{4\pi}\, \delta\Big(\Delta E_{1\to 2} + \frac{q^2}{2m_\chi} - \vec{q}\cdot\vec{v}\Big) \times |F_{\rm DM}(q)|^2 |f_{1\to 2}(\vec{q})|^2\,, \tag{3.E.13}$$

where $f_{1\to2}(\vec{q})$ is the *atomic form factor* for the excitation. It is given by

$$f_{1\to2}(\vec{q}) = \int \mathrm{d}^3x\, \psi_2^*(\vec{x})\psi_1(\vec{x})e^{i\vec{q}\cdot\vec{x}}\,, \tag{3.E.14}$$

where ψ_1 and ψ_2 are the normalized wave functions of the initial and final electron levels.

The rate of excitation events, for a given transition and a given target electron, is found by multiplying the cross section by the DM number density and averaging over the DM velocity distribution. Here we approximate the velocity distribution as being a spherically symmetric function $g_\chi(v)$.

This allows the excitation rate to be written as

$$R_{1\to2} = n_\chi \frac{\overline{\sigma}_e}{8\pi\mu_{\chi e}^2} \int \mathrm{d}^3q\, \frac{1}{q}\eta\big(v_{\min}(q,\Delta E_{1\to2})\big)|F_{\mathrm{DM}}(q)|^2|f_{1\to2}(\vec{q})|^2\,, \tag{3.E.15}$$

where $n_\chi = \rho_{\mathrm{DM}}/m_\chi$ is the local number density of DM particles. The function $\eta(v_{\min})$ encodes all the necessary information about the DM velocity profile, and has its standard definition

$$\eta(v_{\min}) = \int \frac{\mathrm{d}^3v}{v}\, g_\chi(v)\,\theta(v - v_{\min})\,. \tag{3.E.16}$$

The function $v_{\min}(q,\Delta E)$ captures the requirement of energy conservation, and is given by

$$v_{\min}(q,\Delta E_{1\to2}) = \frac{\Delta E_{1\to2}}{q} + \frac{q}{2m_\chi}\,. \tag{3.E.17}$$

3.E.2 Form-factors

The solid state physics lives within the atomic form factor $f_{1\to2}(\vec{q})$ as defined in Eq. 3.E.14, which depends on the wavefunctions of the initial and final states. In the case of a crystal, the initial state is an electron residing in a valence band while the final state is an electron residing in a conduction band. The wavefunctions for both of these electrons can be written in Bloch form,

$$\psi_{i\vec{k}}(\vec{x}) = \frac{1}{\sqrt{V}} \sum_{\vec{G}} u_i(\vec{k}+\vec{G}) e^{i(\vec{k}+\vec{G})\cdot\vec{x}}\,, \tag{3.E.18}$$

where the $\vec{G}$'s are the reciprocal lattice vectors. Here V is the volume of the crystal, and the wave functions are taken to be unit-normalized, so that

$$\sum_{\vec{G}} \left|u_i(\vec{k}+\vec{G})\right|^2 = 1\,. \tag{3.E.19}$$

We can then write the *crystal form factor* as

$$f^{\text{crystal}}_{[i\vec{k},i'\vec{k}',\vec{G}']} = \sum_{\vec{G}} u^*_{i'}(\vec{k}'+\vec{G}+\vec{G}') u_i(\vec{k}+\vec{G})\,. \tag{3.E.20}$$

With this definition, the *total event rate* of excitation in a crystal is given by

$$\begin{aligned} R_{\text{crystal}} = n_\chi \frac{2\pi^2 \overline{\sigma}_e}{\mu^2_{\chi e}} V \sum_{i\,i'} \int_{\text{BZ}} \frac{\mathrm{d}^3k\,\mathrm{d}^3k'}{(2\pi)^6} \sum_{\substack{\vec{G}' \\ \vec{q}=\vec{k}'-\vec{k}+\vec{G}'}} \frac{1}{q} \eta\big(v_{\min}(q, E_{i'\vec{k}'} - E_{i\vec{k}})\big) \times \\ \times F_{\text{DM}}(q)^2 \left|f^{\text{crystal}}_{[i\vec{k},i'\vec{k}',\vec{G}']}\right|^2 . \end{aligned} \tag{3.E.21}$$

Here i is summed over the filled valence bands, and i' over the unfilled conduction bands, and the k-integrals are done over the first BZ. As indicated, in the sum over reciprocal lattice vectors $\vec{G}'$, q is to be replaced by $|\vec{k}'-\vec{k}+\vec{G}'|$. Note that this is the rate of events in the entire crystal, and so it is appropriate that it is proportional to the volume V of the whole crystal (this in turn is proportional to the number of targets, i.e. the total number electrons in the valence band throughout the crystal).

3.F Excitons Revisited

As we saw in Sec. 3.2.1, scintillation in crystals very often relies on the radiative decay of e-h states called *excitons*. An exciton (see [282]) is a configuration of an excited electron in a crystal correlated to its leftover hole via the

Coulomb interaction. Understanding the properties of such states, therefore, is crucial to controlling the properties of the luminescence of each specific material. Important scintillation parameters for our experimental set-up would be decay time, photon yield, and luminescence wavelength; all of which directly depend on the features of the exciton states. However, we did not need to worry about these theoretical considerations in chapter 3, because all the important performance parameters for the scintillators used can be estimated on a purely experimental basis and as such folded into our computations. Nevertheless, since excitons are states with energies slightly smaller than the band-gap, they might play a role in the initial DM-induced up-scattering process.

Is it possible that they constitute a final state for this scattering with a sizeable total rate? How would we go about calculating their contribution?

To answer these questions, in this appendix we delve deeper into the theory of excitonic states and develop formulae to account for their presence.

First we need to point out that, although it is common to say that excitons are additional states which live inside the band gap, this is incorrect. The exciton picture is a refinement of the band picture; it employs two-particle states as opposed to one-particle states, and entirely replaces the band description. How this picture can accommodate both discrete states and a continuum is described in Sec. 3.F.1 and is similar to how a hydrogen atom has a discrete and continuum spectrum at one time.

To fix some notation, we can write the wave function for an exciton as a linear combination of all possible products of 1-particle states for the electron and hole in the following fashion:

$$\Psi^S(\vec{r}_e, \vec{r}_h) = \sum_{\vec{k}_e, \vec{k}_h, i', i} A^S_{\vec{k}_e, \vec{k}_h, i', i} \psi_{i', \vec{k}_e}(\vec{r}_e) \psi_{i, \vec{k}_h}(\vec{r}_h), \tag{3.F.22}$$

where $\psi_{i', \vec{k}_e}(\vec{r}_e)$ is the 1-particle wave function of an electron with momentum k_e in the conduction band labeled by i'. S is a collection of quantum numbers differentiating all the excitonic eigen-states and $A^S_{\vec{k}_e, \vec{k}_h, i', i}$ are the coefficients of such linear combination. This wave function will solve the Schrödinger equa-

tion where we add to the Hamiltonian an attractive Coulomb term between electron and hole. (This term really accounts for the repulsion between the considered electron and all the others.) The lattice is perfectly periodic in the eyes of the exciton state (but it is not so any more for the single electron or single hole), so, since the exciton's momentum $\vec{q}$ is a good quantum number, we can write

$$\Psi^S_{\vec{q}}(\vec{r}_e, \vec{r}_h) = \sum_{\vec{k},i',i} A^S_{\vec{k}+\vec{q},\vec{k},i',i} \psi_{i',\vec{k}+\vec{q}}(\vec{r}_e)\psi_{i,\vec{k}}(\vec{r}_h). \tag{3.F.23}$$

3.F.1 Cardona's simplified model

For concreteness and illustration, we will now present a simplified model wich exhibits the fundamental properties of excitons. Following a discussion in [282], as a first approximation, we will consider exciton effects at M_0 critical points and assume that the conduction band is spherical with energy. We will address the problem as a perturbation around a solution with a single electron in a specific band i' and a single hole in a single band i. We write the exciton wave function Ψ, relative to a hole at the top of the valence band and an electron at the bottom of the conduction band, as a linear combination of the Bloch wave functions for the electron, $\psi_{\vec{k}_e}(\vec{r}_e)$, and hole, $\psi_{\vec{k}_h}(\vec{r}_h)$ in those bands

$$\Psi(\vec{r}_e, \vec{r}_h) = \sum_{\vec{k}_e,\vec{k}_h} A_{\vec{k}_e,\vec{k}_h} \psi_{\vec{k}_e}(\vec{r}_e)\psi_{\vec{k}_h}(\vec{r}_h). \tag{3.F.24}$$

Since the electron and hole are localized relative to their center of mass, we can write the wave functions in terms of Wannier functions $a_{\vec{R}_e}(\vec{r}_e), a_{\vec{R}_h}(\vec{r}_h)$ for the electron and hole, respectively. The resulting exciton wave function is then

$$\Psi(\vec{r}_e, \vec{r}_h) = N^{-1/2} \sum_{\vec{R}_e,\vec{R}_h} \Phi(\vec{R}_e, \vec{R}_h) a_{\vec{R}_e}(\vec{r}_e) a_{\vec{R}_h}(\vec{r}_h) \tag{3.F.25}$$

where $\Phi(\vec{R}_e, \vec{R}_h)$ is the exciton envelope wave function. Treating these variables as continuous, the wave equation is then

$$\left[-\left(\frac{\hbar^2}{2m_e}\right)\nabla^2_{\vec{R}_e} - \left(\frac{\hbar^2}{2m_h}\right)\nabla^2_{\vec{R}_h} - \frac{e^2}{4\pi\epsilon^2|\vec{R}_e-\vec{R}_h|}\right]\Phi(\vec{R}_e,\vec{R}_h) = E\Phi(\vec{R}_e,\vec{R}_h) \tag{3.F.26}$$

We can make a change of coordinates from $\vec{R}_e, \vec{R}_h$ to center of mass coordinate $\vec{R}$ and relative coordinate $\vec{r}$ defined by

$$\vec{R} = \frac{m_e\vec{R}_e + m_h\vec{R}_h}{m_e + m_h} \text{ and } \vec{r} = \vec{R}_e - \vec{R}_h. \tag{3.F.27}$$

Since the Coulomb interaction term we consider does not involve $\vec{R}$, we can now decouple the equation of motion for the center of mass from that of the relative motion, which gives rise to the following system of equations

$$\left(\frac{-\hbar^2}{2M}\right)\nabla^2_{\vec{R}}\psi(\vec{R}) = E_R\psi(\vec{R}) \tag{3.F.28}$$

$$\left(\frac{-\hbar^2}{2\mu}\nabla^2_{\vec{r}} - \frac{e^2}{4\pi\epsilon_0^2\vec{r}}\right)\phi(\vec{r}) = E_r\phi(\vec{r}) \tag{3.F.29}$$

where μ is the reduced mass of the exciton, defined by

$$\frac{1}{\mu} = \frac{1}{m_e} + \frac{1}{m_h}. \tag{3.F.30}$$

The solutions to Eqs. 3.F.29 are given by

$$\psi_{\vec{K}}(\vec{R}) = (N)^{-1/2}\exp(i\vec{K}\cdot\vec{R}) \text{ and } E_R = \frac{\hbar^2K^2}{2M} \tag{3.F.31}$$

$$\phi_{nlm}(\vec{r}) = R_{nl}(r)Y_{lm}(\theta,\phi) \text{ and } E_r = E_r(\infty) - \frac{R^*}{n^2} \tag{3.F.32}$$

where $E_r(\infty)$ is the energy gap and R^* is the Rydberg constant for the exciton defined as

$$R^* = \left(\frac{\mu}{m\epsilon_0^2}\right) \times 13.6 \text{ eV}. \tag{3.F.33}$$

We can then write the exciton envelope wave function

$$\Psi^{nlm}_{\vec{K}}(\vec{R},\vec{r}) = \left(1/\sqrt{N}\right)\exp(i\vec{K}\cdot\vec{R})R_{nl}(r)Y_{lm}(\theta,\phi) \tag{3.F.34}$$

$$E_{nlm} = E_g + \frac{\hbar^2K^2}{2M} - \frac{R^*}{n^2}. \tag{3.F.35}$$

If we want our coefficients in momentum-space like in Eq. 3.F.24 (we will see in the next section that this is desirable), we will have to Fourier-transform them as follows:

$$A_{\vec{k}_e,\vec{k}_h} = \sum_{\vec{R}_e,\vec{R}_h}\Phi(\vec{R}_e,\vec{R}_h)\exp\left(-i\vec{k}_e\cdot\vec{R}_e + i\vec{k}_h\cdot\vec{R}_h\right) \tag{3.F.36}$$

Now, the same procedure can be reiterated for all possible interband transitions to get

$$\Psi^{nlm}_{ii'\vec{K}}(\vec{R},\vec{r}) = \left(1/\sqrt{N}\right)\exp(i\vec{K}\cdot\vec{R})R_{nl}(r)Y_{lm}(\theta,\phi) \tag{3.F.37}$$

$$E^{ii'}_{nlm} = \Delta E_{i\to i'} + \frac{\hbar^2K^2}{2M_{ii'}} - \frac{R^*_{ii'}}{n^2}. \tag{3.F.38}$$

which shows the discrete part of the exciton spectrum. The continuum can be derived considering unbound solution to the wave equation.

3.F.2 Exciton transitions

Finally, the aim of this section is to compute the rate for a dark matter particle exciting the crystal's ground state into a free exciton. In Sec. 3.2.1 we saw bound excitons as well, however these states are localized around specific impurities or defects and therefore have a very low spatial phase-space density, which makes them extremely unlikely final states, and can be safely neglected. Let us switch notation from Eq. 3.F.23 and indicate the exciton state of momentum $\vec{k}$ and remaining quantum numbers S by the following ket:

$$|\left\{S,\vec{k}\right\}\rangle = \sum_{i',i,\vec{k}_e} A^S_{i',\vec{k}_e+\vec{k},i,\vec{k}_e}\,|\left\{i',\vec{k}_e+\vec{k},i,\vec{k}_e\right\}\rangle \tag{3.F.39}$$

where again the coefficients $A^{S}_{i',\vec{k}_e+\vec{k},i,\vec{k}_e}$ are such that $|\left\{S,\vec{k}\right\}\rangle$ diagonalizes the *electron-hole* interaction hamiltonian. Now, to compute the transition amplitude, let us look at the following average excitation rate in a dark matter halo for transitions to the familiar one-particle excited states first and we will then transition to the exciton case. We will follow closely the derivation in [70]. In general the rate is given by

$$R_{1\to 2} \;=\; n_\chi \int \mathrm{d}^3 v \, g_\chi\left(\vec{v}\right)\left(\sigma v\right)_{1\to 2} \tag{3.F.40}$$

where

$$\begin{aligned}\left(\sigma v\right)^{\text{free}}_{1\to 2} = \frac{1}{4E_\chi E_e}\int \frac{\mathrm{d}^3 q}{\left(2\pi\right)^3}\frac{\mathrm{d}^3 k'_e}{\left(2\pi\right)^3}\frac{1}{4E'_\chi E'_e}\left(2\pi\right)^4\delta\left(E'-E\right)\times \\ \times\delta^{(3)}\left(\vec{k}'_e-\vec{k}_e-\vec{q}\right)\left|\mathcal{M}_{\text{free}}\left(\vec{q}\right)\right|^2\end{aligned} \tag{3.F.41}$$

To understand how to modify the above free cross section to take bound states into account, let us compute the following free and bound expectation values and compare them.

$$\langle\vec{p}_\chi-\vec{q},\vec{k}'_e|T|\vec{p}_\chi,\vec{k}_e\rangle \;=\; \left(2\pi\right)^3\delta^{(3)}\left(\vec{k}'_e-\vec{k}_e-\vec{q}\right)\mathcal{M}_{\text{free}}\left(\vec{q}\right) \tag{3.F.42}$$

whence

$$\begin{aligned}\left|\langle\vec{p}_\chi-\vec{q},\vec{k}'_e|T|\vec{p}_\chi,\vec{k}_e\rangle\right|^2 = V\left(2\pi\right)^3\delta^{(3)}\left(\vec{k}'_e-\vec{k}_e-\vec{q}\right)\times \\ \times\left|\mathcal{M}_{\text{free}}\left(\vec{q}\right)\right|^2\end{aligned} \tag{3.F.43}$$

Here we have been denoting with $|\vec{p},\vec{k}\rangle$ the free plane-wave momentum eigenstates for dark matter ($\vec{p}$) and electron ($\vec{k}$), normalized such that $\langle\vec{p},\vec{k}|\vec{p},\vec{k}\rangle =$

$(2\pi)^3\delta^{(3)}(\vec{0}) = V$. In the bound case:

$$\langle \vec{p}_\chi - \vec{q}, \left\{ i', \vec{k}'_e, i, \vec{k}_e \right\} | iT | \vec{p}_\chi, 0 \rangle = \tag{3.F.44}$$

$$= \sum_{\vec{G}', \vec{G}} u^*_{i'} \left(\vec{k}'_e + \vec{G}' \right) u_i \left(\vec{k}_e + \vec{G} \right) \langle \vec{p}_\chi - \vec{q}, \vec{k}'_e + \vec{G}' | iT | \vec{p}_\chi, \vec{k}_e + \vec{G} \rangle = \tag{3.F.45}$$

$$= \sum_{\vec{G}', \vec{G}} u^*_{i'} \left(\vec{k}'_e + \vec{G}' + \vec{G} \right) u_i \left(\vec{k}_e + \vec{G} \right) (2\pi)^3 \delta^{(3)} \left(\vec{k}'_e - \vec{k}_e - \vec{q} + \vec{G}' \right) \mathcal{M}_{\text{free}}(\vec{q}) = \tag{3.F.46}$$

$$= \sum_{\vec{G}'} (2\pi)^3 \delta^{(3)} \left(\vec{k}'_e - \vec{k}_e - \vec{q} + \vec{G}' \right) f_{\left[i\vec{k}_e, i'\vec{k}'_e, \vec{G}' \right]} \mathcal{M}_{\text{free}}(\vec{q}) \Rightarrow \tag{3.F.47}$$

$$\left| \langle \vec{p}_\chi - \vec{q}, \left\{ i', \vec{k}'_e, i, \vec{k}_e \right\} | iT | \vec{p}_\chi, 0 \rangle \right|^2 = \tag{3.F.48}$$

$$= V \sum_{\vec{G}'} (2\pi)^3 \delta^{(3)} \left(\vec{k}'_e - \vec{k}_e - \vec{q} + \vec{G}' \right) \left| f_{\left[i\vec{k}_e, i'\vec{k}'_e, \vec{G}' \right]} \right|^2 |\mathcal{M}_{\text{free}}(\vec{q})|^2$$

So, comparing (3.F.43) and (3.F.48), I operate the following replacement in (3.F.41)

$$\delta^{(3)} \left(\vec{k}'_e - \vec{k}_e - \vec{q} \right) |\mathcal{M}_{\text{free}}(\vec{q})|^2 \to \sum_{\vec{G}'} \delta^{(3)} \left(\vec{k}'_e - \vec{k}_e - \vec{q} + \vec{G}' \right) \times \\ \times \left| f_{\left[i\vec{k}_e, i'\vec{k}'_e, \vec{G}' \right]} \right|^2 |\mathcal{M}_{\text{free}}(\vec{q})|^2 \tag{3.F.49}$$

and I get

$$(\sigma v)^{\text{bound}}_{1\to 2} = \frac{1}{4E_\chi E_e} \int \frac{\mathrm{d}^3 q}{(2\pi)^3} \frac{\mathrm{d}^3 k'_e}{(2\pi)^3} \frac{(2\pi)^4}{4E'_\chi E'_e} \delta(E' - E) \sum_{\vec{G}'} \delta^{(3)} \left(\vec{k}'_e - \vec{k}_e - \vec{q} + \vec{G}' \right) \times \\ \times \left| f_{\left[i\vec{k}_e, i'\vec{k}'_e, \vec{G}' \right]} \right|^2 |\mathcal{M}_{\text{free}}(\vec{q})|^2 \tag{3.F.50}$$

Now, the final electron momentum is fixed, so we have $\int \frac{\mathrm{d}^3 k'_e}{(2\pi)^3} \to \frac{1}{V}$, then I use the delta function to get rid of the $\int \mathrm{d}^3 q$ integral:

$$(\sigma v)^{\text{bound}}_{1\to 2} = \frac{1}{4E_\chi E_e} \frac{1}{V} \sum_{\vec{G}'} \frac{1}{4E'_\chi E'_e} (2\pi) \delta(E' - E) \left| f_{\left[i\vec{k}_e, i'\vec{k}'_e, \vec{G}' \right]} \right|^2 |\mathcal{M}_{\text{free}}(\vec{q})|^2 \Big|_{\vec{q} = \vec{k}'_e - \vec{k}_e + \vec{G}'} \tag{3.F.51}$$

In the non relativistic regime

$$\begin{aligned} E &= E_\chi + E_e = m_\chi + \frac{1}{2} m_\chi v^2 + m_e + E_{fermi} \approx m_\chi + m_e && \text{(3.F.52)} \\ E' &= E'_\chi + E'_e = m_\chi + \frac{\left(m_\chi \vec{v} - \vec{q}\right)^2}{2m_\chi} + m_e + E_{fermi} + \Delta E_{\left[i\vec{k}_e, i'\vec{k}'_e\right]} \\ &\approx m_\chi + m_e && \text{(3.F.53)} \\ E' - E &= \frac{q^2}{2m_\chi} - \vec{v}\cdot\vec{q} + \Delta E_{\left[i\vec{k}_e, i'\vec{k}'_e\right]} && \text{(3.F.54)} \end{aligned}$$

Now, some useful definitions. As we did in Sec. 3.E.1, we will use a reference amplitude computed at the typical atomic electron momentum $p_e \simeq \alpha m_e$ (because the kinematics of the process gives $q \sim p_e$) and, correspondingly, a reference cross section, like so (we will also assume that the amplitude only depends on the absolute value of the momentum transfer):

$$\begin{aligned} \left|\mathcal{M}_{\text{free}}(q)\right|^2 &\equiv \left|\mathcal{M}_{\text{free}}(\alpha m_e)\right|^2 \left|F_{\text{DM}}(q)\right|^2 && \text{(3.F.55)} \\ \bar{\sigma}_e &\equiv \frac{\mu_{\chi e}^2 \left|\mathcal{M}_{\text{free}}(\alpha m_e)\right|^2}{16\pi m_\chi^2 m_e^2} && \text{(3.F.56)} \end{aligned}$$

Hence,

$$(\sigma v)_{1\to 2}^{\text{bound}} = \frac{2\pi^2 \bar{\sigma}_e}{V \mu_{\chi e}^2} \sum_{\vec{G}'} \delta\left(\frac{q^2}{2m_\chi} - \vec{v}\cdot\vec{q} + \Delta E_{\left[i\vec{k}_e, i'\vec{k}'_e\right]}\right) \left| f_{\left[i\vec{k}_e, i'\vec{k}'_e, \vec{G}'\right]} \right|^2 \left|F_{\text{DM}}(q)\right|^2 \Big|_{\vec{q}=\vec{k}'_e - \vec{k}_e + \vec{G}'} \quad \text{(3.F.57)}$$

Now, plug this into (3.F.40) and get (where we choose the z_v axis along $\vec{q}$ and assume $g_\chi(\vec{v}) \equiv g_\chi(v)$)

$$R_{1\to 2} = \frac{2\pi^2 n_\chi \bar{\sigma}_e}{V \mu_{\chi e}^2} \sum_{\vec{G}'} \left| f_{\left[i\vec{k}_e, i'\vec{k}'_e, \vec{G}'\right]} \right|^2 |F_{\rm DM}(q)|^2 \times \tag{3.F.58}$$

$$\times \int v^2 \mathrm{d}v \, \mathrm{d}(\cos\theta_v) \, \mathrm{d}\phi_v \, g_\chi(v) \, \delta\left(\frac{q^2}{2m_\chi} - vq\cos\theta_v + \Delta E_{\left[i\vec{k}_e, i'\vec{k}'_e\right]} \right) \Bigg|_{\vec{q}=\vec{k}'_e - \vec{k}_e + \vec{G}'}$$

$$= \frac{4\pi^3 n_\chi \bar{\sigma}_e}{V \mu_{\chi e}^2} \sum_{\vec{G}'} \left| f_{\left[i\vec{k}_e, i'\vec{k}'_e, \vec{G}'\right]} \right|^2 |F_{\rm DM}(q)|^2 \times \tag{3.F.59}$$

$$\times \frac{1}{q} \int v \mathrm{d}v \, g_\chi(v) \, \theta\left(v - \left(\frac{q}{2m_\chi} + \frac{\Delta E_{\left[i\vec{k}_e, i'\vec{k}'_e\right]}}{q} \right) \right) \Bigg|_{\vec{q}=\vec{k}'_e - \vec{k}_e + \vec{G}'} =$$

$$= \frac{\pi^2 n_\chi \bar{\sigma}_e}{V \mu_{\chi e}^2} \sum_{\vec{G}'} \left| f_{\left[i\vec{k}_e, i'\vec{k}'_e, \vec{G}'\right]} \right|^2 |F_{\rm DM}(q)|^2 \frac{1}{q} \eta\left(v_{\rm min}\left(\Delta E_{\left[i\vec{k}_e, i'\vec{k}'_e\right]}, q \right) \right) \Bigg|_{\vec{q}=\vec{k}'_e - \vec{k}_e + \vec{G}'} \tag{3.F.60}$$

where

$$v_{\rm min}(\Delta E, q) \equiv \frac{\Delta E}{q} + \frac{q}{2m_\chi} \tag{3.F.61}$$

$$\eta(v_0) \equiv 4\pi \int_0^\infty \mathrm{d}v \, v g_\chi(v) \, \theta(v - v_0) \tag{3.F.62}$$

This almost final result is exactly identical to the one in Eq. 3.E.15. Now our job is to generalize this expression to the exciton case and then bring the calculation to an end. Let us consider an exciton state and, analogously to

Eq. 3.F.44, compute the following expectation value:

$$\langle \vec{p}_\chi - \vec{q}, \left\{ S, \vec{k} \right\} | iT | \vec{p}_\chi, 0 \rangle = \tag{3.F.63}$$

$$= \sum_{i,i',k_e} A^{S\,*}_{i',\vec{k}_e+\vec{k},i,\vec{k}_e} \langle \vec{p}_\chi - \vec{q}, \left\{ i', \vec{k}_e + \vec{k}, i, \vec{k}_e \right\} | iT | \vec{p}_\chi, 0 \rangle = \tag{3.F.64}$$

$$= \sum_{i,i',k_e,\vec{G}',\vec{G}} A^{S\,*}_{i',\vec{k}_e+\vec{k},i,\vec{k}_e} u^*_{i'} \left(\vec{k}_e + \vec{k} + \vec{G}' + \vec{G} \right) u_i \left(\vec{k}_e + \vec{G} \right) \times \tag{3.F.65}$$

$$\times (2\pi)^3 \delta^{(3)} \left(\vec{k} - \vec{q} + \vec{G}' \right) \mathcal{M}_{\text{free}} (\vec{q}) =$$

$$= \sum_{\vec{G}'} (2\pi)^3 \delta^{(3)} \left(\vec{k} - \vec{q} + \vec{G}' \right) f_{\left[S\vec{k},\vec{G}'\right]} \mathcal{M}_{\text{free}} (\vec{q}) \tag{3.F.66}$$

and thus

$$\left| \langle \vec{p}_\chi - \vec{q}, \left\{ S, \vec{k} \right\} | iT | \vec{p}_\chi, 0 \rangle \right|^2 = V \sum_{\vec{G}'} (2\pi)^3 \delta^{(3)} \left(\vec{k} - \vec{q} + \vec{G}' \right) \times \\ \times \left| f_{\left[S\vec{k},\vec{G}'\right]} \right|^2 \left| \mathcal{M}_{\text{free}} (\vec{q}) \right|^2 \tag{3.F.67}$$

with

$$f_{\left[S\vec{k},\vec{G}'\right]} \equiv \sum_{i,i',k_e,\vec{G}} A^{S\,*}_{i',\vec{k}_e+\vec{k},i,\vec{k}_e} u^*_{i'} \left(\vec{k}_e + \vec{k} + \vec{G}' + \vec{G} \right) u_i \left(\vec{k}_e + \vec{G} \right) \tag{3.F.68}$$

$$= V \sum_{i,i'} \int_{\text{BZ}} \frac{\mathrm{d}^3 k_e}{(2\pi)^3} A^{S\,*}_{i',\vec{k}_e+\vec{k},i,\vec{k}_e} f_{\left[i\vec{k}_e,i'\vec{k}_e+\vec{k},\vec{G}'\right]} \tag{3.F.69}$$

From which we see that the only adjustments we need to make are the following replacements:

$$\vec{k}'_e - \vec{k}_e \rightarrow \vec{k} \tag{3.F.70}$$

$$\Delta E_{\left[i\vec{k}_e,i'\vec{k}'_e\right]} \rightarrow \Delta E_{\left[S\vec{k}\right]} \tag{3.F.71}$$

$$\left| f_{\left[i\vec{k}_e,i'\vec{k}_e+\vec{k},\vec{G}'\right]} \right|^2 \rightarrow \left| f_{\left[S\vec{k},\vec{G}'\right]} \right|^2 \tag{3.F.72}$$

which yields

$$R_{\text{G.S.}\to S\vec{k}} = \frac{\pi^2 n_\chi \bar{\sigma}_e}{V \mu_{\chi e}^2} \sum_{\vec{G}'} \left| f_{\left[S\vec{k},\vec{G}'\right]} \right|^2 \left| F_{\text{DM}}\left(q\right) \right|^2 \frac{1}{q} \eta \left(v_{\min}\left(\Delta E_{\left[S\vec{k}\right]}, q \right) \right) \Bigg|_{\vec{q}=\vec{k}+\vec{G}'} \tag{3.F.73}$$

Now let's get to the total rate, summing over all possible final states (and the two-fold degeneracy of the ground state electrons)

$$R_{\text{crystal}} = \frac{2\pi^2 n_\chi \bar{\sigma}_e}{\mu_{\chi e}^2} \sum_{S,\vec{G}'} \int_{\text{BZ}} \frac{\mathrm{d}^3 k}{\left(2\pi\right)^3} \left| f_{\left[S\vec{k},\vec{G}'\right]} \right|^2 \left| F_{\text{DM}}\left(q\right) \right|^2 \frac{1}{q} \eta \left(v_{\min}\left(\Delta E_{\left[S\vec{k}\right]}, q \right) \right) \Bigg|_{\vec{q}=\vec{k}+\vec{G}'} \tag{3.F.74}$$

Now, if we are interested in the differential rate, we insert delta functions

$$\begin{aligned} R_{\text{crystal}} = \frac{2\pi^2 n_\chi \bar{\sigma}_e}{\mu_{\chi e}^2} \int \mathrm{d}\ln\left(E_e\right) \mathrm{d}\ln(q) \int_{\text{BZ}} \frac{\mathrm{d}^3 k}{\left(2\pi\right)^3} \sum_{S,\vec{G}'} q\, \delta\left(q - \left| \vec{k} + \vec{G}' \right| \right) \times \\ \times E_e \delta\left(E_e - \Delta E_{\left[S\vec{k}\right]} \right) \left| f_{\left[S\vec{k},\vec{G}'\right]} \right|^2 \left| F_{\text{DM}}\left(q\right) \right|^2 \frac{1}{q} \eta\left(v_{\min}\left(E_e, q \right) \right) \end{aligned} \tag{3.F.75}$$

Now write $V = V_{\text{cell}} N_{\text{cell}}$ and take a log-derivative in energy.

$$\begin{aligned} \frac{\mathrm{d}R_{\text{crystal}}}{\mathrm{d}\ln\left(E_e\right)} = \alpha\, n_\chi \bar{\sigma}_e N_{\text{cell}} \frac{m_e^2}{\mu_{\chi e}^2} \int \mathrm{d}\ln(q) \left| F_{\text{DM}}\left(q\right) \right|^2 \frac{E_e}{q} \eta\left(v_{\min}\left(E_e, q \right) \right) \times \\ \times \left| f_{\text{crystal}}\left(q, E_e\right) \right|^2 \end{aligned} \tag{3.F.76}$$

where we define an overall crystal form factor

$$\begin{aligned} \left| f_{\text{crystal}}\left(q, E_e\right) \right|^2 \equiv \frac{2\pi^2 N_{\text{cell}}}{\alpha m_e^2 E_e} \sum_S \int_{\text{BZ}} \frac{V_{\text{cell}} \mathrm{d}^3 k}{\left(2\pi\right)^3} E_e \times \\ \times \delta\left(E_e - \Delta E_{\left[S\vec{k}\right]} \right) \sum_{\vec{G}'} q\, \delta\left(q - \left| \vec{k} + \vec{G}' \right| \right) \times \\ \times \left| \sum_{i,i'} \int_{\text{BZ}} \frac{V_{\text{cell}} \mathrm{d}^3 k_e}{\left(2\pi\right)^3} A^{S\,*}_{i',\vec{k}_e+\vec{k},i,\vec{k}_e} f_{\left[i\vec{k}_e, i'\vec{k}_e+\vec{k}, \vec{G}'\right]} \right|^2 \end{aligned} \tag{3.F.77}$$

3.F.3 Discussion

As already discussed in Sec. 3.B, excitonic effects are typically large only within the first few meV around the conduction band's edge, which is why we safely ignore them in our calculations. In other cases neglecting them is fine because it will typically lead to a conservative result. At any rate, if for some reason one needed to include them, our formulae above allow to do so. However, we must point out that calculating the coefficients $A^S_{i',\vec{k}_e+\vec{k},i,\vec{k}_e}$ is an extremely laborious matter and is an active area of research within computational condensed matter. We refer the reader to software such as BerkeleyGW [283] and Yambo [284] for current examples of such computations.

3.G Spin dependence

As noted at the end of Sec. 3.2.1, some materials, including TlBr, can receive important contributions to their electronic structure from the spin-orbit magnetic coupling between the electron's spin and orbital angular momentum. This interaction results in the spin-degenerate band structure to split in energy into twice as many bands. This will in general alter the scattering rates, especially if the dark matter particle interaction matrix element is itself spin dependent (a case which we will not treat in depth here).

The aim of this section is to derive the scattering rate for electronic excitations when these are not diagonal in spin, *e.g.* because of spin-orbit coupling. The degenerate states labeled by band index i and spin indices $s = +, -$ will now be replaced by two non-degenerate states labeled by $i, a = 1$ and $i, a = 2$. These states can be expanded on a basis of spin eigenfunctions (which we will use in 3.G.81). Let us start from the free cross section of Eq. 3.F.41 and write out explicitly the spin indices.

$$\begin{aligned}(\sigma v)^{\text{free}}_{1\to 2} = \frac{1}{2}\sum_{\alpha,\beta}\frac{1}{4E^{\alpha}_{\chi}E^{\beta}_{e}}\sum_{\gamma,\delta}\int\frac{\mathrm{d}^3q}{(2\pi)^3}\frac{\mathrm{d}^3k'_e}{(2\pi)^3}\frac{1}{4E'^{\gamma}_{\chi}E'^{\delta}_{e}}\times \\ \times(2\pi)^4\,\delta\left(E'_{\gamma\delta}-E_{\alpha\beta}\right)\delta^{(3)}\left(\vec{k}'_e-\vec{k}_e-\vec{q}\right)\left|\mathcal{M}^{\alpha\beta\gamma\delta}_{\text{free}}\left(\vec{q}\right)\right|^2\end{aligned} \tag{3.G.78}$$

Now I will repeat the derivation of Sec. 3.F.2, just adding explicit spin indices wherever appropriate.

$$\langle \vec{p}_\chi - \vec{q}, \gamma, \vec{k}'_e, \delta | T | \vec{p}_\chi, \alpha, \vec{k}_e, \beta \rangle = (2\pi)^3 \delta^{(3)} \left(\vec{k}'_e - \vec{k}_e - \vec{q} \right) \times \\ \times \mathcal{M}_{\text{free}}^{\alpha\beta\gamma\delta} (\vec{q}) \tag{3.G.79}$$

whence

$$\left| \langle \vec{p}_\chi - \vec{q}, \gamma, \vec{k}'_e, \delta | T | \vec{p}_\chi, \alpha, \vec{k}_e, \beta \rangle \right|^2 = V (2\pi)^3 \delta^{(3)} \left(\vec{k}'_e - \vec{k}_e - \vec{q} \right) \times \\ \times \left| \mathcal{M}_{\text{free}}^{\alpha\beta\gamma\delta} (\vec{q}) \right|^2 \tag{3.G.80}$$

In the bound case:

$$\langle \vec{p}_\chi - \vec{q}, \gamma, \left\{ i', a', \vec{k}'_e, i, a, \vec{k}_e \right\} | T | \vec{p}_\chi, \alpha, 0 \rangle = \tag{3.G.81}$$

$$= \sum_{s,s'} \sum_{\vec{G}', \vec{G}} u^{s'*}_{i',a'} \left(\vec{k}'_e + \vec{G}' + \vec{G} \right) u^{s}_{i,a} \left(\vec{k}_e + \vec{G} \right) (2\pi)^3 \times \tag{3.G.82}$$

$$\times \delta^{(3)} \left(\vec{k}'_e - \vec{k}_e - \vec{q} + \vec{G}' \right) \mathcal{M}_{\text{free}}^{\alpha s \gamma s'} (\vec{q}) =$$

$$= \sum_{\vec{G}'} (2\pi)^3 \delta^{(3)} \left(\vec{k}'_e - \vec{k}_e - \vec{q} + \vec{G}' \right) \sum_{s,s'} f_{\left[i a \vec{k}_e s, i' a' \vec{k}'_e s', \vec{G}' \right]} \mathcal{M}_{\text{free}}^{\alpha s \gamma s'} (\vec{q}) \Rightarrow \tag{3.G.83}$$

$$\left| \langle \vec{p}_\chi - \vec{q}, \gamma, \left\{ i', a', \vec{k}'_e, i, a, \vec{k}_e \right\} | iT | \vec{p}_\chi, \alpha, 0 \rangle \right|^2 = \tag{3.G.84}$$

$$= V \sum_{\vec{G}'} (2\pi)^3 \delta^{(3)} \left(\vec{k}'_e - \vec{k}_e - \vec{q} + \vec{G}' \right) \left| \sum_{s,s'} f_{\left[i a \vec{k}_e s, i' a' \vec{k}'_e s', \vec{G}' \right]} \mathcal{M}_{\text{free}}^{\alpha s \gamma s'} (\vec{q}) \right|^2$$

So, comparing (3.G.80) and (3.G.84), I operate the following replacement in (3.G.78)

$$\delta^{(3)} \left(\vec{k}'_e - \vec{k}_e - \vec{q} \right) \left| \mathcal{M}_{\text{free}}^{\alpha\beta\gamma\delta} (\vec{q}) \right|^2 \to \sum_{\vec{G}'} \delta^{(3)} \left(\vec{k}'_e - \vec{k}_e - \vec{q} + \vec{G}' \right) \times \\ \times \left| \sum_{s,s'} f_{\left[i a \vec{k}_e s, i' a' \vec{k}'_e s', \vec{G}' \right]} \mathcal{M}_{\text{free}}^{\alpha s \gamma s'} (\vec{q}) \right|^2 \tag{3.G.85}$$

and I get

$$(\sigma v)^{\text{bound}}_{1\to 2} = \frac{1}{2}\sum_{\alpha,a}\frac{1}{4E_\chi^\alpha E_e^a}\sum_{\gamma,a'}\int\frac{\mathrm{d}^3q}{(2\pi)^3}\frac{\mathrm{d}^3k'_e}{(2\pi)^3}\frac{1}{4E'_\chi{}^\gamma E'^{a'}_e}(2\pi)^4\,\delta\left(E'_{\gamma a'}-E_{\alpha a}\right)\times \\ \times\sum_{\vec{G}'}\delta^{(3)}\left(\vec{k}'_e-\vec{k}_e-\vec{q}+\vec{G}'\right)\left|\sum_{s,s'}f_{\left[ia\vec{k}_e s,i'a'\vec{k}'_e s',\vec{G}'\right]}\mathcal{M}^{\alpha s\gamma s'}_{\text{free}}(\vec{q})\right|^2 \tag{3.G.86}$$

Before proceeding any further, we shall assume that

1. $\mathcal{M}^{\alpha\beta\gamma\delta}_{\text{free}}(\vec{q}) = \mathcal{M}_{\text{free}}(\vec{q})$

2. $E_\chi^\alpha = E_\chi$, $E'_\chi{}^\gamma = E'_\chi$

This means that the DM-electron interaction is assumed to be spin-independent and that spin is a good quantum number for the DM particle. We will also denote

$$f_{\left[ia\vec{k}_e,i'a'\vec{k}'_e,\vec{G}'\right]} \equiv \sum_{s,s'}\sum_{\vec{G}}u^{s'*}_{i',a'}\left(\vec{k}'_e+\vec{G}'+\vec{G}\right)u^s_{i,a}\left(\vec{k}_e+\vec{G}\right) \tag{3.G.87}$$

$$= \sum_{s,s'}f_{\left[ia\vec{k}_e s,i'a'\vec{k}'_e s',\vec{G}'\right]} \tag{3.G.88}$$

Now, the final electron momentum is fixed, so we have $\int\frac{\mathrm{d}^3k'_e}{(2\pi)^3}\to\frac{1}{V}$, then I use the delta function to get rid of the $\int\mathrm{d}^3q$ integral:

$$(\sigma v)^{\text{bound}}_{1\to 2} = \frac{4}{2}\,\frac{1}{4E_\chi E_e^a}\frac{1}{V}\sum_{\vec{G}'}\frac{1}{4E'_\chi E'^{a'}_e}(2\pi)\,\delta\left(E'_{a'}-E_a\right)\left|f_{\left[ia\vec{k}_e,i'a'\vec{k}'_e,\vec{G}'\right]}\right|^2\left|\mathcal{M}_{\text{free}}(\vec{q})\right|^2\Big|_{\vec{q}=\vec{k}'_e-\vec{k}_e+\vec{G}'} \tag{3.G.89}$$

In the non relativistic regime

$$\begin{aligned} E_a &= E_\chi + E_e^a = m_\chi + \frac{1}{2} m_\chi v^2 + m_e + E_{fermi} \\ &\approx m_\chi + m_e \end{aligned} \tag{3.G.90}$$

$$\begin{aligned} E'_{a'} &= E'_\chi + E_e'^{a'} = m_\chi + \frac{\left(m_\chi \vec{v} - \vec{q}\right)^2}{2m_\chi} + m_e + E_{fermi} + \\ &\quad + \Delta E_{\left[i a \vec{k}_e, i' a' \vec{k}'_e\right]} \approx m_\chi + m_e \end{aligned} \tag{3.G.91}$$

$$E'_{a'} - E_a = \frac{q^2}{2m_\chi} - \vec{v} \cdot \vec{q} + \Delta E_{\left[i a \vec{k}_e, i' a' \vec{k}'_e\right]} \tag{3.G.92}$$

Now again the usual definitions.

$$\frac{4}{2} \left|\mathcal{M}_{\text{free}}(q)\right|^2 \equiv \overline{\left|\mathcal{M}_{\text{free}}(\alpha m_e)\right|^2} \left|F_{\text{DM}}(q)\right|^2 \tag{3.G.93}$$

$$\bar{\sigma}_e \equiv \frac{\mu_{\chi e}^2 \overline{\left|\mathcal{M}_{\text{free}}(\alpha m_e)\right|^2}}{16\pi m_\chi^2 m_e^2} \tag{3.G.94}$$

Hence,

$$(\sigma v)_{1\to 2}^{\text{bound}} = \frac{2\pi^2 \bar{\sigma}_e}{V \mu_{\chi e}^2} \sum_{\vec{G}'} \delta\left(\frac{q^2}{2m_\chi} - \vec{v} \cdot \vec{q} + \Delta E_{\left[i a \vec{k}_e, i' a' \vec{k}'_e\right]}\right) \left|f_{\left[i a \vec{k}_e, i' a' \vec{k}'_e, \vec{G}'\right]}\right|^2 \left|F_{\text{DM}}(q)\right|^2 \Bigg|_{\vec{q} = \vec{k}'_e - \vec{k}_e + \vec{G}'} \tag{3.G.95}$$

Now, plug this into (3.F.40) and get (where we choose the z_v axis along $\vec{q}$ and assume $g_\chi(\vec{v}) \equiv g_\chi(v)$)

$$R_{1\to 2} = \frac{\pi^2 n_\chi \bar{\sigma}_e}{V \mu_{\chi e}^2} \sum_{\vec{G}'} \left|f_{\left[i a \vec{k}_e, i' a' \vec{k}'_e, \vec{G}'\right]}\right|^2 \left|F_{\text{DM}}(q)\right|^2 \frac{1}{q} \eta\left(v_{\min}\left(\Delta E_{\left[i a \vec{k}_e, i' a' \vec{k}'_e\right]}, q\right)\right) \Bigg|_{\vec{q} = \vec{k}'_e - \vec{k}_e + \vec{G}'} \tag{3.G.96}$$

Now we have for the total rate, summing over all possible final and initial

states.

$$R_{\text{crystal}} = \frac{\pi^2 n_\chi \bar{\sigma}_e}{\mu_{\chi e}^2} V \sum_{a,a',i,i',\vec{G}'} \int_{\text{BZ}} \frac{\mathrm{d}^3 k_e \mathrm{d}^3 k'_e}{(2\pi)^6} \left| f_{\left[i\vec{a}\vec{k}_e, i'a'\vec{k}'_e, \vec{G}'\right]} \right|^2 \times \\ \times \left| F_{\text{DM}}(q) \right|^2 \frac{1}{q} \eta \left(v_{\text{min}} \left(\Delta E_{\left[i\vec{a}\vec{k}_e, i'a'\vec{k}'_e\right]}, q \right) \right) \Big|_{\vec{q}=\vec{k}'_e - \vec{k}_e + \vec{G}'} \tag{3.G.97}$$

Now again, if we want the differential rate:

$$\frac{\mathrm{d}R_{\text{crystal}}}{\mathrm{d}\ln(E_e)} = \alpha\, n_\chi \bar{\sigma}_e N_{\text{cell}} \frac{m_e^2}{\mu_{\chi e}^2} \int \mathrm{d}\ln(q) \left| F_{\text{DM}}(q) \right|^2 \frac{E_e}{q} \eta \left(v_{\text{min}}(E_e, q) \right) \times \\ \times \left| f_{\text{crystal}}(q, E_e) \right|^2 \tag{3.G.98}$$

where we define an overall crystal form factor

$$\left| f_{\text{crystal}}(q, E_e) \right|^2 \equiv \frac{\pi^2}{\alpha m_e^2 E_e V_{\text{cell}}} \sum_{a,a',i,i'} \int_{\text{BZ}} \frac{V_{\text{cell}} \mathrm{d}^3 k_e}{(2\pi)^3} \frac{V_{\text{cell}} \mathrm{d}^3 k'_e}{(2\pi)^3} E_e\, \delta \left(E_e - \Delta E_{\left[i\vec{a}\vec{k}_e, i'a'\vec{k}'_e\right]} \right) \times \\ \times \sum_{\vec{G}'} q\, \delta \left(q - \left| \vec{k}'_e - \vec{k}_e + \vec{G}' \right| \right) \left| f_{\left[i\vec{a}\vec{k}_e, i'a'\vec{k}'_e, \vec{G}'\right]} \right|^2 \tag{3.G.99}$$

This final result is entirely analogous to Eq. 3.E.20, with the simple replacement of the form factor with the appropriate spin-dependent one defined in Eq. 3.G.88, as well as the new band energies.

3.G.1 Discussion

Fortunately, software such as quantum espresso can handle the effects of spin-orbit coupling. Therefore, we were able to perform the complete calculation for the scattering rate in TlBr, where the impact of this change is expected be the highest, according to Eq. 3.G.97 above, and verified that the overall change in the result, as opposed to neglecting the spin-orbit effects altogether, is less than 10%. Given that we have several other larger sources of uncertainty in these estimations, as discussed in the main body of this chapter, spin-orbit coupling effects are not expected to be essential in calculations of scattering

rates.

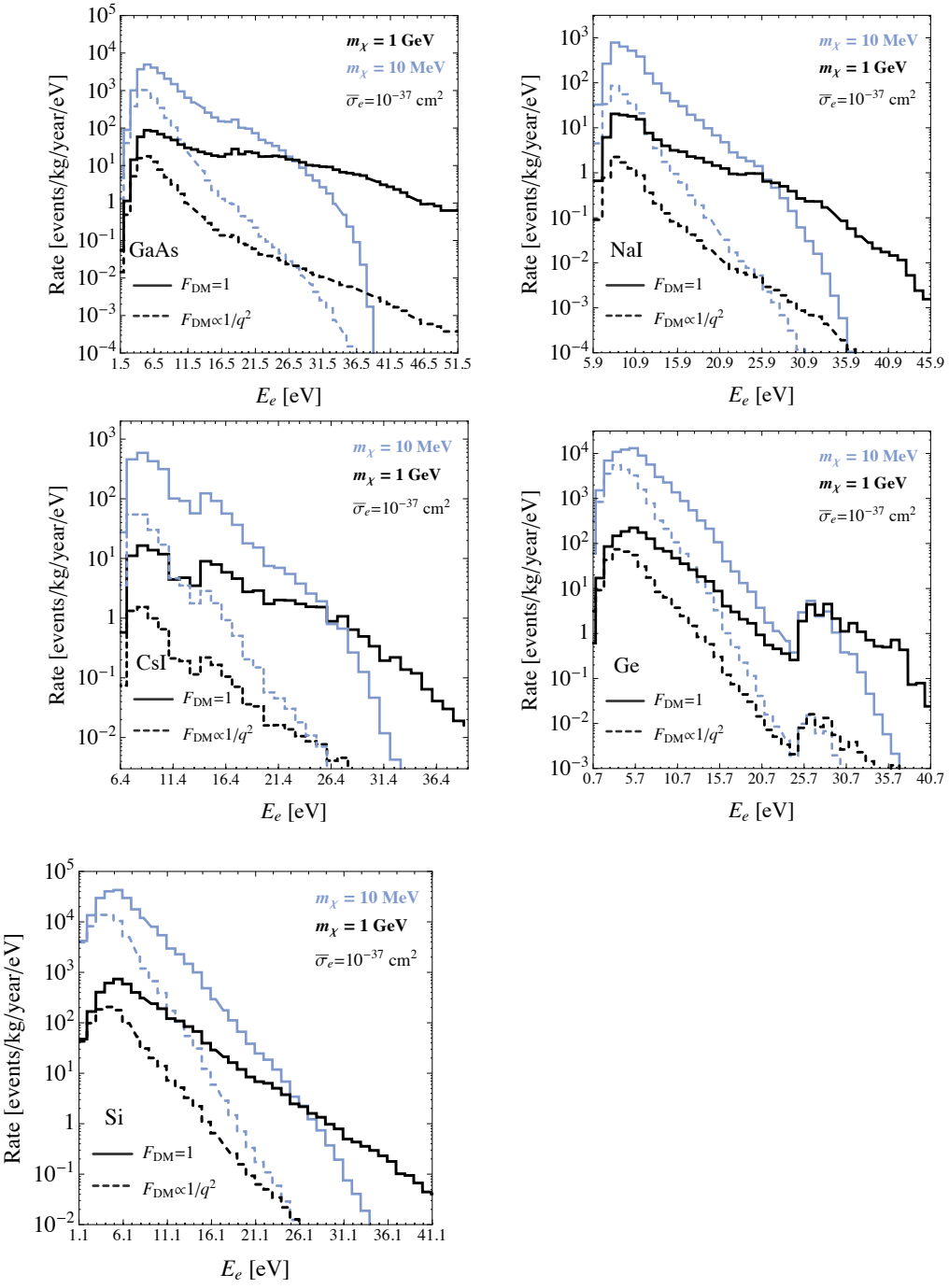

Figure 3.B.1: Electron recoil spectra from DM-electron scattering in GaAs, NaI, CsI, Ge, and Si as a function of total deposited energy E_e, for m_χ = 10 MeV (blue lines) and 1 GeV (black lines) and DM form factors $F_{\rm DM} = 1$ (solid lines) and $F_{\rm DM} = (\alpha m_e/q)^2$ (dashed lines). We fix $\overline{\sigma}_e = 10^{-37}{\rm cm}^2$ and assume an exposure of 1 kg-year. The E_e-axis begins at the band-gap energies E_g.

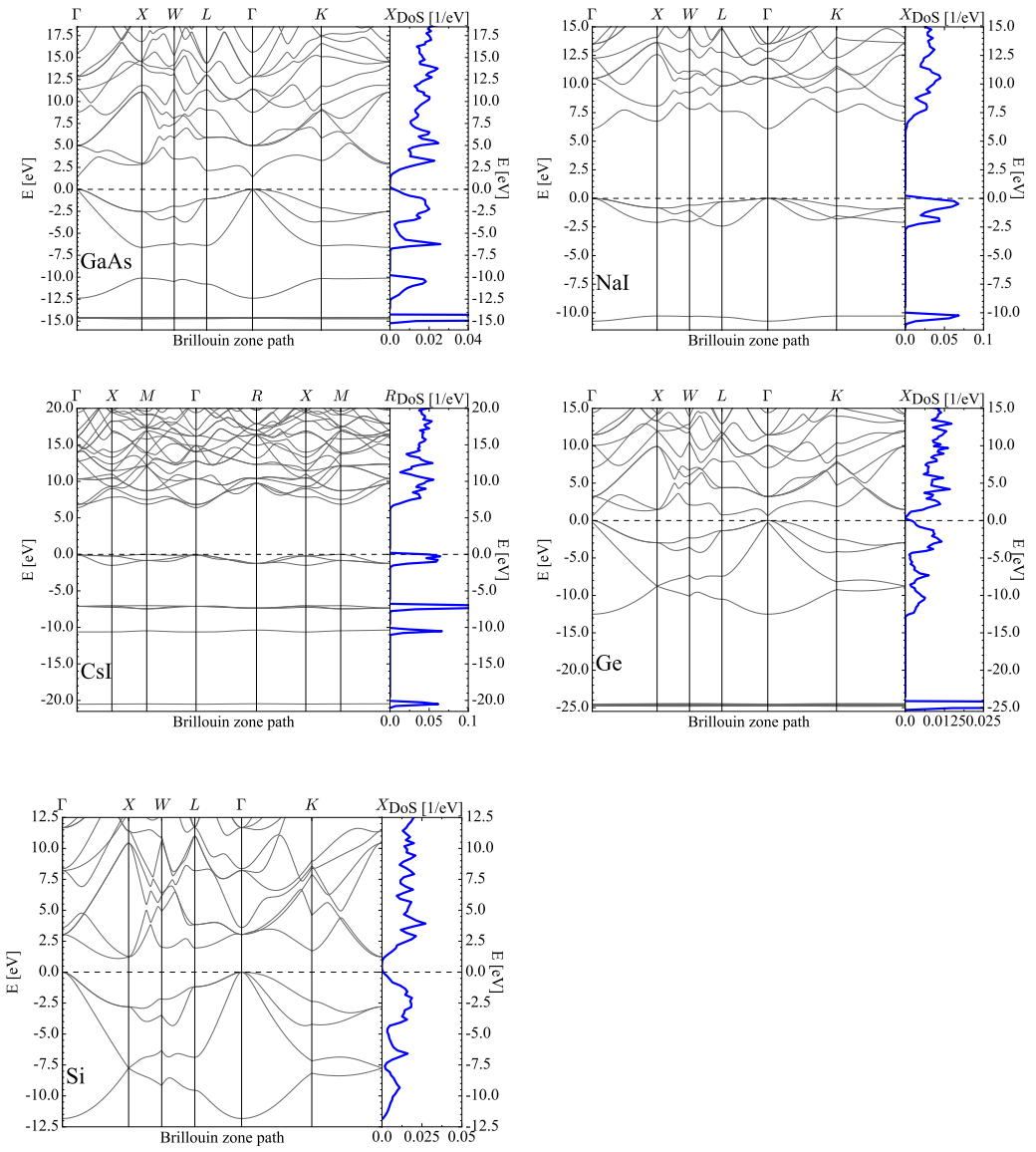

Figure 3.B.2: Calculated band structure (black lines) and density of states (DoS, blue lines) of the electronic states for gallium arsenide (GaAs), sodium iodide (NaI), caesium iodide (CsI), germanium (Ge), and silicon (Si). We show all valence electron states included in our DM-electron-scattering-rate calculation as well as the bottom of the conduction band. The DoS was calculated by smearing the energy with a Gaussian function of width $\delta E = 0.25$ eV.

Bibliography

[1] P. Langacker, *The standard model and beyond*. Series in High Energy Physics, Cosmology and Gravitation. Taylor and Francis, Boca Raton, FL, 2010.

[2] C. Misner, K. Thorne, and J. Wheeler, *Gravitation*. W.H. Freeman and Company, 1973.

[3] G. Aad, T. Abajyan, B. Abbott, J. Abdallah, S. Abdel Khalek, A. A. Abdelalim, O. Abdinov, R. Aben, B. Abi, M. Abolins, and et al., *Observation of a new particle in the search for the Standard Model Higgs boson with the ATLAS detector at the LHC*, *Physics Letters B* **716** (Sept., 2012) 1–29, [arXiv:1207.7214].

[4] **LIGO Scientific Collaboration and Virgo Collaboration** Collaboration, B. P. Abbott *et. al.*, *Observation of gravitational waves from a binary black hole merger*, *Phys. Rev. Lett.* **116** (Feb, 2016) 061102.

[5] R. D. Peccei, *The Strong CP problem and axions*, *Lect. Notes Phys.* **741** (2008) 3–17, [hep-ph/0607268]. [,3(2006)].

[6] R. N. Mohapatra *et. al.*, *Theory of neutrinos: A White paper*, *Rept. Prog. Phys.* **70** (2007) 1757–1867, [hep-ph/0510213].

[7] H. Georgi, *The flavor problem*, *Physics Letters B* **169** (1986), no. 2 231 – 233.

[8] K. S. Babu, *TASI Lectures on Flavor Physics*, in *Proceedings of Theoretical Advanced Study Institute in Elementary Particle Physics on The dawn of the LHC era (TASI 2008)*, pp. 49–123, 2010. arXiv:0910.2948.

[9] S. Raby, *Grand Unified Theories*, in *2nd World Summit: Physics Beyond the Standard Model Galapagos, Islands, Ecuador, June 22-25, 2006*, 2006. hep-ph/0608183.

[10] M. Dine, *Naturalness Under Stress*, *Ann. Rev. Nucl. Part. Sci.* **65** (2015) 43–62, [arXiv:1501.0103].

[11] R. P. Woodard, *How Far Are We from the Quantum Theory of Gravity?*, *Rept. Prog. Phys.* **72** (2009) 126002, [arXiv:0907.4238].

[12] J. M. Cline, *Baryogenesis*, in *Les Houches Summer School - Session 86: Particle Physics and Cosmology: The Fabric of Spacetime Les Houches, France, July 31-August 25, 2006*, 2006. hep-ph/0609145.

[13] M.-C. Chen, *TASI 2006 Lectures on Leptogenesis*, in *Proceedings of Theoretical Advanced Study Institute in Elementary Particle Physics : Exploring New Frontiers Using Colliders and Neutrinos (TASI 2006)*, pp. 123–176, 2007. hep-ph/0703087.

[14] J. Martin, *Everything You Always Wanted To Know About The Cosmological Constant Problem (But Were Afraid To Ask)*, *Comptes Rendus Physique* **13** (2012) 566–665, [arXiv:1205.3365].

[15] G. Bertone, D. Hooper, and J. Silk, *Particle dark matter: Evidence, candidates and constraints*, *Phys.Rept.* **405** (2005) 279–390, [hep-ph/0404175].

[16] J. Yoo and Y. Watanabe, *Theoretical Models of Dark Energy*, *International Journal of Modern Physics D* **21** (Dec., 2012) 1230002, [arXiv:1212.4726].

[17] **Planck** Collaboration, P. A. R. Ade *et. al.*, *Planck 2015 results. XIII. Cosmological parameters*, arXiv:1502.0158.

[18] F. Zwicky, *On the Masses of Nebulae and of Clusters of Nebulae*, *The Astrophysical Journal* **86** (oct, 1937) 217.

[19] M. Milgrom, *A modification of the Newtonian dynamics as a possible alternative to the hidden mass hypothesis*, *The Astrophysical Journal* **270** (July, 1983) 365–370.

[20] V. C. Rubin and W. K. Ford, Jr., *Rotation of the Andromeda Nebula from a Spectroscopic Survey of Emission Regions*, *The Astrophysical Journal* **159** (Feb., 1970) 379.

[21] K. G. Begeman, A. H. Broeils, and R. H. Sanders, *Extended rotation curves of spiral galaxies - Dark haloes and modified dynamics*, *Mon. Not. R. Astr. Soc.* **249** (Apr., 1991) 523–537.

[22] W. Hu and S. Dodelson, *Cosmic microwave background anisotropies*, *Ann. Rev. Astron. Astrophys.* **40** (2002) 171–216, [astro-ph/0110414].

[23] **Planck** Collaboration, P. A. R. Ade *et. al.*, *Planck 2013 results. I. Overview of products and scientific results*, *Astron. Astrophys.* **571** (2014) A1, [arXiv:1303.5062].

[24] Planck Collaboration, P. A. R. Ade, N. Aghanim, M. Arnaud, M. Ashdown, J. Aumont, C. Baccigalupi, A. J. Banday, R. B. Barreiro, J. G. Bartlett, and et al., *Planck 2015 results. XIII. Cosmological parameters*, *ArXiv e-prints* (Feb., 2015) [arXiv:1502.0158].

[25] R. H. Cyburt, B. D. Fields, K. A. Olive, and T.-H. Yeh, *Big Bang Nucleosynthesis: 2015*, arXiv:1505.0107.

[26] M. Vogelsberger, S. Genel, V. Springel, P. Torrey, D. Sijacki, D. Xu, G. F. Snyder, D. Nelson, and L. Hernquist, *Introducing the Illustris Project: Simulating the coevolution of dark and visible matter in the*

Universe, *Mon. Not. Roy. Astron. Soc.* **444** (2014), no. 2 1518–1547, [arXiv:1405.2921].

[27] J. Diemand, M. Kuhlen, and P. Madau, *Dark matter substructure and gamma-ray annihilation in the Milky Way halo*, *Astrophys. J.* **657** (2007) 262–270, [astro-ph/0611370].

[28] W. Tucker, P. Blanco, S. Rappoport, L. David, D. Fabricant, E. E. Falco, W. Forman, A. Dressler, and M. Ramella, *1e0657-56: a contender for the hottest known cluster of galaxies*, *Astrophys. J.* **496** (1998) L5, [astro-ph/9801120].

[29] J. A. Tyson, F. Valdes, and R. A. Wenk, *Detection of systematic gravitational lens galaxy image alignments - Mapping dark matter in galaxy clusters*, *The Astrophysical Journal Letters* **349** (Jan., 1990) L1–L4.

[30] D. Clowe, M. Bradac, A. H. Gonzalez, M. Markevitch, S. W. Randall, C. Jones, and D. Zaritsky, *A direct empirical proof of the existence of dark matter*, *Astrophys. J.* **648** (2006) L109–L113, [astro-ph/0608407].

[31] F. Kahlhoefer, K. Schmidt-Hoberg, M. T. Frandsen, and S. Sarkar, *Colliding clusters and dark matter self-interactions*, *Mon. Not. Roy. Astron. Soc.* **437** (2014), no. 3 2865–2881, [arXiv:1308.3419].

[32] M. Markevitch, *Chandra observation of the most interesting cluster in the universe*, astro-ph/0511345. [ESA Spec. Publ.604,723(2006)].

[33] J. L. Feng, *Dark Matter Candidates from Particle Physics and Methods of Detection*, *Ann. Rev. Astron. Astrophys.* **48** (2010) 495–545, [arXiv:1003.0904].

[34] B. Paczynski, *Gravitational microlensing by the galactic halo*, *Astrophys. J.* **304** (May, 1986) 1–5.

[35] **MACHO** Collaboration, C. Alcock *et. al.*, *The MACHO project: Microlensing results from 5.7 years of LMC observations*, *Astrophys. J.* **542** (2000) 281–307, [astro-ph/0001272].

[36] R. D. Peccei and H. R. Quinn, CP *conservation in the presence of pseudoparticles*, *Phys. Rev. Lett.* **38** (Jun, 1977) 1440–1443.

[37] **ACME** Collaboration, J. Baron *et. al.*, *Order of Magnitude Smaller Limit on the Electric Dipole Moment of the Electron*, *Science* **343** (2014) 269–272, [arXiv:1310.7534].

[38] P. Sikivie, *Experimental tests of the "invisible" axion*, *Phys. Rev. Lett.* **51** (Oct, 1983) 1415–1417.

[39] S. J. Asztalos, G. Carosi, C. Hagmann, D. Kinion, K. van Bibber, M. Hotz, L. J. Rosenberg, G. Rybka, J. Hoskins, J. Hwang, P. Sikivie, D. B. Tanner, R. Bradley, and J. Clarke, *Squid-based microwave cavity search for dark-matter axions*, *Phys. Rev. Lett.* **104** (Jan, 2010) 041301.

[40] J. R. Primack, *Dark Matter and Galaxy Formation*, in *American Institute of Physics Conference Series* (F. Roig, D. Lopes, R. de La Reza, and V. Ortega, eds.), vol. 1192 of *American Institute of Physics Conference Series*, pp. 101–137, Dec., 2009. arXiv:0909.2021.

[41] B. W. Lee and S. Weinberg, *Cosmological lower bound on heavy-neutrino masses*, *Phys. Rev. Lett.* **39** (Jul, 1977) 165–168.

[42] E. Kolb and M. Turner, *The Early Universe*. Frontiers in physics. Westview Press, 1994.

[43] P. Gondolo and G. Gelmini, *Cosmic abundances of stable particles: improved analysis.*, *Nuclear Physics B* **360** (Aug., 1991) 145–179.

[44] J. Ellis, J. Hagelin, D. Nanopoulos, K. Olive, and M. Srednicki, *Supersymmetric relics from the big bang*, *Nuclear Physics B* **238** (1984), no. 2 453 – 476.

[45] **ATLAS** Collaboration, G. Aad *et. al.*, *Search for supersymmetry at $\sqrt{s} = 13$ TeV in final states with jets and two same-sign leptons or three leptons with the ATLAS detector*, arXiv:1602.0905.

[46] J. Conrad, *Indirect Detection of WIMP Dark Matter: a compact review*, in *Interplay between Particle and Astroparticle physics London, United Kingdom, August 18-22, 2014*, 2014. arXiv:1411.1925.

[47] C. Weniger, *A Tentative Gamma-Ray Line from Dark Matter Annihilation at the Fermi Large Area Telescope*, *JCAP* **1208** (2012) 007, [arXiv:1204.2797].

[48] **Fermi-LAT** Collaboration, M. Ackermann *et. al.*, *Searching for Dark Matter Annihilation from Milky Way Dwarf Spheroidal Galaxies with Six Years of Fermi Large Area Telescope Data*, *Phys. Rev. Lett.* **115** (2015), no. 23 231301, [arXiv:1503.0264].

[49] **LAT Collaboration** Collaboration, W. Atwood *et. al.*, *The Large Area Telescope on the Fermi Gamma-ray Space Telescope Mission*, *Astrophys.J.* **697** (2009) 1071–1102, [arXiv:0902.1089].

[50] S. P. Ahlen *et. al.*, *An Antimatter spectrometer in space*, *Nucl. Instrum. Meth.* **A350** (1994) 351–367.

[51] **AMS Collaboration** Collaboration, M. Aguilar *et. al.*, *First Result from the Alpha Magnetic Spectrometer on the International Space Station: Precision Measurement of the Positron Fraction in Primary Cosmic Rays of 0.5-350 GeV*, *Phys.Rev.Lett.* **110** (2013) 141102.

[52] **IceCube** Collaboration, J. Ahrens *et. al.*, *Icecube - the next generation neutrino telescope at the south pole*, *Nucl. Phys. Proc. Suppl.* **118** (2003) 388–395, [astro-ph/0209556]. [,388(2002)].

[53] **IceCube** Collaboration, S. Klein, *Recent Highlights from IceCube*, *Braz. J. Phys.* **44** (2014) 540–549, [arXiv:1311.6519]. [,1293(2013)].

[54] R. Abbasi, Y. Abdou, T. Abu-Zayyad, J. Adams, J. A. Aguilar, M. Ahlers, K. Andeen, J. Auffenberg, X. Bai, M. Baker, and et al., *Search for dark matter from the Galactic halo with the IceCube Neutrino Telescope*, *Phys. Rev. D* **84** (July, 2011) 022004, [arXiv:1101.3349].

[55] P. Cushman *et. al.*, *Working Group Report: WIMP Dark Matter Direct Detection*, in *Community Summer Study 2013: Snowmass on the Mississippi (CSS2013) Minneapolis, MN, USA, July 29-August 6, 2013*, 2013. arXiv:1310.8327.

[56] M. W. Goodman and E. Witten, *Detectability of certain dark-matter candidates*, *Phys. Rev. D* **31** (Jun, 1985) 3059–3063.

[57] J. Sander *et. al.*, *Supercdms status from soudan and plans for snolab*, *AIP Conference Proceedings* **1534** (2013), no. 1 129–135.

[58] **CoGeNT** Collaboration, C. E. Aalseth *et. al.*, *CoGeNT: A Search for Low-Mass Dark Matter using p-type Point Contact Germanium Detectors*, *Phys. Rev.* **D88** (2013) 012002, [arXiv:1208.5737].

[59] G. Angloher *et. al.*, *Commissioning run of the cresst-ii dark matter search*, *Astroparticle Physics* **31** (2009), no. 4 270 – 276.

[60] R. Bernabei, P. Belli, V. Landoni, F. Montecchia, N. W. Di, A. Incicchitti, D. Prosperi, C. Bacci, D. C.J., D. L.K., H. Kuang, J. Ma, M. Angelone, P. Bastistoni, and M. Pillon, *New limits on {WIMP} search with large-mass low-radioactivity nai(tl) set-up at gran sasso*, *Physics Letters B* **389** (1996), no. 4 757 – 766.

[61] **DAMA** Collaboration, R. Bernabei *et. al.*, *First results from DAMA/LIBRA and the combined results with DAMA/NaI*, *Eur. Phys. J.* **C56** (2008) 333–355, [arXiv:0804.2741].

[62] A. de Bellefon, I. Berkes, C. Bobin, D. Broszkiewicz, B. Chambon, M. Chapellier, G. Chardin, P. Charvin, V. Chazal, N. Coron, M. D.

JÃ©sus, D. Drain, L. Dumoulin, Y. Giraud-HÃ©raud, C. Goldbach, G. Guerier, J. Hadjout, J. Leblanc, D. Marchand, M. Massaq, Y. Messous, X. Navick, G. Nollez, P. Pari, C. Pastor, M. Perillo-Isaac, I. Prostakov, and D. Yvon, *Dark matter search with a low temperature sapphire bolometer*, *Astroparticle Physics* **6** (1996), no. 1 35 – 43.

[63] **LUX** Collaboration, D. S. Akerib *et. al.*, *The Large Underground Xenon (LUX) Experiment*, *Nucl. Instrum. Meth.* **A704** (2013) 111–126, [arXiv:1211.3788].

[64] **SIMPLE** Collaboration, M. Felizardo *et. al.*, *The SIMPLE Phase II Dark Matter Search*, *Phys. Rev.* **D89** (2014), no. 7 072013, [arXiv:1404.4309].

[65] Xenon100 Collaboration, E. Aprile, *et. al.*, *The XENON100 dark matter experiment*, *Astroparticle Physics* **35** (Apr., 2012) 573–590, [arXiv:1107.2155].

[66] J. Cooley, *Overview of Non-Liquid Noble Direct Detection Dark Matter Experiments*, *Phys. Dark Univ.* **4** (2014) 92–97, [arXiv:1410.4960].

[67] C. Boehm, P. Fayet, and J. Silk, *Light and heavy dark matter particles*, *Phys. Rev.* **D69** (2004) 101302, [hep-ph/0311143].

[68] R. Essig, J. Mardon, and T. Volansky, *Direct Detection of Sub-GeV Dark Matter*, *Phys. Rev.* **D85** (2012) 076007, [arXiv:1108.5383].

[69] A. Askew, S. Chauhan, B. Penning, W. Shepherd, and M. Tripathi, *Searching for Dark Matter at Hadron Colliders*, *Int. J. Mod. Phys.* **A29** (2014) 1430041, [arXiv:1406.5662].

[70] R. Essig, M. Fernandez-Serra, J. Mardon, A. Soto, T. Volansky, and T.-T. Yu, *Direct Detection of sub-GeV Dark Matter with Semiconductor Targets*, arXiv:1509.0159.

[71] A. Abdo, M. Ackermann, M. Ajello, W. Atwood, L. Baldini, *et. al.*, *Fermi LAT Search for Photon Lines from 30 to 200 GeV and Dark Matter Implications*, *Phys.Rev.Lett.* **104** (2010) 091302, [arXiv:1001.4836].

[72] **LAT Collaboration** Collaboration, M. Ackermann *et. al.*, *Fermi LAT Search for Dark Matter in Gamma-ray Lines and the Inclusive Photon Spectrum*, *Phys.Rev.* **D86** (2012) 022002, [arXiv:1205.2739].

[73] **Fermi-LAT Collaboration** Collaboration, M. Ackermann *et. al.*, *Search for Gamma-ray Spectral Lines with the Fermi Large Area Telescope and Dark Matter Implications*, *Phys.Rev.* **D88** (2013) 082002, [arXiv:1305.5597].

[74] **Fermi-LAT Collaboration** Collaboration, A. Albert *et. al.*, *Search for 100 MeV to 10 GeV γ-ray lines in the Fermi-LAT data and implications for gravitino dark matter in $\mu\nu$SSM*, *JCAP* **1410** (2014), no. 10 023, [arXiv:1406.3430].

[75] T. Bringmann, X. Huang, A. Ibarra, S. Vogl, and C. Weniger, *Fermi LAT Search for Internal Bremsstrahlung Signatures from Dark Matter Annihilation*, *JCAP* **1207** (2012) 054, [arXiv:1203.1312].

[76] M. Su and D. P. Finkbeiner, *Strong Evidence for Gamma-ray Line Emission from the Inner Galaxy*, arXiv:1206.1616.

[77] **Fermi-LAT collaboration** Collaboration, M. Ackermann *et. al.*, *Constraining Dark Matter Models from a Combined Analysis of Milky Way Satellites with the Fermi Large Area Telescope*, *Phys.Rev.Lett.* **107** (2011) 241302, [arXiv:1108.3546].

[78] **Fermi-LAT Collaboration** Collaboration, A. Abdo *et. al.*, *Observations of Milky Way Dwarf Spheroidal galaxies with the Fermi-LAT detector and constraints on Dark Matter models*, *Astrophys.J.* **712** (2010) 147–158, [arXiv:1001.4531].

[79] **Fermi-LAT Collaboration** Collaboration, M. Ackermann *et. al.*, *Dark Matter Constraints from Observations of 25 Milky Way Satellite Galaxies with the Fermi Large Area Telescope*, *Phys.Rev.* **D89** (2014) 042001, [arXiv:1310.0828].

[80] M. Mazziotta, F. Loparco, F. de Palma, and N. Giglietto, *A model-independent analysis of the Fermi Large Area Telescope gamma-ray data from the Milky Way dwarf galaxies and halo to constrain dark matter scenarios*, *Astropart.Phys.* **37** (2012) 26–39, [arXiv:1203.6731].

[81] A. Geringer-Sameth and S. M. Koushiappas, *Exclusion of canonical WIMPs by the joint analysis of Milky Way dwarfs with Fermi*, *Phys.Rev.Lett.* **107** (2011) 241303, [arXiv:1108.2914].

[82] I. Cholis and P. Salucci, *Extracting limits on Dark Matter annihilation from gamma-ray observations towards dwarf spheroidal galaxies*, *Phys.Rev.* **D86** (2012) 023528, [arXiv:1203.2954].

[83] A. Geringer-Sameth, S. M. Koushiappas, and M. G. Walker, *A Comprehensive Search for Dark Matter Annihilation in Dwarf Galaxies*, arXiv:1410.2242.

[84] M. Ackermann, M. Ajello, A. Allafort, L. Baldini, J. Ballet, *et. al.*, *Constraints on Dark Matter Annihilation in Clusters of Galaxies with the Fermi Large Area Telescope*, *JCAP* **1005** (2010) 025, [arXiv:1002.2239].

[85] J. Han, C. S. Frenk, V. R. Eke, L. Gao, S. D. White, *et. al.*, *Constraining Extended Gamma-ray Emission from Galaxy Clusters*, *Mon.Not.Roy.Astron.Soc.* **427** (2012) 1651–1665, [arXiv:1207.6749].

[86] O. Macias-Ramirez, C. Gordon, A. M. Brown, and J. Adams, *Evaluating the Gamma-Ray Evidence for Self-Annihilating Dark Matter from the Virgo Cluster*, *Phys.Rev.* **D86** (2012) 076004, [arXiv:1207.6257].

[87] **LAT collaboration** Collaboration, M. Ackermann *et. al.*, *Constraints on the Galactic Halo Dark Matter from Fermi-LAT Diffuse Measurements*, *Astrophys.J.* **761** (2012) 91, [arXiv:1205.6474].

[88] M. Cirelli, P. Panci, and P. D. Serpico, *Diffuse gamma ray constraints on annihilating or decaying Dark Matter after Fermi*, *Nucl.Phys.* **B840** (2010) 284–303, [arXiv:0912.0663].

[89] M. Papucci and A. Strumia, *Robust implications on Dark Matter from the first FERMI sky gamma map*, *JCAP* **1003** (2010) 014, [arXiv:0912.0742].

[90] G. A. Gomez-Vargas, M. A. Sanchez-Conde, J.-H. Huh, M. Peiro, F. Prada, *et. al.*, *Constraints on WIMP Annihilation for Contracted Dark Matter in the Inner Galaxy with the Fermi-LAT*, arXiv:1308.3515.

[91] I. Cholis, G. Dobler, D. P. Finkbeiner, L. Goodenough, T. R. Slatyer, *et. al.*, *The Fermi gamma-ray spectrum of the inner galaxy: Implications for annihilating dark matter*, arXiv:0907.3953.

[92] L. Goodenough and D. Hooper, *Possible Evidence For Dark Matter Annihilation In The Inner Milky Way From The Fermi Gamma Ray Space Telescope*, arXiv:0910.2998.

[93] D. Hooper and L. Goodenough, *Dark Matter Annihilation in The Galactic Center As Seen by the Fermi Gamma Ray Space Telescope*, *Phys.Lett.* **B697** (2011) 412–428, [arXiv:1010.2752].

[94] A. Boyarsky, D. Malyshev, and O. Ruchayskiy, *A comment on the emission from the Galactic Center as seen by the Fermi telescope*, *Phys.Lett.* **B705** (2011) 165–169, [arXiv:1012.5839].

[95] D. Hooper and T. Linden, *On The Origin Of The Gamma Rays From The Galactic Center*, *Phys.Rev.* **D84** (2011) 123005, [arXiv:1110.0006].

[96] K. N. Abazajian and M. Kaplinghat, *Detection of a Gamma-Ray Source in the Galactic Center Consistent with Extended Emission from Dark Matter Annihilation and Concentrated Astrophysical Emission*, *Phys.Rev.* **D86** (2012) 083511, [arXiv:1207.6047].

[97] C. Gordon and O. Macias, *Dark Matter and Pulsar Model Constraints from Galactic Center Fermi-LAT Gamma Ray Observations*, *Phys.Rev.* **D88** (2013) 083521, [arXiv:1306.5725].

[98] K. N. Abazajian, N. Canac, S. Horiuchi, and M. Kaplinghat, *Astrophysical and Dark Matter Interpretations of Extended Gamma-Ray Emission from the Galactic Center*, *Phys.Rev.* **D90** (2014) 023526, [arXiv:1402.4090].

[99] D. Hooper and T. R. Slatyer, *Two Emission Mechanisms in the Fermi Bubbles: A Possible Signal of Annihilating Dark Matter*, *Phys.Dark Univ.* **2** (2013) 118–138, [arXiv:1302.6589].

[100] T. Daylan, D. P. Finkbeiner, D. Hooper, T. Linden, S. K. N. Portillo, *et. al.*, *The Characterization of the Gamma-Ray Signal from the Central Milky Way: A Compelling Case for Annihilating Dark Matter*, arXiv:1402.6703.

[101] W.-C. Huang, A. Urbano, and W. Xue, *Fermi Bubbles under Dark Matter Scrutiny. Part I: Astrophysical Analysis*, arXiv:1307.6862.

[102] O. Macias and C. Gordon, *The Contribution of Cosmic Rays Interacting With Molecular Clouds to the Galactic Center Gamma-Ray Excess*, *Phys.Rev.* **D89** (2014) 063515, [arXiv:1312.6671].

[103] F. Calore, I. Cholis, and C. Weniger, *Background model systematics for the Fermi GeV excess*, arXiv:1409.0042.

[104] A. Drlica-Wagner, G. A. Gomez-Vargas, J. W. Hewitt, T. Linden, and L. Tibaldo, *Searching for Dark Matter Annihilation in the Smith High-Velocity Cloud*, *Astrophys.J.* **790** (2014) 24, [arXiv:1405.1030].

[105] M. Nichols, N. Mirabal, O. Agertz, F. J. Lockman, and J. Bland-Hawthorn, *The Smith Cloud and its dark matter halo: Survival of a Galactic disc passage*, *Mon.Not.Roy.Astron.Soc.* **442** (2014) 2883, [arXiv:1404.3209].

[106] **Fermi-LAT Collaboration** Collaboration, A. Abdo *et. al.*, *Constraints on Cosmological Dark Matter Annihilation from the Fermi-LAT Isotropic Diffuse Gamma-Ray Measurement*, *JCAP* **1004** (2010) 014, [arXiv:1002.4415].

[107] M. Fornasa, J. Zavala, M. A. Sanchez-Conde, F. Prada, and M. Vogelsberger, *Dark Matter implications of the Fermi-LAT measurement of anisotropies in the diffuse gamma-ray background: status report*, *Nucl.Instrum.Meth.* **A692** (2012) 132–136, [arXiv:1110.0324].

[108] T. Bringmann, F. Calore, M. Di Mauro, and F. Donato, *Constraining dark matter annihilation with the isotropic γ-ray background: updated limits and future potential*, *Phys.Rev.* **D89** (2014) 023012, [arXiv:1303.3284].

[109] I. Cholis, D. Hooper, and S. D. McDermott, *Dissecting the Gamma-Ray Background in Search of Dark Matter*, *JCAP* **1402** (2014) 014, [arXiv:1312.0608].

[110] J. Hisano, M. Kawasaki, K. Kohri, T. Moroi, and K. Nakayama, *Cosmic Rays from Dark Matter Annihilation and Big-Bang Nucleosynthesis*, *Phys.Rev.* **D79** (2009) 083522, [arXiv:0901.3582].

[111] F.-Y. Cyr-Racine, S. Profumo, and K. Sigurdson, *Protohalo Constraints to the Resonant Annihilation of Dark Matter*, *Phys.Rev.* **D80** (2009) 081302, [arXiv:0904.3933].

[112] A. V. Belikov and D. Hooper, *How Dark Matter Reionized The Universe*, *Phys.Rev.* **D80** (2009) 035007, [arXiv:0904.1210].

[113] S. Galli, F. Iocco, G. Bertone, and A. Melchiorri, *CMB constraints on Dark Matter models with large annihilation cross-section*, *Phys.Rev.* **D80** (2009) 023505, [arXiv:0905.0003].

[114] T. R. Slatyer, N. Padmanabhan, and D. P. Finkbeiner, *CMB Constraints on WIMP Annihilation: Energy Absorption During the Recombination Epoch*, *Phys.Rev.* **D80** (2009) 043526, [arXiv:0906.1197].

[115] G. Huetsi, A. Hektor, and M. Raidal, *Constraints on leptonically annihilating Dark Matter from reionization and extragalactic gamma background*, *Astron.Astrophys.* **505** (2009) 999–1005, [arXiv:0906.4550].

[116] M. Cirelli, F. Iocco, and P. Panci, *Constraints on Dark Matter annihilations from reionization and heating of the intergalactic gas*, *JCAP* **0910** (2009) 009, [arXiv:0907.0719].

[117] M. S. Madhavacheril, N. Sehgal, and T. R. Slatyer, *Current Dark Matter Annihilation Constraints from CMB and Low-Redshift Data*, *Phys.Rev.* **D89** (2014) 103508, [arXiv:1310.3815].

[118] M. Cirelli, *Indirect Searches for Dark Matter: a status review*, *Pramana* **79** (2012) 1021–1043, [arXiv:1202.1454].

[119] P. Meade, M. Papucci, A. Strumia, and T. Volansky, *Dark Matter Interpretations of the e+- Excesses after FERMI*, *Nucl.Phys.* **B831** (2010) 178–203, [arXiv:0905.0480].

[120] M. A. Sanchez-Conde and F. Prada, *The flattening of the concentration-mass relation towards low halo masses and its implications for the annihilation signal boost*, *Mon.Not.Roy.Astron.Soc.* **442** (2014) 2271, [arXiv:1312.1729].

[121] R. Catena and P. Ullio, *A novel determination of the local dark matter density*, *JCAP* **1008** (2010) 004, [arXiv:0907.0018].

[122] P. Salucci, F. Nesti, G. Gentile, and C. Martins, *The dark matter density at the Sun's location*, *Astron.Astrophys.* **523** (2010) A83, [arXiv:1003.3101].

[123] F. Prada, A. Klypin, J. Flix Molina, M. Martinez, and E. Simonneau, *Dark Matter Annihilation in the Milky Way Galaxy: Effects of Baryonic Compression*, *Phys.Rev.Lett.* **93** (2004) 241301, [astro-ph/0401512].

[124] M. Pato, O. Agertz, G. Bertone, B. Moore, and R. Teyssier, *Systematic uncertainties in the determination of the local dark matter density*, *Phys.Rev.* **D82** (2010) 023531, [arXiv:1006.1322].

[125] S. Garbari, C. Liu, J. I. Read, and G. Lake, *A new determination of the local dark matter density from the kinematics of K dwarfs*, *Mon.Not.Roy.Astron.Soc.* **425** (2012) 1445, [arXiv:1206.0015].

[126] A. Ghez, S. Salim, N. Weinberg, J. Lu, T. Do, *et. al.*, *Measuring Distance and Properties of the Milky Way's Central Supermassive Black Hole with Stellar Orbits*, *Astrophys.J.* **689** (2008) 1044–1062, [arXiv:0808.2870].

[127] J. F. Navarro, C. S. Frenk, and S. D. White, *The Structure of cold dark matter halos*, *Astrophys.J.* **462** (1996) 563–575, [astro-ph/9508025].

[128] J. F. Navarro, C. S. Frenk, and S. D. White, *A Universal density profile from hierarchical clustering*, *Astrophys.J.* **490** (1997) 493–508, [astro-ph/9611107].

[129] J. Einasto, *Kinematics and dynamics of stellar systems*, *Trudy Inst. Astrofiz. Alma-Ata* **51** 87.

[130] J. F. Navarro, A. Ludlow, V. Springel, J. Wang, M. Vogelsberger, *et. al.*, *The Diversity and Similarity of Cold Dark Matter Halos*, *Mon.Not.Roy.Astron.Soc.* **402** (2010) 21, [arXiv:0810.1522].

[131] J. N. Bahcall and R. Soneira, *The Universe at faint magnetidues. 2. Models for the predicted star counts*, *Astrophys.J.Suppl.* **44** (1980) 73–110.

[132] M. Gustafsson, M. Fairbairn, and J. Sommer-Larsen, *Baryonic Pinching of Galactic Dark Matter Haloes*, *Phys.Rev.* **D74** (2006) 123522, [astro-ph/0608634].

[133] T. Sjostrand, S. Mrenna, and P. Z. Skands, *A Brief Introduction to PYTHIA 8.1*, *Comput.Phys.Commun.* **178** (2008) 852–867, [arXiv:0710.3820].

[134] J. F. Beacom, N. F. Bell, and G. Bertone, *Gamma-ray constraint on Galactic positron production by MeV dark matter*, *Phys.Rev.Lett.* **94** (2005) 171301, [astro-ph/0409403].

[135] A. Birkedal, K. T. Matchev, M. Perelstein, and A. Spray, *Robust gamma ray signature of WIMP dark matter*, hep-ph/0507194.

[136] J. Mardon, Y. Nomura, D. Stolarski, and J. Thaler, *Dark Matter Signals from Cascade Annihilations*, *JCAP* **0905** (2009) 016, [arXiv:0901.2926].

[137] R. Essig, N. Sehgal, and L. E. Strigari, *Bounds on Cross-sections and Lifetimes for Dark Matter Annihilation and Decay into Charged Leptons from Gamma-ray Observations of Dwarf Galaxies*, *Phys.Rev.* **D80** (2009) 023506, [arXiv:0902.4750].

[138] T. E. Jeltema and S. Profumo, *Fitting the Gamma-Ray Spectrum from Dark Matter with DMFIT: GLAST and the Galactic Center Region*, *JCAP* **0811** (2008) 003, [arXiv:0808.2641].

[139] N. Arkani-Hamed, D. P. Finkbeiner, T. R. Slatyer, and N. Weiner, *A Theory of Dark Matter*, *Phys.Rev.* **D79** (2009) 015014, [arXiv:0810.0713].

[140] M. Pospelov and A. Ritz, *Astrophysical Signatures of Secluded Dark Matter*, *Phys.Lett.* **B671** (2009) 391–397, [arXiv:0810.1502].

[141] **PAMELA Collaboration** Collaboration, O. Adriani *et. al.*, *An anomalous positron abundance in cosmic rays with energies 1.5-100 GeV*, *Nature* **458** (2009) 607–609, [arXiv:0810.4995].

[142] **Fermi LAT Collaboration** Collaboration, A. A. Abdo *et. al.*, *Measurement of the Cosmic Ray e+ plus e- spectrum from 20 GeV to 1 TeV with the Fermi Large Area Telescope*, *Phys.Rev.Lett.* **102** (2009) 181101, [arXiv:0905.0025].

[143] **AMS Collaboration** Collaboration, M. Aguilar *et. al.*, *Electron and Positron Fluxes in Primary Cosmic Rays Measured with the Alpha Magnetic Spectrometer on the International Space Station*, *Phys.Rev.Lett.* **113** (2014) 121102.

[144] D. P. Finkbeiner and N. Weiner, *Exciting Dark Matter and the INTEGRAL/SPI 511 keV signal*, *Phys.Rev.* **D76** (2007) 083519, [astro-ph/0702587].

[145] J. Knodlseder, V. Lonjou, P. Jean, M. Allain, P. Mandrou, *et. al.*, *Early SPI / INTEGRAL contraints on the morphology of the 511 keV line emission in the 4th galactic quadrant*, *Astron.Astrophys.* **411** (2003) L457–L460, [astro-ph/0309442].

[146] M. Cirelli, G. Corcella, A. Hektor, G. Hutsi, M. Kadastik, *et. al.*, *PPPC 4 DM ID: A Poor Particle Physicist Cookbook for Dark Matter Indirect Detection*, *JCAP* **1103** (2011) 051, [arXiv:1012.4515].

[147] R. Essig, E. Kuflik, S. D. Mcdermott, T. Volansky, and K. M. Zurek, *Constraining Light Dark Matter with Diffuse X-Ray and Gamma-Ray Observations*, *JHEP* **1311** (2013) 193, [arXiv:1309.4091].

[148] **Planck Collaboration** Collaboration, P. Ade *et. al.*, *Planck 2013 results. XVI. Cosmological parameters*, *Astron.Astrophys.* **571** (2014) A16, [arXiv:1303.5076].

[149] M. Su, T. R. Slatyer, and D. P. Finkbeiner, *Giant Gamma-ray Bubbles from Fermi-LAT: AGN Activity or Bipolar Galactic Wind?*, *Astrophys.J.* **724** (2010) 1044–1082, [arXiv:1005.5480].

[150] T. Delahaye, R. Lineros, F. Donato, N. Fornengo, and P. Salati, *Positrons from dark matter annihilation in the galactic halo: Theoretical uncertainties*, *Phys.Rev.* **D77** (2008) 063527, [arXiv:0712.2312].

[151] A. Strong and I. Moskalenko, *The galprop program for cosmic ray propagation: new developments*, astro-ph/9906228.

[152] A. E. Vladimirov, G. Johannesson, I. V. Moskalenko, and T. A. Porter, *Testing the Origin of High-Energy Cosmic Rays*, *Astrophys.J.* **752** (2012) 68, [arXiv:1108.1023].

[153] I. Cholis, G. Dobler, D. P. Finkbeiner, L. Goodenough, and N. Weiner, *The Case for a 700+ GeV WIMP: Cosmic Ray Spectra from ATIC and PAMELA*, *Phys.Rev.* **D80** (2009) 123518, [arXiv:0811.3641].

[154] **Fermi-LAT Collaboration** Collaboration, J. Bregeon, E. Charles, and M. Wood, *Fermi-LAT data reprocessed with updated calibration constants*, arXiv:1304.5456.

[155] **Fermi-LAT Collaboration** Collaboration, M. Ackermann *et. al.*, *The Fermi Large Area Telescope On Orbit: Event Classification, Instrument Response Functions, and Calibration*, *Astrophys.J.Suppl.* **203** (2012) 4, [arXiv:1206.1896].

[156] "Fermi Science Tools." http://www.slac.stanford.edu/exp/glast/wb/prod/sciTools_Home.htm.

[157] **The Fermi-LAT Collaboration** Collaboration, *Fermi Large Area Telescope Third Source Catalog*, arXiv:1501.0200.

[158] I. Cholis and D. Hooper, *Dark Matter and Pulsar Origins of the Rising Cosmic Ray Positron Fraction in Light of New Data From AMS*, *Phys.Rev.* **D88** (2013) 023013, [arXiv:1304.1840].

[159] M. Boudaud, S. Aupetit, S. Caroff, A. Putze, G. Belanger, *et. al.*, *A new look at the cosmic ray positron fraction*, arXiv:1410.3799.

[160] H.-B. Jin, Y.-L. Wu, and Y.-F. Zhou, *Implications of the first AMS-02 measurement for dark matter annihilation and decay*, *JCAP* **1311** (2013) 026, [arXiv:1304.1997].

[161] A. Arvanitaki, S. Dimopoulos, S. Dubovsky, P. W. Graham, R. Harnik, *et. al.*, *Astrophysical Probes of Unification*, *Phys.Rev.* **D79** (2009) 105022, [arXiv:0812.2075].

[162] E. Nardi, F. Sannino, and A. Strumia, *Decaying Dark Matter can explain the e+- excesses*, *JCAP* **0901** (2009) 043, [arXiv:0811.4153].

[163] P.-f. Yin, Q. Yuan, J. Liu, J. Zhang, X.-j. Bi, *et. al.*, *PAMELA data and leptonically decaying dark matter*, *Phys.Rev.* **D79** (2009) 023512, [arXiv:0811.0176].

[164] A. Ibarra and D. Tran, *Decaying Dark Matter and the PAMELA Anomaly*, *JCAP* **0902** (2009) 021, [arXiv:0811.1555].

[165] K. Ishiwata, S. Matsumoto, and T. Moroi, *Cosmic-Ray Positron from Superparticle Dark Matter and the PAMELA Anomaly*, *Phys.Lett.* **B675** (2009) 446–449, [arXiv:0811.0250].

[166] C.-R. Chen, M. M. Nojiri, F. Takahashi, and T. Yanagida, *Decaying Hidden Gauge Boson and the PAMELA and ATIC/PPB-BETS Anomalies*, *Prog.Theor.Phys.* **122** (2009) 553–559, [arXiv:0811.3357].

[167] S. Baek, P. Ko, W.-I. Park, and Y. Tang, *Indirect and direct signatures of Higgs portal decaying vector dark matter for positron excess in cosmic rays*, *JCAP* **1406** (2014) 046, [arXiv:1402.2115].

[168] D. Hooper, N. Weiner, and W. Xue, *Dark Forces and Light Dark Matter*, *Phys.Rev.* **D86** (2012) 056009, [arXiv:1206.2929].

[169] **Fermi-LAT Collaboration** Collaboration, *Fermi-LAT Observations of the Diffuse Gamma-Ray Emission: Implications for Cosmic Rays and the Interstellar Medium*, *Astrophys.J.* **750** (2012) 3, [arXiv:1202.4039].

[170] http://fermi.gsfc.nasa.gov/ssc/data/access/lat/BackgroundModels.html. Galactic diffuse model used for all MC is based on (with flux renormalization to 1 GeV lowest energy) http://fermi.gsfc.nasa.gov/ssc/data/analysis/software/aux/gal_2yearp7v6_trim_v0.fits.

[171] P. W. Graham, D. E. Kaplan, S. Rajendran, and M. T. Walters, *Semiconductor Probes of Light Dark Matter*, *Phys. Dark Univ.* **1** (2012) 32–49, [arXiv:1203.2531].

[172] S. K. Lee, M. Lisanti, S. Mishra-Sharma, and B. R. Safdi, *Modulation Effects in Dark Matter-Electron Scattering Experiments*, arXiv:1508.0736.

[173] R. Essig, A. Manalaysay, J. Mardon, P. Sorensen, and T. Volansky, *First Direct Detection Limits on sub-GeV Dark Matter from XENON10*, *Phys. Rev. Lett.* **109** (2012) 021301, [arXiv:1206.2644].

[174] Y. Hochberg, Y. Zhao, and K. M. Zurek, *Superconducting Detectors for Superlight Dark Matter*, *Phys. Rev. Lett.* **116** (2016), no. 1 011301, [arXiv:1504.0723].

[175] Y. Hochberg, M. Pyle, Y. Zhao, and K. M. Zurek, *Detecting Superlight Dark Matter with Fermi-Degenerate Materials*, arXiv:1512.0453.

[176] K. Schutz and K. M. Zurek, *On the Detectability of Light Dark Matter with Superfluid Helium*, arXiv:1604.0820.

[177] Y. Hochberg, Y. Kahn, M. Lisanti, C. G. Tully, and K. M. Zurek, *Directional Detection of Dark Matter with 2D Targets*, arXiv:1606.0884.

[178] R. Essig, J. A. Jaros, W. Wester, P. H. Adrian, S. Andreas, *et. al.*, *Working Group Report: New Light Weakly Coupled Particles*, arXiv:1311.0029.

[179] C. Bird, P. Jackson, R. V. Kowalewski, and M. Pospelov, *Search for Dark Matter in $B \to S$ Transitions with Missing Energy*, *Phys.Rev.Lett.* **93** (2004) 201803, [hep-ph/0401195].

[180] N. Borodatchenkova, D. Choudhury, and M. Drees, *Probing MeV Dark Matter at Low-Energy E+E- Colliders*, *Phys.Rev.Lett.* **96** (2006) 141802, [hep-ph/0510147].

[181] B. McElrath, *Invisible Quarkonium Decays as a Sensitive Probe of Dark Matter*, *Phys.Rev.* **D72** (2005) 103508, [hep-ph/0506151].

[182] P. Fayet, *Constraints on Light Dark Matter and U Bosons, from Psi, Upsilon, K+, Pi0, Eta and Eta-Prime Decays*, *Phys.Rev.* **D74** (2006) 054034, [hep-ph/0607318].

[183] C. Bird, R. V. Kowalewski, and M. Pospelov, *Dark Matter Pair-Production in $B \to S$ Transitions*, *Mod.Phys.Lett.* **A21** (2006) 457–478, [hep-ph/0601090].

[184] Y. Kahn, M. Schmitt, and T. M. Tait, *Enhanced rare pion decays from a model of MeV dark matter*, *Phys.Rev.* **D78** (2008) 115002, [arXiv:0712.0007].

[185] P. Fayet, *U-boson production in e+ e- annihilations, psi and Upsilon decays, and Light Dark Matter*, *Phys.Rev.* **D75** (2007) 115017, [hep-ph/0702176].

[186] R. Essig, P. Schuster, and N. Toro, *Probing Dark Forces and Light Hidden Sectors at Low-Energy E+E- Colliders*, *Phys.Rev.* **D80** (2009) 015003, [arXiv:0903.3941].

[187] J. D. Bjorken, R. Essig, P. Schuster, and N. Toro, *New Fixed-Target Experiments to Search for Dark Gauge Forces*, *Phys. Rev.* **D80** (2009) 075018.

[188] M. Reece and L.-T. Wang, *Searching for the Light Dark Gauge Boson in Gev-Scale Experiments*, *JHEP* **0907** (2009) 051, [arXiv:0904.1743].

[189] P. Fayet, *Invisible Upsilon decays into Light Dark Matter*, *Phys.Rev.* **D81** (2010) 054025, [arXiv:0910.2587].

[190] G. K. Yeghiyan, *Upsilon Decays into Light Scalar Dark Matter*, *Phys.Rev.* **D80** (2009) 115019, [arXiv:0909.4919].

[191] A. Badin and A. A. Petrov, *Searching for light Dark Matter in heavy meson decays*, *Phys.Rev.* **D82** (2010) 034005, [arXiv:1005.1277].

[192] B. Echenard, *Search for Low-Mass Dark Matter at BABAR*, *Mod.Phys.Lett.* **A27** (2012) 1230016, [arXiv:1205.3505].

[193] J. March-Russell, J. Unwin, and S. M. West, *Closing in on Asymmetric Dark Matter I: Model Independent Limits for Interactions with Quarks*, *JHEP* **1208** (2012) 029, [arXiv:1203.4854].

[194] R. Essig, J. Mardon, M. Papucci, T. Volansky, and Y.-M. Zhong, *Constraining Light Dark Matter with Low-Energy e^+e^- Colliders*, *JHEP* **1311** (2013) 167, [arXiv:1309.5084].

[195] C. Boehm, M. J. Dolan, and C. McCabe, *A Lower Bound on the Mass of Cold Thermal Dark Matter from Planck*, *JCAP* **1308** (2013) 041, [arXiv:1303.6270].

[196] K. M. Nollett and G. Steigman, *BBN And The CMB Constrain Light, Electromagnetically Coupled WIMPs*, *Phys. Rev.* **D89** (2014), no. 8 083508, [arXiv:1312.5725].

[197] S. Andreas *et. al.*, *Proposal for an Experiment to Search for Light Dark Matter at the SPS*, arXiv:1312.3309.

[198] E. Izaguirre, G. Krnjaic, P. Schuster, and N. Toro, *New Electron Beam-Dump Experiments to Search for MeV to few-GeV Dark Matter*, *Phys.Rev.* **D88** (2013) 114015, [arXiv:1307.6554].

[199] **BDX Collaboration** Collaboration, M. Battaglieri *et. al.*, *Dark matter search in a Beam-Dump eXperiment (BDX) at Jefferson Lab*, arXiv:1406.3028.

[200] E. Izaguirre, G. Krnjaic, P. Schuster, and N. Toro, *Testing GeV-Scale Dark Matter with Fixed-Target Missing Momentum Experiments*, arXiv:1411.1404.

[201] B. Batell, R. Essig, and Z. Surujon, *Strong Constraints on Sub-GeV Dark Sectors from SLAC Beam Dump E137*, *Phys.Rev.Lett.* **113** (2014), no. 17 171802, [arXiv:1406.2698].

[202] Y. Kahn, G. Krnjaic, J. Thaler, and M. Toups, *DAE?ALUS and dark matter detection*, *Phys. Rev.* **D91** (2015), no. 5 055006, [arXiv:1411.1055].

[203] G. Krnjaic, *Probing Light Thermal Dark-Matter With a Higgs Portal Mediator*, arXiv:1512.0411.

[204] B. Batell, M. Pospelov, and A. Ritz, *Exploring Portals to a Hidden Sector Through Fixed Targets*, *Phys.Rev.* **D80** (2009) 095024, [arXiv:0906.5614].

[205] E. Izaguirre, G. Krnjaic, P. Schuster, and N. Toro, *Accelerating the Discovery of Light Dark Matter*, arXiv:1505.0001.

[206] C. Boehm and P. Fayet, *Scalar dark matter candidates*, *Nucl.Phys.* **B683** (2004) 219–263, [hep-ph/0305261].

[207] M. J. Strassler and K. M. Zurek, *Echoes of a Hidden Valley at Hadron Colliders*, *Phys.Lett.* **B651** (2007) 374–379, [hep-ph/0604261].

[208] D. Hooper and K. M. Zurek, *A Natural Supersymmetric Model with MeV Dark Matter*, *Phys.Rev.* **D77** (2008) 087302, [arXiv:0801.3686].

[209] J. L. Feng and J. Kumar, *The Wimpless Miracle: Dark-Matter Particles without Weak-Scale Masses Or Weak Interactions*, *Phys.Rev.Lett.* **101** (2008) 231301, [arXiv:0803.4196].

[210] D. E. Morrissey, D. Poland, and K. M. Zurek, *Abelian Hidden Sectors at a GeV*, *JHEP* **0907** (2009) 050, [arXiv:0904.2567].

[211] R. Essig, J. Kaplan, P. Schuster, and N. Toro, *On the Origin of Light Dark Matter Species*, arXiv:1004.0691.

[212] T. Cohen, D. J. Phalen, A. Pierce, and K. M. Zurek, *Asymmetric Dark Matter from a GeV Hidden Sector*, *Phys.Rev.* **D82** (2010) 056001, [arXiv:1005.1655].

[213] T. Lin, H.-B. Yu, and K. M. Zurek, *On Symmetric and Asymmetric Light Dark Matter*, *Phys.Rev.* **D85** (2012) 063503, [arXiv:1111.0293].

[214] X. Chu, T. Hambye, and M. H. Tytgat, *The Four Basic Ways of Creating Dark Matter Through a Portal*, *JCAP* **1205** (2012) 034, [arXiv:1112.0493].

[215] Y. Hochberg, E. Kuflik, T. Volansky, and J. G. Wacker, *Mechanism for Thermal Relic Dark Matter of Strongly Interacting Massive Particles*, *Phys.Rev.Lett.* **113** (2014) 171301, [arXiv:1402.5143].

[216] Y. Hochberg, E. Kuflik, H. Murayama, T. Volansky, and J. G. Wacker, *The Simplest Miracle*, arXiv:1411.3727.

[217] **XENON10** Collaboration, J. Angle *et. al.*, *A search for light dark matter in XENON10 data*, *Phys. Rev. Lett.* **107** (2011) 051301, [arXiv:1104.3088]. [Erratum: Phys. Rev. Lett.110,249901(2013)].

[218] **SuperCDMS** Collaboration, R. Agnese *et. al.*, *New Results from the Search for Low-Mass Weakly Interacting Massive Particles with the CDMS Low Ionization Threshold Experiment*, *Phys. Rev. Lett.* **116** (2016), no. 7 071301, [arXiv:1509.0244].

[219] G. Fernandez Moroni, J. Estrada, G. Cancelo, S. E. Holland, E. E. Paolini, and H. T. Diehl, *Sub-electron readout noise in a Skipper CCD fabricated on high resistivity silicon*, *Exper. Astron.* **34** (2012) 43–64, [arXiv:1106.1839].

[220] G. D. Starkman and D. N. Spergel, *A New technique for detecting supersymmetric dark matter*, hep-ph/9409275.

[221] M. Pyle *private communication*.

[222] **XENON100** Collaboration, E. Aprile *et. al.*, *A low-mass dark matter search using ionization signals in XENON100*, arXiv:1605.0626.

[223] P. Luke, J. Beeman, F. Goulding, S. Labov, and E. Silver, *Calorimetric ionization detector*, *Nucl.Instrum.Meth.* **A289** (1990) 406–409.

[224] B. Neganov and V. Trofimov *Otkrytiya, Izobret* **146** (1985) 215.

[225] **SuperCDMS** Collaboration, S. Golwala, *SuperCDMS SNOLAB: Goals, Design, and Status*, 2016. talk given at UCLA DM 2016.

[226] P. Lecoq, M. Korzhik, A. Annenkov, C. Pedrini, and A. Gektin, *Inorganic scintillators for detector systems*, *Springer-Verlag Berlin Heidelberg* (2006).

[227] M. Nikl and C. Pedrini, *Photoluminescence of heavily doped cef3: Cd2+ single crystals*, *Solid State Communications* **90** (1994), no. 3 155 – 159.

[228] C. A. Klein, *Bandgap dependence and related features of radiation ionization energies in semiconductors*, *Journal of Applied Physics* **39** (1968), no. 4 2029–2038.

[229] N. N. Ershov, N. G. Zakharov, and P. A. Rodnyi, *Spectral-kinetic study of the intrinsic-luminescence characteristics of a fluorite-type crystal*, *Optics and Spectroscopy* **53** (July, 1982) 51–54.

[230] L. Grabner, *Exciton emission and donor-acceptor association in thallium bromide*, *Phys. Rev. B* **4** (Aug, 1971) 1335–1339.

[231] G. H. Wannier, *The Structure of Electronic Excitation Levels in Insulating Crystals*, *Physical Review* **52** (Aug., 1937) 191–197.

[232] J. Frenkel, *On the Transformation of light into Heat in Solids. I*, *Physical Review* **37** (Jan., 1931) 17–44.

[233] A. Song and R. Williams, *Self-trapped excitons*. Springer series in solid-state sciences. Springer, 1996.

[234] P. A. Rodnyi, I. V. Khodyuk, E. I. Gorokhova, S. B. Mikhrin, and P. Dorenbos, *Emission and Excitation Spectra of ZnO:Ga and ZnO:Ga,N Ceramics*, *Opt. Spectrosc.* **105** (2008) 908, [arXiv:1009.1325].

[235] M. J. J. Lammers, G. Blasse, and D. S. Robertson, *The luminescence of cadmium tungstate (cdwo4)*, *physica status solidi (a)* **63** (1981), no. 2 569–572.

[236] V. V. Hizhnyakov, V. G. Plekhanov, V. V. Shepelev, and G. S. Zavt, *Hot luminescence of self-trapped excitons in alkali halide crystals*, *physica status solidi (b)* **108** (1981), no. 2 531–540.

[237] Y. Uchida and E. Matsui, *Optical properties of sodium iodide-thallium crystals*, *Japanese Journal of Applied Physics* **3** (1964), no. S1 622.

[238] A. Kitai, *Luminescent Materials and Applications*. Wiley Series in Materials for Electronic & Optoelectronic Applications. Wiley, 2008.

[239] B. A. Mazin, B. Bumble, S. R. Meeker, K. O'Brien, S. McHugh, and E. Langman, *A superconducting focal plane array for ultraviolet, optical, and near-infrared astrophysics*, *Opt. Express* **20** (Jan, 2012) 1503–1511.

[240] K. Irwin and G. Hilton, *Cryogenic Particle Detection Transition-Edge Sensors*, *Topics in Applied Physics* **99, 63** (2005).

[241] M. D. Petroff, M. G. Stapelbroek, and W. A. Kleinhans, *Detection of individual 0.4-28 μm wavelength photons via impurity-impact ionization in a solid-state photomultiplier*, *Applied Physics Letters* **51** (1987), no. 6 406–408.

[242] D. F. Santavicca, B. Reulet, B. S. Karasik, S. V. Pereverzev, D. Olaya, M. E. Gershenson, L. Frunzio, and D. E. Prober, *Energy resolution of terahertz single-photon-sensitive bolometric detectors*, *Applied Physics Letters* **96** (2010), no. 8.

[243] B. S. Karasik, S. V. Pereverzev, A. Soibel, D. F. Santavicca, D. E. Prober, D. Olaya, and M. E. Gershenson, *Energy-resolved detection of single infrared photons with $\lambda = 8\mu m$ using a superconducting microbolometer*, *Applied Physics Letters* **101** (2012), no. 5.

[244] D. J. Goldie, A. V. Velichko, D. M. Glowacka, and S. Withington, *Ultra-low-noise mocu transition edge sensors for space applications*, *Journal of Applied Physics* **109** (2011), no. 8.

[245] A. J. Miller, S. W. Nam, J. M. Martinis, and A. V. Sergienko, *Demonstration of a low-noise near-infrared photon counter with multiphoton discrimination*, *Applied Physics Letters* **83** (2003), no. 4 791–793.

[246] **CRESST** Collaboration, G. Angloher *et. al.*, *Results on light dark matter particles with a low-threshold CRESST-II detector*, *Eur. Phys. J.* **C76** (2016), no. 1 25, [arXiv:1509.0151].

[247] G. Angloher *et. al.*, *A CsI low temperature detector for dark matter search*, arXiv:1602.0888.

[248] M. Biroth, P. Achenbach, E. Downie, and A. Thomas, *Silicon photomultiplier properties at cryogenic temperatures*, *Nuclear Instruments & Methods in Physics Research Section A-Accelerators Spectrometers Detectors and Associated Equipment* **787** (2015) 68–71.

[249] P. Achenbach, M. Biroth, E. Downie, and A. Thomas, *On the operation of silicon photomultipliers at temperatures of 1-4 kelvin*, *Nuclear Instruments & Methods in Physics Research Section A-Accelerators Spectrometers Detectors and Associated Equipment* **824** (2016) 74–75.

[250] A. K. Drukier, K. Freese, and D. N. Spergel, *Detecting Cold Dark Matter Candidates*, *Phys. Rev.* **D33** (1986) 3495–3508.

[251] D. Tucker-Smith and N. Weiner, *Inelastic dark matter*, *Phys.Rev.* **D64** (2001) 043502, [hep-ph/0101138].

[252] M. Moszynski, M. Balcerzyk, W. Czarnacki, M. Kapusta, W. Klamra, P. Schotanus, A. Syntfeld, M. Szawlowski, and V. Kozlov, *Energy resolution and non-proportionality of the light yield of pure csi at liquid nitrogen temperatures*, *Nuclear Instruments and Methods in Physics Research Section A: Accelerators, Spectrometers, Detectors and Associated Equipment* **537** (2005), no. 1â 2 357 – 362. Proceedings of the 7th International Conference on Inorganic Scintillators and their Use in Scientific and Industrial Applications.

[253] C. C. ADAMS and R. DAMS, eds., *Copyright*, vol. 2 of *International Series of Monographs on Analytical Chemistry*. Pergamon, second edition completely revised and enlarged ed., 1970.

[254] R. Hofstadter, *The detection of gamma-rays with thallium-activated sodium iodide crystals*, *Phys. Rev.* **75** (Mar, 1949) 796–810.

[255] R. Hofstadter, *Erratum: The detection of gamma-rays with thallium-activated sodium iodide crystals*, *Phys. Rev.* **75** (May, 1949) 1611–1611.

[256] "Saint-gobain crystals." http://www.crystals.saint-gobain.com/. Accessed: 2016-02-17.

[257] M. Moszyriski, A. Nassalski, A. Syntfeld-Kazuch, L. Swiderski, and T. Szczesniak, *Energy resolution of scintillation detectors #x2014;new observations*, *Nuclear Science, IEEE Transactions on* **55** (June, 2008) 1062–1068.

[258] C. Sailer, B. Lubsandorzhiev, C. Strandhagen, and J. Jochum, *Low temperature light yield measurements in NaI and NaI(Tl)*, *European Physical Journal C* **72** (June, 2012) 2061, [arXiv:1203.1172].

[259] V. B. Mikhailik, V. Kapustyanyk, V. Tsybulskyi, V. Rudyk, and H. Kraus, *Luminescence and scintillation properties of csi: A potential cryogenic scintillator*, *physica status solidi (b)* **252** (2015), no. 4 804–810.

[260] D. Cusano, *Radiative recombination from gaas directly excited by electron beams*, *Solid State Communications* **2** (1964), no. 11 353 – 358.

[261] A. Knapitsch and P. Lecoq, *Review on photonic crystal coatings for scintillators*, *International Journal of Modern Physics A* **29** (2014), no. 30 1430070.

[262] M. Moszynski, M. Balcerzyk, W. Czarnacki, M. Kapusta, W. Klamra, P. Schotanus, A. Syntfeld, and M. Szawlowski, *Study of pure nai at room and liquid nitrogen temperatures*, in *Nuclear Science Symposium Conference Record, 2002 IEEE*, vol. 1, pp. 346–351 vol.1, Nov, 2002.

[263] C. Amsler, D. GrÃ¶gler, W. Joffrain, D. LindelÃ¶f, M. Marchesotti, P. Niederberger, H. Pruys, C. Regenfus, P. Riedler, and A. Rotondi, *Temperature dependence of pure csi: scintillation light yield and decay time*, *Nuclear Instruments and Methods in Physics Research Section A: Accelerators, Spectrometers, Detectors and Associated Equipment* **480** (2002), no. 2-3 494 – 500.

[264] S. E. Derenzo, E. Bourret-Courchesne, F. J. James, M. K. Klintenberg, Y. Porter-Chapman, J. Wang, and M. J. Weber, *Identifying semiconductors by d.c. ionization conductivity*, *IEEE Nuclear Science Symposium Conference Record* (2006) 1132–1132.

[265] M. Steger, A. Yang, T. Sekiguchi, K. Saeedi, M. L. W. Thewalt, M. O. Henry, K. Johnston, H. Riemann, N. V. Abrosimov, M. F. Churbanov, A. V. Gusev, A. K. Kaliteevskii, O. N. Godisov, P. Becker, and H.-J. Pohl, *Photoluminescence of deep defects involving transition metals in si: New insights from highly enriched 28si*, *Journal of Applied Physics* **110** (2011), no. 8.

[266] G. Davies, *Configurational instabilities at isoelectronic centres in silicon*, *Physica Scripta* **1994** (1994), no. T54 7.

[267] G. Davies, E. C. Lightowlers, K. Itoh, W. L. Hansen, E. E. Haller, and V. Ozhogin, *Isotope dependence of the indirect energy gap of germanium*, *Semiconductor Science and Technology* **7** (1992), no. 10 1271.

[268] J. P. Perdew, K. Burke, and M. Ernzerhof, *Generalized gradient approximation made simple*, *Phys. Rev. Lett.* **77** (Oct, 1996) 3865–3868.

[269] D. R. Hamann, M. Schlüter, and C. Chiang, *Norm-conserving pseudopotentials*, *Phys. Rev. Lett.* **43** (Nov, 1979) 1494–1497.

[270] Z. Levine and D. Allan, *Linear optical response in silicon and germanium including self-energy effects*, *Phys. Rev. Lett.* **63** (Oct, 1989) 1719–1722.

[271] Z. Levine and D. Allan, *Quasiparticle calculation of the dielectric response of silicon and germanium*, *Phys. Rev. B* **43** (Feb, 1991) 4187–4207.

[272] C. A. Klein, *Bandgap Dependence and Related Features of Radiation Ionization Energies in Semiconductors*, *Journal of Applied Physics* **39** (Mar., 1968) 2029–2038.

[273] G. F. Knoll, *Radiation detection and measurement; 4th ed.* Wiley, New York, NY, 2010.

[274] R. Knox, *Theory of excitons*. Solid state physics: Supplement. Academic Press, 1963.

[275] A. Song and R. Williams, *Self-trapped excitons*. Springer series in solid-state sciences. Springer, 1996.

[276] K. Cho, P. Dean, B. Fischer, D. Herbert, J. Lagois, and P. Yu, *Excitons*. Topics in Current Physics. Springer Berlin Heidelberg, 2012.

[277] R. Kubo and E. Hanamura, *Relaxation of Elementary Excitations: Proceedings of the Taniguchi International Symposium, Susono-shi, Japan, October 12–16, 1979*. Springer Series in Solid-State Sciences. Springer Berlin Heidelberg, 2012.

[278] "Almaz optics." http://www.almazoptics.com. Accessed: 2016-06-16.

[279] W. Setyawan, R. M. Gaume, R. S. Feigelson, and S. Curtarolo, *Comparative study of nonproportionality and electronic band structures features in scintillator materials*, *IEEE Transactions on Nuclear Science* **56** (Oct, 2009) 2989–2996.

[280] K. Kamiyoshi and Y. Nigara, *Dielectric constant of some alkali halides*, *physica status solidi (a)* **3** (1970), no. 3 735–741.

[281] J. Singh, *Physics of semiconductors and their heterostructures*. McGraw-Hill, 1992.

[282] P. YU and M. Cardona, *Fundamentals of Semiconductors: Physics and Materials Properties*. Graduate Texts in Physics. Springer Berlin Heidelberg, 2010.

[283] J. Deslippe, G. Samsonidze, D. A. Strubbe, M. Jain, M. L. Cohen, and S. G. Louie, *BerkeleyGW: A massively parallel computer package for the calculation of the quasiparticle and optical properties of materials and nanostructures*, *Computer Physics Communications* **183** (June, 2012) 1269–1289, [arXiv:1111.4429].

[284] A. Marini, C. Hogan, M. Grüning, and D. Varsano, *Yambo: An ab initio tool for excited state calculations*, *Computer Physics Communications* **180** (Aug., 2009) 1392–1403, [arXiv:0810.3118].

Epigram

Astera quondam aetatis compugnante furore
tangere non immo me esse volebat Ares.
Di sic deludunt homines crudelibus oestris:
lanas lacque ut dent, pasce gregem metibus.
Leniter at tolerare docebor fata morosa.
Exsurgo lacrimis. Plaudite et ite domum.

The End